THE EFFECT OF CONTAMINATION PARTICLES ON THE DYNAMICS OF ULTRA-LOW FLYING AIR BEARING SLIDERS

by

Xinjiang Shen

B. S. (Xi'an Jiaotong Univeristy, PR China) 1994
M. S. (University of Houston) 1999

A dissertation submitted in partial fulfillment of the

requirements for the degree of

Doctor of Philosophy

in

Engineering – Mechanical Engineering

in the

GRADUATE DIVISION

of the

UNIVERSITY OF CALIFORNIA AT BERKELEY

Committee in charge:

Professor David B. Bogy, Chair
Professor Tarek I. Zohdi
Professor Andrew R. Neureuther

Fall 2004

This dissertation of Xinjiang Shen is approved:

_____

Chair Date

_____

Date

_____

Date

University of California, Berkeley

Fall, 2004

THE EFFECT OF CONTAMINATION PARTICLES ON THE DYNAMICS OF ULTRA-LOW FLYING AIR BEARING SLIDERS

By

Xinjiang Shen

ABSTRACT

THE EFFECT OF CONTAMINATION PARTICLES ON THE DYNAMICS OF ULTRA-LOW FLYING AIR BEARING SLIDERS

by Xinjiang Shen

Doctor of Philosophy in Engineering- Mechanical Engineering

University of California at Berkeley

For complex air bearing slider designs the two dimensional approximation incorporated in the Reynolds equation for determining the airflow in the air bearing is not applicable due to steps in the air bearing surface. A model that incorporates some transverse flow effects is needed to better characterize the airflow between the slider and disk. Such a model is derived here to better predict the paths of contamination particles entrained in the air bearing. The characteristics of airflow and particle flow within the air bearing are then studied. The analysis with transverse effects included reveals that the transverse air velocity is not negligible in the geometric transition regions of the slider. Furthermore, this transverse velocity has a significant effect on the flight path of particles, and therefore, on the particle contamination profile on slider surfaces.

For a particle flying into contact with the slider or disk surfaces, criteria are needed to determine if it sticks or bounces. For an adhesive elastic particle such criteria based on its adhesive energy with the surface are derived and applied. The criteria reveal that nanometer particles are likely to stick to and contaminate the slider and disk surfaces.

For future high areal density hard disk drives, the magnetic spacing is expected to be less than 5nm, and the mechanical clearance between the head and disk is about 3.5nm. For such spacing, the effects of a particle in the head disk interface include the slider's flying height modulation and its MR read-back signal variation. The effects become more severe for less head disk clearance. The modeling of a particle in the head disk interface include three-body contact, frictional heating, and heat conduction due to the frictional heating and cooling effect of the slider air bearing. The contact force exerted on the slider by a nanometer size particle is on the order of 1/1000 gram. The effective force acting on the slider by a large number of particles is comparable to the gram load applied by the suspension in a hard disk drive. It modulates the slider's flying characteristics and changes the head signal sensitivity due to the spacing modulation between the MR sensor and disk media.

To my wife and son.

TABLE OF CONTENTS

LIST OF TABLES

LIST OF FIGURES

ACKNOWLEDGMENTS

The author wishes to thank his research advisor, Professor David B. Bogy for his continuous support throughout the research and academic study at University of California at Berkeley. The research freedom and opportunities at the Computer Mechanics Laboratory given by Professor Bogy are invaluable for me. I am honored to be one of his graduate students and learn from him all these years.

I would like to thank Dr. Mike Suk, who provided me professional advice during my internship at IBM. His insight into the research in the hard drive industry gave me much support. Also, his enthusiasm always encouraged me in my research.

Also, I would like to thank Dr. J. P. Peng and Martin Smallen for their continuing support and for spending time answering my questions and enlightening my research at Berkeley.

Throughout my academic study in America, my family gave me total support. My parents gave me freedom to make decisions and study aboard. My wife and son stood by my side all these years. Without their support, none of this would have been possible. They gave me the most motivation to learn and study. I owe everything to them for their sacrifice and endless love.

The research presented in this dissertation was supported by the Computer Mechanical Laboratory at University of California and partially by the IBM fellowship program.

Table of Contents

CHAPTER 1

INTRODUCTION

1.1 Magnetic disk drive evolution

Magnetic recording technology has evolved to become the most common means of storing personal and business information. The magnetic areal recording density has increased dramatically in the last decade. The new emerging customer electronics like personal video recorders (PVR), digital recorders, and high definition video recorders are pushing the capacity of hard drives to a new level. The hard drive is becoming smaller and faster for various applications. The speed of hard drives has also increased to a new level to achieve ever faster reading and writing of information on a magnetic disk drive. Many technological challenges have been overcome in this evolutionary process. However, the fundamentals of magnetic recording hard-disk drives have not changed much since their introduction. Figure 1.1 shows a picture of a modern hard-disk drive with its cover off, exposing the components. Such a disk drive usually contains more than one platter, as shown in Fig. 1.2, on which the data is stored. The writing and reading of the data is achieved by a magnoresistive sensor located on the air bearing slider which is supported by a suspension and arm. In order for the magnetic areal density to increase, the area of the magnetic bit has to shrink. Increasing the magnetic areal density requires packing the bits closer together in both the circumferential and radial directions, and a fundamental “paramagnetic” limit at which the bits will demagnetized their neighbors is expected to be reached soon for conventional longitudinal recording.

1 Tbit/in^2 is the current goal of academic and industry researchers (Wood, 2000) for the areal density of future hard disk drives. Organizations such as the Information Storage Industry Consortium (INSIC) in the US and Storage Research Consortium (SRC) in Japan are working on research in media and heads (magnetics), signal processing, servo, and tribology to achieve the goal of reaching 1 Tbit/in^2.

1.2 Head disk interface mechanics and reliability

In order for 1 Tbit/in^2 to be achieved in a HDD, the spacing between the read-write transducer and magnetic disk must decrease to have an acceptable signal-noise ratio (SNR) for the readback of the data on the disk. The targeted head media spacing is as low as 5nm for 1 Tbit/in^2. The mechanical issues also become of more concern because the inevitable contact between the head and disk causes off-track fluctuation of head as does air flow turbulence. It is a design goal to limit the slider's vertical modulation and off-track movement during the writing and reading process. Slider-disk contact can also cause damage to the disk and even loss of data. Diamond like carbon (DLC) is usually applied to protect the disk from scratches and wear. Lubricant is often applied to improve the durability of the DLC. Also, contamination particles in the head-disk interface play an important role in the head's dynamic behavior. In fact, these particles may cause the slider to crash and possibly cause total disk failure.

1.3 Air bearing sliders

The mechanical spacing between the head and disk is maintained by the proper design of the air bearing slider. Figure 1.3 shows an example of the air bearing of a slider

for hard disk drives. The air bearing slider is designed such that is has a sub-ambient pressure region in the middle, and high pressure on the air bearing surface especially at the trailing edge, as shown in the bottom portion of Fig. 1.3. The air bearing slider design has been changing with the increase of areal density, not only its structural design, but also its overall size. The typical slider in current products is called a “pico” slider, which has lateral dimensions of 1.25mm by 1mm. A smaller form factor, which is called the “femto” slider, with dimensions of 0.85mm by 0.7mm is under development for future products, and a few drives already use them.

1.4 Particle contamination and its effect on the head disk interface

When a hard disk drive operates in an office environment many air borne particles have a chance of entering the head disk interface, as shown in Fig. 1.4. Figure 1.5 shows a microphotograph of a contaminated air bearing slider. When a particle enters the air-bearing its possible effects include modulation of the flying height, abrasive wear and mechanical scratching of the magnetic disk surface, and thermally induced spikes in the read back signal. Such flash events near a magnetoresistive(MR) transducer can modify the MR signal because of the dependence of the MR resistance on temperature. More importantly, mechanical scratching of the magnetic disk surfaces may cause permanent data loss. These effects depend on the size and properties of the particles and their interaction with the slider and magnetic disk surfaces. Certain slider designs may reduce a particle’s chances of entering the air-bearing, contacting the slider and the disk surface, and/or contaminating the slider surfaces.

1.5 Objective

The research reported on in this dissertation seeks a better understanding of the particle contamination issues in the head disk interface as well as the effects of these particles on the hard disk performance. It consists of the following parts: modeling of the slider air bearing with transverse air flow effects, modeling of particles flying in the interface and contamination of these particles onto the slider and disk, and modeling the effects of particles entrapped in the head disk interface, including the slider's flying height modulation and the MR signal fluctuation induced by the particles.

In studying the slider air bearing, we started with the reduced Navier-Stokes equation for thin bearing films to derive a modified Reynold's equation with the effect of transverse air flow. We applied the air slip boundary conditions to calculate the air flow velocities in the lateral directions. The continuity equation for the air is used to calculate the air velocity in the transverse direction.

Then we developed a model to predict a particle's flying path in the head disk interface. Using this model, we simulated the flying behavior of several particles in the slider air bearing. When a particle impacts a slider or disk surface the stick/bounce criteria are used to determine the behavior of the particle. Sticking particles result in contamination on air bearing sliders.

A three-body contact model is developed for a particle entrapped in the head disk interface. The moving pattern of a particle in an air bearing is determined first by a criterion based on applied forces and moments. For sliding particles in a head disk interface, frictional heating is generated in the interface.

A particle entrapped in the head disk interface affects a slider's dynamic performance as well as the MR head's read-back signal. The slider's flying characteristics induced by these particles are studied. The heat generated by sliding particles is incorporated in a thermal analysis of air bearing sliders. In this way, we studied the MR signal change during the contamination process.

1.6 Dissertation Structure

The thesis consists of seven chapters. The first chapter is the introduction and the seventh chapter is the conclusion. Chapter 2 through Chapter 5 present the study of air bearing and particle flow and contamination of the head disk interface. Chapter 6 is concerned with the study of air bearing designs to reduce the effects of particles in the head disk interface. The model related to the slider air bearing is presented in Chapter 2, and Chapter 3 develops a hybrid grid refinement method for a complex bearing surface. The particle flow and contamination modeling is contained in Chapter 4. Chapter 5 presents three-body contact modeling for large hard particles in the head disk interface and the friction heating generated by a large particle. Chapter 6 is concerned with air bearing designs to reduce particle contamination and its effects.

Tables in all chapters appear in the text, while the figures are collected at the end of each chapter. The references are listed after the conclusion of the thesis.

Figure 1.1. Hard disk drive (http://www.seagate.com/).

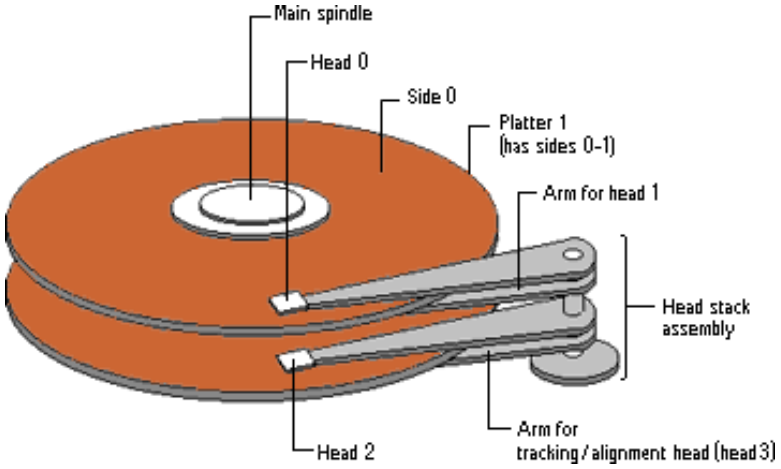

Figure 1.2. Open view of a hard disk drive

(http://www.philrees.co.uk/pc4music/optimisation.php).

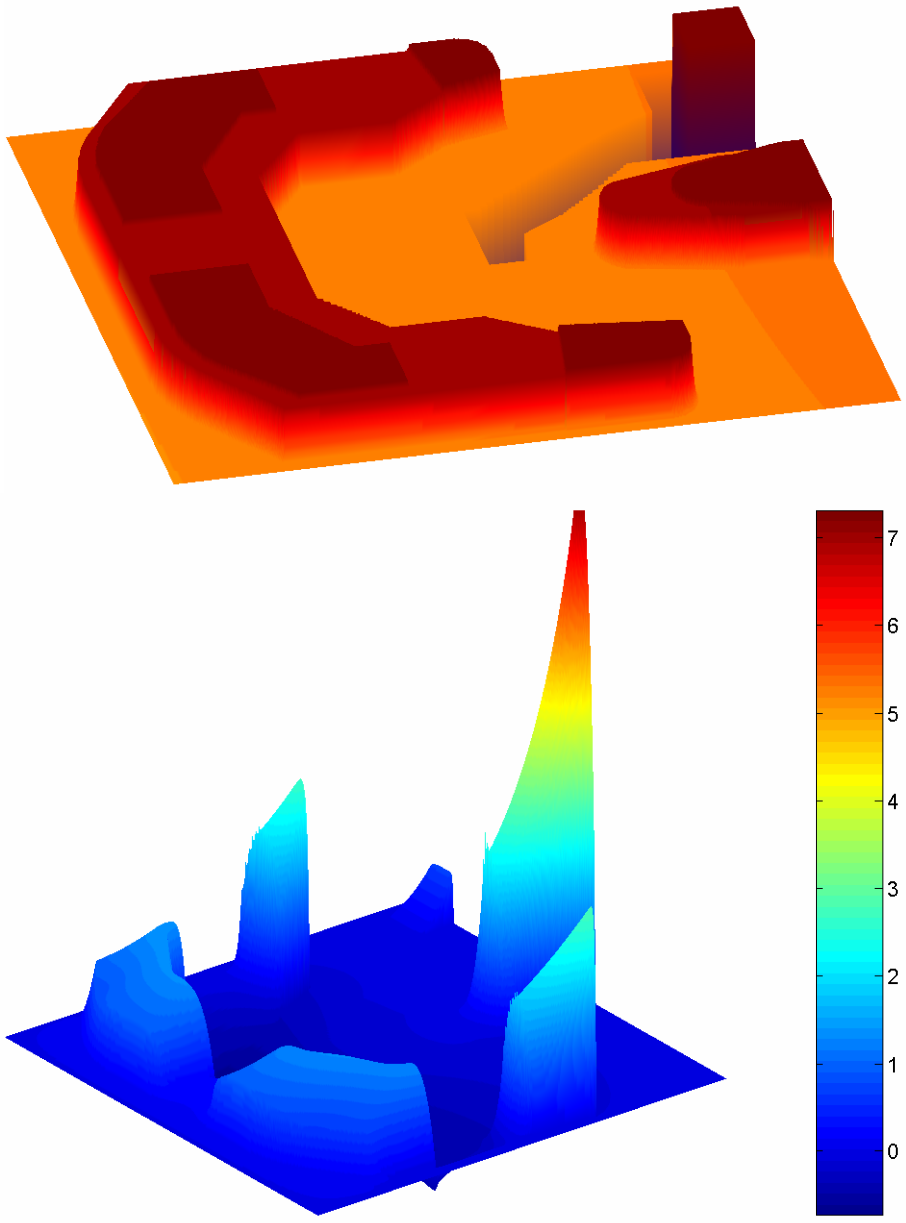

Figure 1.3. An air bearing slider and its pressure profile

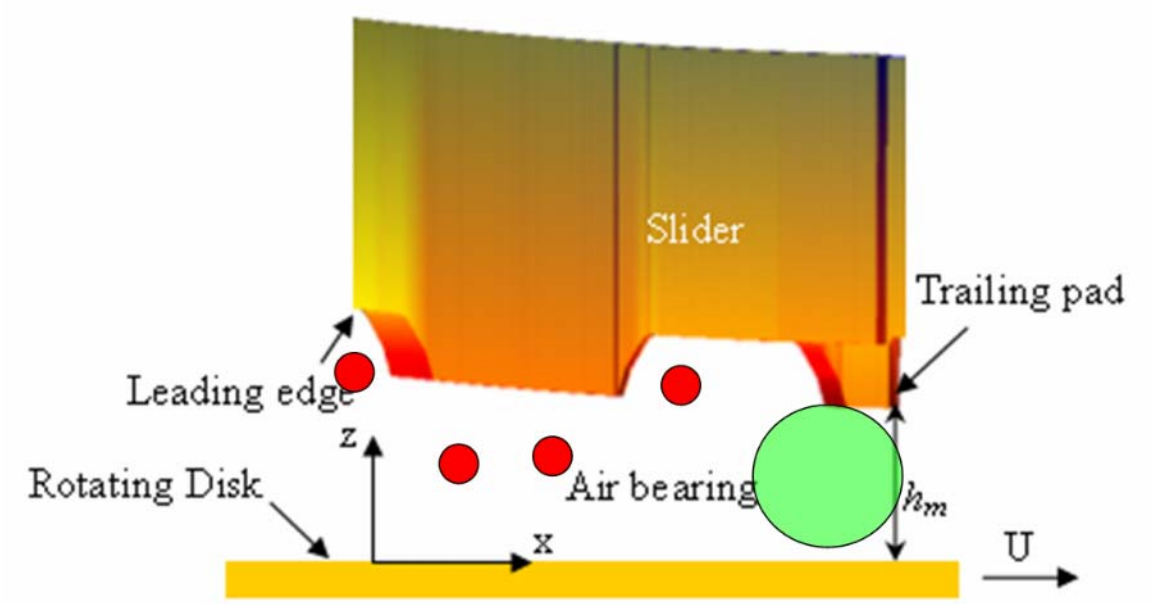

Figure 1.4. Particle flow and contamination in the head disk interface.

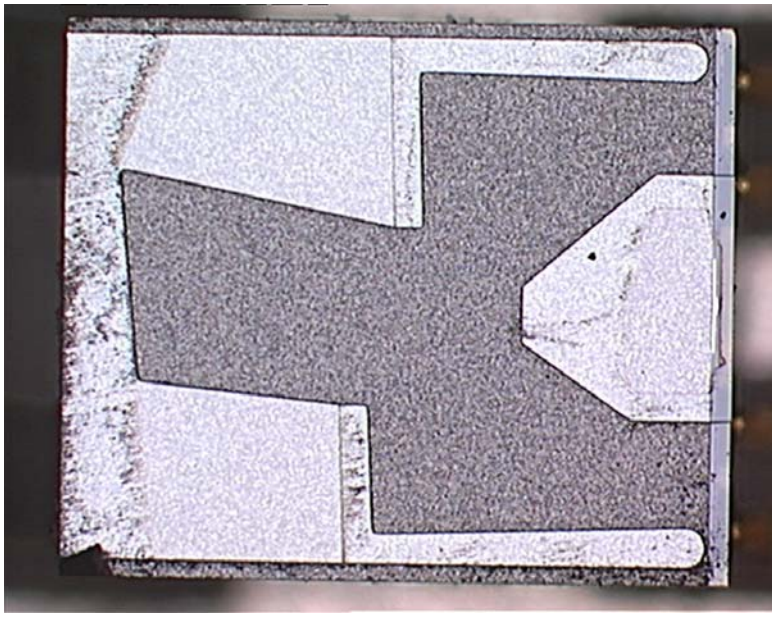

Figure 1.5. A contaminated air bearing slider operating in an office environment.

CHAPTER 2

AIR BEARING MODELING WITH TRANSVERSE FLOW EFFECTS

For modern complex slider designs the two dimensional approximation incorporated in the Reynolds equation for determining the airflow in the air bearing is not applicable due to the etch steps in the air bearing surface. A model that incorporates transverse flow effects is needed to better characterize the airflow between the slider and disk for sub 5nm applications. In this chapter such a model is derived to better predict the pressure profile and air flow of the slider air bearing. A modified Reynolds equation, including the 3-D slip boundary conditions, is proposed. The characteristics of the airflow within the air bearing are then studied. The analysis, including the transverse effects, reveals that the transverse velocity of the air is not negligible in the geometric transition regions of the slider. This transverse velocity has a significant effect on some applications, such as particle flow for air bearings below 5nm, and therefore, designs of air bearing sliders for 1Tbit/in^2 hard disk drives.

2.1. Introduction

As required by the evolution of magnetic recording disk drive technology, the mechanical flying height of air bearing sliders that position the read-write transducers has decreased dramatically. For 1Tbit/in^2 the flying height is expected to be as low as 3.5nm. Such nano spacing requires modeling of the air bearing that can account for the detailed features of air bearing sliders. The traditional Reynolds equation, which is used to calculate the air pressure, assumes there is no air transverse flow in the air bearing. Also,

for rarefied gas, most slip models do not consider the effect of a slider's geometrical discontinuities. These models work very well for air bearings with spacing above 20nm. For sub 5nm air bearing sliders the traditional slip models introduce higher pressure due to the air squeeze effect. Therefore, a 3-D slip model is needed for designing air bearings for 1Tbit/in^2 hard disk drives.

2.2. 3-D slip boundary condition modeling

The spacing between the slider and disk surface for a complex air bearing slider varies steeply in certain regions. The air flow conditions near the air bearing surface are very complicated due to the gas rarefaction effect. It depends on the spacing function, $z = h(x, y)$ and the mean free path of the air. Let $\vec{n} = \left(\frac{\partial h}{\partial x}, \frac{\partial h}{\partial y}, -1\right) / \sqrt{1 + \left(\frac{\partial h}{\partial x}\right)^2 + \left(\frac{\partial h}{\partial y}\right)^2}$ be the normal direction of the air bearing surface as shown in the highly distorted Fig. 2.1, and define a local coordinate system on the 3-D air bearing surface at (x, y, h(x,y)) as follows,

$$\vec{e}_1 = \left(1, 0, \frac{\partial h}{\partial x}\right) / \sqrt{1 + \left(\frac{\partial h}{\partial x}\right)^2} \tag{2.1}$$

$$\vec{e}_2 = \left(\frac{\partial h}{\partial x}\frac{\partial h}{\partial y}, -\left[1 + \left(\frac{\partial h}{\partial x}\right)^2\right], -\frac{\partial h}{\partial y}\right) / \sqrt{\left[1 + \left(\frac{\partial h}{\partial x}\right)^2\right]\left[1 + \left(\frac{\partial h}{\partial x}\right)^2 + \left(\frac{\partial h}{\partial y}\right)^2\right]} \tag{2.2}$$

$$\vec{e}_3 = \left(\frac{\partial h}{\partial x}, \frac{\partial h}{\partial y}, -1\right) / \sqrt{1 + \left(\frac{\partial h}{\partial x}\right)^2 + \left(\frac{\partial h}{\partial y}\right)^2} \tag{2.3}$$

Where $\vec{e}_3$ is the same as the normal direction of the air bearing surface.

Using the impenetrable property of the surfaces, we denote the air flow velocities on the air bearing surface in the global coordinates as u, v, $u\frac{\partial h}{\partial x}+v\frac{\partial h}{\partial y}$. The corresponding air velocity components in the local coordinates are u', v', 0, where

$$u' = \left\{u\left[1+\left(\frac{\partial h}{\partial x}\right)^2\right]+v\frac{\partial h}{\partial x}\frac{\partial h}{\partial y}\right\}/\sqrt{1+\left(\frac{\partial h}{\partial x}\right)^2} \tag{2.4}$$

$$v' = -\frac{\sqrt{1+\left(\frac{\partial h}{\partial x}\right)^2+\left(\frac{\partial h}{\partial y}\right)^2}}{\sqrt{1+\left(\frac{\partial h}{\partial x}\right)^2}}v \tag{2.5}$$

The free mean path for a rarefied gas is comparable to the characteristic length of the flow. The first order slip boundary conditions are stated as,

$$u\big|_{z=0} = U + a\lambda\left.\frac{\partial u}{\partial z}\right|_{z=0},\ u'\big|_{z=h} = a\lambda\left.\frac{\partial u'}{\partial n}\right|_{z=h};$$

$$v\big|_{z=0} = V + a\lambda\left.\frac{\partial v}{\partial z}\right|_{z=0},\ v'\big|_{z=h} = a\lambda\left.\frac{\partial v'}{\partial n}\right|_{z=h}. \tag{2.6}$$

where a is the accommodation factor and λ is the mean free path of the air.

2.3. Air bearing velocities in slider air bearings

From the reduced Navier-Stokes equations,

$$\frac{\partial p}{\partial x} = \frac{\partial}{\partial z}\left(\mu\frac{\partial u}{\partial z}\right) \tag{2.7}$$

$$\frac{\partial p}{\partial y} = \frac{\partial}{\partial z}\left(\mu\frac{\partial v}{\partial z}\right) \tag{2.8}$$

$$\frac{\partial p}{\partial z} = 0 \tag{2.9}$$

which is derived from the low Reynolds number Navier-Stokes equation, $\nabla p = \mu \nabla^2 \vec{v} + \frac{1}{3}\mu \nabla\left(\nabla \cdot \vec{v}\right)$, we have

$$u = \frac{1}{2\mu}\left(\frac{\partial p}{\partial x} z^2 + C_1 z + C_2\right), v = \frac{1}{2\mu}\left(\frac{\partial p}{\partial y} z^2 + C_3 z + C_4\right). \tag{2.10}$$

Using the slip boundary conditions (2.6) at $z = 0$, one gets

$$C_2 = 2\mu U + a\lambda C_1 \tag{2.11}$$

$$C_4 = 2\mu V + a\lambda C_3 \tag{2.12}$$

Therefore,

$$u = U + \frac{1}{2\mu}\left(\frac{\partial p}{\partial x} z^2 + C(x,y)\left(z + a\lambda\right)\right) \tag{2.13}$$

$$v = V + \frac{1}{2\mu}\left(\frac{\partial p}{\partial y} z^2 + D(x,y)\left(z + a\lambda\right)\right) \tag{2.14}$$

where C, D are determined from the slip boundary conditions at $z = h$.

Combining Eqns. (2.4,2.5) and (2.13, 2.14), we have

$$\begin{aligned} u' = &\left\{\left[U + \frac{1}{2\mu}\left(\frac{\partial p}{\partial x} z^2 + C(x,y)\left(z + a\lambda\right)\right)\right]\left[1 + \left(\frac{\partial h}{\partial x}\right)^2\right]\right. \\ &\left. + \left[V + \frac{1}{2\mu}\left(\frac{\partial p}{\partial y} z^2 + D(x,y)\left(z + a\lambda\right)\right)\right]\frac{\partial h}{\partial x}\frac{\partial h}{\partial y}\right\} \Big/ \sqrt{1 + \left(\frac{\partial h}{\partial x}\right)^2} \end{aligned} \tag{2.15}$$

$$v' = -\frac{\sqrt{1 + \left(\frac{\partial h}{\partial x}\right)^2 + \left(\frac{\partial h}{\partial y}\right)^2}}{\sqrt{1 + \left(\frac{\partial h}{\partial x}\right)^2}}\left[V + \frac{1}{2\mu}\left(\frac{\partial p}{\partial y} z^2 + D(x,y)\left(z + a\lambda\right)\right)\right] \tag{2.16}$$

and,

$$\left.\frac{\partial u'}{\partial n}\right|_{z=h} = \left[\frac{\partial u'}{\partial x}\frac{\partial h}{\partial x} + \frac{\partial u'}{\partial y}\frac{\partial h}{\partial y} - \frac{\partial u'}{\partial z}\right] \Big/ \sqrt{1+\left(\frac{\partial h}{\partial x}\right)^2 + \left(\frac{\partial h}{\partial y}\right)^2} \tag{2.17}$$

$$\left.\frac{\partial v'}{\partial n}\right|_{z=h} = \left[\frac{\partial v'}{\partial x}\frac{\partial h}{\partial x} + \frac{\partial v'}{\partial y}\frac{\partial h}{\partial y} - \frac{\partial v'}{\partial z}\right] \Big/ \sqrt{1+\left(\frac{\partial h}{\partial x}\right)^2 + \left(\frac{\partial h}{\partial y}\right)^2} \tag{2.18}$$

Substitute Eqns. (2.15-2.18) into the slip boundary condition at $z = h$ and solve for C, D to get

$$C(x,y) = -\left\{2\mu U + \frac{\partial p}{\partial x}\left[h^2 + 2a\lambda h \Big/ \sqrt{1+\left(\frac{\partial h}{\partial x}\right)^2 + \left(\frac{\partial h}{\partial y}\right)^2}\right]\right\} \Big/ \left[h + a\lambda\left(1 + 1\Big/\sqrt{1+\left(\frac{\partial h}{\partial x}\right)^2 + \left(\frac{\partial h}{\partial y}\right)^2}\right)\right], \tag{2.19}$$

$$D(x,y) = -\left\{2\mu V + \frac{\partial p}{\partial y}\left[h^2 + 2a\lambda h \Big/ \sqrt{1+\left(\frac{\partial h}{\partial x}\right)^2 + \left(\frac{\partial h}{\partial y}\right)^2}\right]\right\} \Big/ \left[h + a\lambda\left(1 + 1\Big/\sqrt{1+\left(\frac{\partial h}{\partial x}\right)^2 + \left(\frac{\partial h}{\partial y}\right)^2}\right)\right] \tag{2.20}$$

For $\frac{\partial h}{\partial x} \to \infty$ we have $C(x,y) = -\left(2\mu U + \frac{\partial p}{\partial x}h^2\right)/(h + a\lambda)$. Thus $u\big|_{z=h} = 0$, which is consistent with the wall condition for $\frac{\partial h}{\partial x} \to 0$. From this we get $C(x,y) = -\left(2\mu U + \frac{\partial p}{\partial x}\left(h^2 + 2a\lambda h\right)\right)/(h + 2a\lambda)$, which is the traditional first order slip boundary condition.

2.4. Modified Reynolds equation

Consider now the bearing surfaces shown in Fig. 2.2, where the lower surface represents the disk surface and the upper surface represents the slider air bearing. For the

slider air bearing the height h is very small compared with the slider's length and width. Also it is assumed that there is no variation of pressure across the air bearing, i. e.

$$\frac{\partial p}{\partial z} = 0 \tag{2.21}$$

From the air continuity equation,

$$\frac{\partial \rho}{\partial t} + \frac{\partial (\rho u)}{\partial x} + \frac{\partial (\rho v)}{\partial y} + \frac{\partial (\rho w)}{\partial z} = 0 \tag{2.22}$$

Integrate Eqn. (2.22) across the air bearing to get,

$$\int_0^h \frac{\partial \rho}{\partial t} dz + \int_0^h \frac{\partial (\rho u)}{\partial x} dz + \int_0^h \frac{\partial (\rho v)}{\partial y} dz + \int_0^h \frac{\partial (\rho w)}{\partial z} dz = 0 \tag{2.23}$$

Using

$$\int_0^h \frac{\partial}{\partial x}\left[f(x,z)\right] dz = \frac{\partial}{\partial x}\int_0^h f dz - f(x,h)\frac{\partial h}{\partial x} \tag{2.24}$$

in Eqn. (2.23) we obtain

$$\begin{aligned} &\frac{\partial}{\partial t}\int_0^h \rho dz + \frac{\partial}{\partial x}\int_0^h \rho u dz + \frac{\partial}{\partial y}\int_0^h \rho v dz + \rho w_h \\ &= \rho\left[\frac{\partial h}{\partial t} + u_h \frac{\partial h}{\partial x} + v_h \frac{\partial h}{\partial y} \right] \end{aligned} \tag{2.25}$$

Combine this with Eqn. (2.21) to arrive at

$$h\frac{\partial \rho}{\partial t} + \frac{\partial}{\partial x}\int_0^h \rho u dz + \frac{\partial}{\partial y}\int_0^h \rho v dz = 0 \tag{2.26}$$

which is the modified Reynolds equation for the air bearing including transverse air flow.

For an air bearing slider under steady state, the Reynolds equation becomes

$$\frac{\partial}{\partial x}\int_0^h \rho u dz + \frac{\partial}{\partial y}\int_0^h \rho v dz = 0 \tag{2.27}$$

Substituting Eqns. (2.13-2.14) into Equation (2.27), we get

$$\frac{\partial}{\partial X}\left(QPH^3\frac{\partial P}{\partial X}-\Lambda_x PH\right)+\frac{\partial}{\partial Y}\left(QPH^3\frac{\partial P}{\partial Y}-\Lambda_y PH\right)=0 \tag{2.28}$$

where $P=\frac{p}{p_a}$, $H=\frac{h}{h_m}$, $X=\frac{x}{L}$, $Y=\frac{y}{L}$ are the non-dimensionalized pressure, bearing clearance, coordinates in the slider length and width directions, respectively; p_a is the ambient atmospheric pressure; h_m is the nominal flying height of the slider at the trailing edge center; L is the length of the slider; $\Lambda_x=\frac{6\mu UL}{p_a h_m^2}\left(2-\frac{h+2a\lambda}{h+a\lambda(1+G)}\right)$ and $\Lambda_y=\frac{6\mu VL}{p_a h_m^2}\left(2-\frac{h+2a\lambda}{h+a\lambda(1+G)}\right)$ are the bearing numbers in the x and y directions, respectively; $G=\frac{1}{\sqrt{1+\left(\frac{\partial h}{\partial x}\right)^2+\left(\frac{\partial h}{\partial y}\right)^2}}$ is the geometric factor of the air bearing; Q is the flow factor, which for this modified slip boundary conditions takes the form

$$Q=-2+3\left(1+\frac{2aK_nG}{PH}\right)\frac{1+2a\frac{K_n}{PH}}{1+a(1+G)\frac{K_n}{PH}}, \tag{2.29}$$

where $a=\frac{2-\alpha}{\alpha}$ and α is the accommodation factor; $K_n=\frac{\lambda}{h_m}$ is the Knudsen number and λ is the mean free path of the air.

The modified Reynolds equation $\frac{\partial}{\partial x}\int_0^h \rho u dz+\frac{\partial}{\partial y}\int_0^h \rho v dz=0$ and the low Reynolds number Navier-Stokes equations $\nabla p=\mu\nabla^2\vec{v}+\frac{1}{3}\mu\nabla(\nabla\cdot\vec{v})$, together with the 3-D slip boundary conditions described previously can be used to solve for the pressure and

velocity fields in any nanometer scale geometry. The current modeling is derived specifically for complex slider air bearings which have much larger lateral dimensions than its vertical dimension.

2.5. Transverse air flow

In order to determine the trajectory of a particle within the air-bearing we must first determine the spacing between the slider and disk surfaces as well as the pressure and velocity fields. For a modern complex slider design with etch steps, the point-to-point spacing between the slider and the disk surfaces varies abruptly in places, introducing local three-dimensional airflow. Since the spacing is about three to five orders of magnitude less than the slider's lateral dimensions, we retain the following assumptions:

(1) The pressure gradient in the vertical direction is negligible; therefore, the pressure field calculated from the Reynolds equation is considered to be valid.

(2) The vertical air velocity at the step regions is not negligible although it is small compared to the in-plane velocity of the air.

Also, we assume that the particle volume concentration in the air bearing is low. Thus the particles do not affect the air bearing's dynamics. The air bearing velocity field can be solved without considering the particles flying in it. This assumption simplifies the problem and is expected to be valid for particle concentrations below 1%.

The transverse velocity w of the air in most of the air bearing satisfies the boundary conditions

$$w\big|_{z=0} = 0 \tag{2.30}$$

$$w\big|_{z=h} = 0 \tag{2.31}$$

Let $W_g = w/U$ be dimensionless, and substitute it into the air continuity equation to obtain

$$\frac{\partial U_g}{\partial X} + \frac{\partial V_g}{\partial Y} - \frac{l}{h_m}\frac{\partial W_g}{\partial Z} = 0\,. \tag{2.32}$$

where l is the length of the slider, and h_m is the nominal flying height of the slider. X, Y, Z are defined as $X = \frac{x}{l}$, $Y = \frac{y}{l}$ and $Z = \frac{z}{h_m}$.

For a compressible air bearing,

$$\frac{\partial \rho U_g}{\partial X} + \frac{\partial \rho V_g}{\partial Y} - \frac{l}{h_m}\frac{\partial \rho W_g}{\partial Z} = 0\,. \tag{2.33}$$

Therefore,

$$W_g = \frac{h_m}{\rho l}\int_0^Z \left(\frac{\partial \rho U_g}{\partial X} + \frac{\partial \rho V_g}{\partial Y} \right) dZ\,. \tag{2.34}$$

Combining this with the relationship between air pressure and density,

$$\rho = \frac{p}{p_0}\rho_0 = P\rho_0 \tag{2.35}$$

where ρ_0 is the density of air at the ambient pressure p_0, one has

$$W_g = \frac{h_m}{Pl}\int_0^Z \left(\frac{\partial \left(PU_g \right)}{\partial X} + \frac{\partial \left(PV_g \right)}{\partial Y} \right) dZ\,, \tag{2.36}$$

where U_g, V_g are the dimensionless air lateral velocities derived from either the first order, second order and 3-D slip boundary conditions as follows:

First order slip boundary condition:

$$U_g = \frac{1}{2\mu U}\frac{\partial p}{\partial x}\left[z^2 - hz - \lambda h\right] + \left[1 - \frac{z + a\lambda}{h + 2a\lambda}\right] \tag{2.37}$$

$$V_g = \frac{1}{2\mu U}\frac{\partial p}{\partial y}\left[z^2 - hz - \lambda h\right] + \frac{V}{U}\left[1 - \frac{z + a\lambda}{h + 2a\lambda}\right] \tag{2.38}$$

Second order slip boundary conditions

$$U_g = \frac{1}{2\mu U}\frac{\partial p}{\partial x}\left[z^2 - hz - \lambda h - \frac{\lambda^2}{2}\right] + \left[1 - \frac{z + a\lambda}{h + a\lambda}\right] \tag{2.39}$$

$$V_g = \frac{1}{2\mu U}\frac{\partial p}{\partial y}\left[z^2 - hz - \lambda h - \frac{\lambda^2}{2}\right] + \frac{V}{U}\left[1 - \frac{z + a\lambda}{h + a\lambda}\right] \tag{2.40}$$

3-D slip bounrady condition:

$$U_g = 1 + \frac{1}{2\mu U}\left(\frac{\partial p}{\partial x}z^2 + C(x,y)(z + a\lambda)\right) \tag{2.41}$$

$$V_g = \frac{V}{U} + \frac{1}{2\mu U}\left(\frac{\partial p}{\partial y}z^2 + D(x,y)(z + a\lambda)\right) \tag{2.42}$$

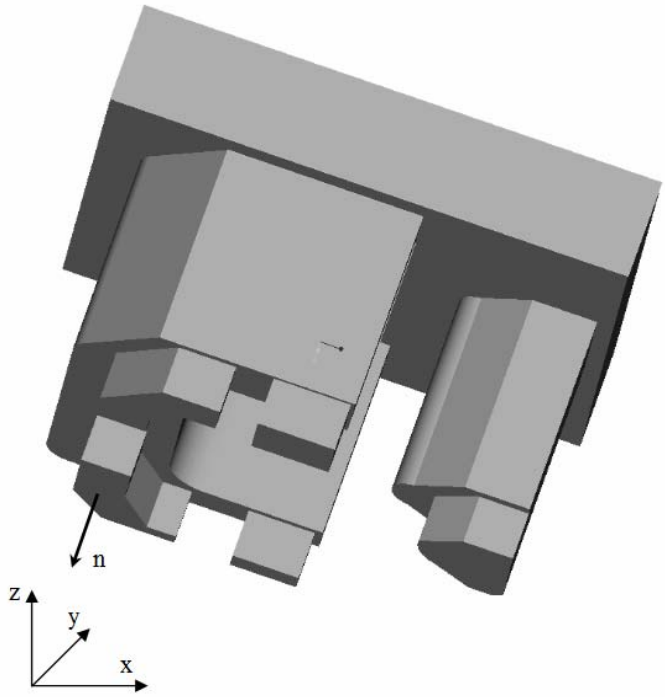

Figure 2.1, A 3-D view of an air bearing slider.

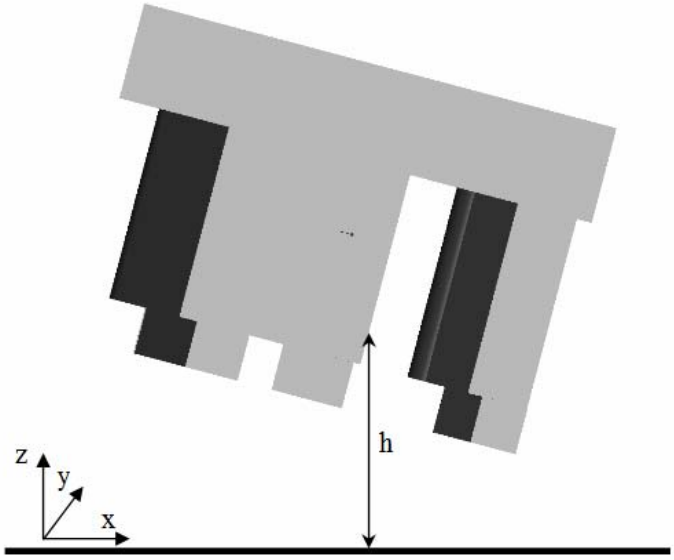

Figure 2.2, Head disk spacing between a slider and disk.

Chapter 3

HYBRID GRADIENT ADAPTIVE MESH WITH REFINEMENT FEATURES FOR ULTRA LOW FLYING HEIGHT SLIDERS

For 1Tbit/in^2 areal density magnetic storage disk drives, the minimum flying height of the air bearing sliders is expected to be less than 5nm. At such low fly heights, very high air pressure and pressure gradients are introduced at certain locations in the air bearing. Also, one needs to consider intermolecular forces between the slider and disk surfaces for such nanoscale spacing. To successfully simulate such complex air bearing designs, a robust mesh covering detailed features is required. In this chapter a hybrid adaptive mesh with refining ability is proposed and used on an example complex design. The mesh refinement feature allows users to control the grid density at desired locations, such as the minimum spacing locations, discontinuities, and the front taper. The results show that the new mesh method not only can resolve very high pressure and pressure gradient regions of ultra-low flying height sliders, but also it is more robust than the previous adaptive mesh used in the rectangular code (Quick 4) of the CML air bearing design program.

3.1. Introduction

The CML air bearing design code with its pressure gradient adaptive mesh has been successfully used for more than 15 years to design air bearing sliders for hard disk drives. At sub-5nm spacing very high air pressure is observed in most designs. Also, for

such applications the sliders become more complex in geometry. The design of future slider air bearings depends on a successful numerical solution, which requires a robust and adequate grid generation algorithm used in solving the generalized Reynolds equation. Two types of grids suitable for complex air bearing designs are the rectangular mesh which is employed in the CML Quick 4 solver. The other one employs a triangular meshing method, Quick 5, which was introduced recently in the CML code by Wu and Bogy [59]. Their unstructured adaptive triangular mesh technique is usually very efficient for traditional slider designs without small landing pads. However, sometimes it is difficult to mesh very complex designs using Quick 5. Also, there are presently no refinement features available in the rectangular or triangular grid generation methods used in the air bearing design codes. Some current ultra-low flying height slider designs have pads and grooves to meet various requirements. In the case of sub-5nm sliders the pressure at the minimum spacing will be extremely high due to the air squeezing effect, which requires a very fine mesh at this location. When the spacing between the slider and disk surfaces is less than 5nm, the intermolecular force between the slider air bearing and disk surface should also be included in the calculation. The mesh used to calculate the intermolecular forces should be fine enough to yield a converged result.

In this Chapter a meshing method with refinement features based on a combination of geometric and pressure gradients is proposed. The mesh refinement feature allows users to control the grid density at desired locations, such as at minimum spacing locations, discontinuities along rails, and at the front taper. The results show that the new meshing method not only can resolve very high pressure and pressure gradient regions of ultra-low flying height sliders, but it also is more robust and converges more

rapidly with increasing mesh numbers than the pressure adaptive mesh used in Quick 4. It is also less dependent on the initial conditions chosen for the calculation, and it requires less computation time.

3.2. Grid generated by geometric progression

To solve the Reynold's equation with the CML rectangular mesh the grid is initially generated by geometric progression in both the x and y directions. The computational domain can be divided into several intervals. For each interval, the control points can be specified by user input. Also, an expansion ratio for each interval can be assigned. The grid number becomes larger if the expansion ratio is greater than unity. For symmetric sliders, one may mesh only half of the slider in the computational domain. The other half will be mirrored automatically. Typically, one uses a uniform grid as the basis for mesh adaptation.

3.3. Adaptive grid with refinement features

Due to the complexity of modern air bearing designs uniform meshing is usually not adequate. The air bearing contains geometric discontinuities and wall profiles that are produced by etching processes. Also, there are certain locations that have extremely high air pressure and pressure gradients due to the air squeezing effect. Generally, more grids are needed at such locations. An adaptive grid with refinement features not only can provide more grids at these locations, but it can also decrease the total grid number for the entire computational domain. Therefore, it reduces the requirements on computational resources and shortens the slider design process. Previously, pressure gradient was used to adapt the grid distribution in both the x and y directions. This approach can resolve

certain high pressure and pressure gradient locations. However, this approach often does not perform very well at geometric discontinuities where geometric gradients should be used to replace pressure gradients as the grid density function. To avoid extremely high pressures or geometric gradients, an allowable ratio of maximum to minimum gradients is specified in the program, and it can be changed by user input.

Relatively small features such as landing pads designed to avoid meniscus force effects when the slider lands on the disk are used in complex slider designs, and they are not covered well by the previous meshing methods. For these features, local mesh refinement is required. The level of mesh refinement can be specified by user input.

3.4. Grid snapping and smoothing

It has been shown by Lu and Bogy [33] that grid snapping is very effective for achieving a stable convergence to the final flying height. Without grid snapping large fluctuations of the flying height and roll are evident as the computation progresses. Grid snapping is most effective for rails with straight boundaries. And also, it is required that the grid lines should align to the taper end if there is a taper in the air bearing design.

In numerical simulations abrupt changes in the grid size cause numerical errors. To reduce these numerical errors we use smoothing techniques. In the current implementation an exponentially decaying function is used. One may specify how fast the grid size changes by giving a certain decay factor. A larger decay factor means less grid smoothing. However, a very small decay factor also causes problems because the

grids are too densely focused at one location. Usually, a decay factor of about 60 is recommended for air bearing designs.

In order to incorporate the hybrid gradient adaptive meshing method with refinement features we needed to change the Quick 4 input file. The example input file is given in Appendix I, which shows the new parameters in bold text. The input file not only lets the user control the meshing in the grid in the x and y directions separately, it also lets the user refine the mesh at any location with a desired level. For the intermolecular force study the Hamaker constants can also be input in the intermolecular force menu.

To generate an appropriate grid mesh for a complex air bearing with an ultra low flying height one may iterate the grid meshing process to get stable and reliable flying characteristics.

3.5. Intermolecular force between slider and disk

With the evolution of magnetic disk drives, the slider's flying height is approaching sub 5nm. An important new physical phenomenon, the intermolecular force, affects the slider's flying height. The intermolecular force between two bodies can be calculated by use of the Lennard-Jones potential. The intermolecular force per unit area is calculated as [59]

$$F = \frac{A}{6\pi}\frac{1}{h^3} - \frac{B}{45\pi}\frac{1}{h^9} \tag{3.1}$$

The total intermolecular force between the slider and disk can be calculated by the following integration,

$$F_{vdw} = \int\left(\frac{A}{6\pi}\frac{1}{h^3} - \frac{B}{45\pi}\frac{1}{h^9}\right)dxdy \tag{3.2}$$

where A is the Hamaker constant between the slider and disk across the air bearing, $B = 9A\left(0.4\times10^{-9}\right)^6$ is a material constant determined by the Lennard-Jones separation distance, 0.4×10^{-9} m.

3.6. Numerical results and discussions

To study the effect of the current hybrid gradient adaptive meshing method we chose an example slider as shown in Fig. 3.1. This slider had been previously designed with the old code to have a flying height of 3.5 nm at the radius of 17mm with a skew angle of 1.1 degrees. In our previous study it was found that the simulated flying height increased with an increase of the grid size, and it was difficult to get a converged flying height for this complex air bearing design using the pressure gradient meshing grids. The grid generated by that method is shown in Fig. 3.2. One can see from Fig. 3.2 that although the grid in the y direction is very concentrated in the middle of the slider, the mesh in the x direction is less concentrated at the trailing pad. For such an ultra low flying height air bearing designs the pressure at the center of the trailing pad is more than 25atm, as shown in Fig. 3.3. The grid mesh does not capture this pressure spike very well. Also, in this complex air bearing design there are several geometrically steep step edges. Typically, none of these transition regions is covered by enough grids. To improve the mesh at these steep transitions we used the hybrid gradient mesh as shown in Fig. 3.4 where the geometric gradient controlled the grid density in the x direction and the pressure gradient controlled the grid density in the y direction. Figure 3.5 shows the pressure profile obtained with this mesh. While no major changes are observed, the

pressure profile is actually smoother than the one in Fig. 3.3 due to the finer mesh in the steep geometric regions. Figure 3.6 shows the comparison of the nominal flying height calculated by these two meshes at different grid sizes. The nominal flying height increases with the grid size and does not appear to converge for the pressure gradient adaptive mesh. However, the nominal flying height clearly shows convergence at a grid size of 705 when the hybrid gradient meshing grid is employed.

For some applications, mesh refinement is also desirable. In this new mesh generation method, this feature is also enabled. Figure 3.7 shows the mesh generated by the hybrid gradient with 4X refinement at the minimum spacing of the slider. The pressure profile calculated by this mesh is shown in Fig. 3.8. This pressure profile is very similar to that of Fig. 3.5. The effect of mesh refinement on the nominal flying height is shown in Fig. 3.9. The mesh size used for this calculation is 593. One can see that mesh refinement can improve the convergence of the nominal flying height. The nominal flying height becomes steady after the 4X mesh refinement is applied at the minimum spacing location. Figure 3.10 shows that the nominal flying height converges with grid size using this refined mesh. Even at the grid size of 593, the nominal flying height reaches its converged value. With this new mesh the calculation time is usually less than that with the pressure gradient mesh.

For ultra low flying height sliders, one needs to also consider intermolecular forces between the slider and disk surfaces. The intermolecular forces are largest at the minimum spacing between the slider air bearing and disk surface, which requires enough grids to precisely cover this region. Figure 3.11 shows the mesh refinement effect on the intermolecular force calculation. In this calculation, the nominal flying height is fixed at

3.745 nm with a pitch angle of 119 μrad and a roll angle of 1.825 μrad. The total intermolecular force decreases with an increase of grid size since the molecular force is very sensitive to the local height. At the refinement level of 40, the intermolecular force becomes converged at 0.133 gram.

Figure 3.12 shows the convergence process comparison between the old pressure gradient adaptive grid and the new hybrid gradient grid, and the comparison with and without molecular force for this example slider. The grid size is set to 593 for all these cases. The initial flying height is 6nm with a pitch angle of 150 μrad and a roll angle of 5 μrad. Figure 3.12 also shows that the hybrid gradient grid converges faster than the pressure gradient. Also, with the effect of intermolecular force included, the convergence process becomes slower. The intermolecular force causes the slider to fly lower with a nominal flying height of 3.732 nm.

3.7. Conclusions

In this Chapter a hybrid adaptive mesh with refining ability is proposed and used on an ultra low flying height complex design. The mesh refinement feature allows users to control the grid density at desired locations, such as at the minimum spacing locations, geometric discontinuities along rails, and at the front taper. The results show that this new hybrid gradient adaptive mesh method not only can resolve very high pressure and pressure gradient regions for ultra-low flying height sliders, but it is also more robust and quicker to converge than the pressure gradient adaptive grid used in Quick 4. Mesh refinement is also required for the intermolecular force calculation between a slider air bearing and disk surface because it is very sensitive to spacing and grid size.

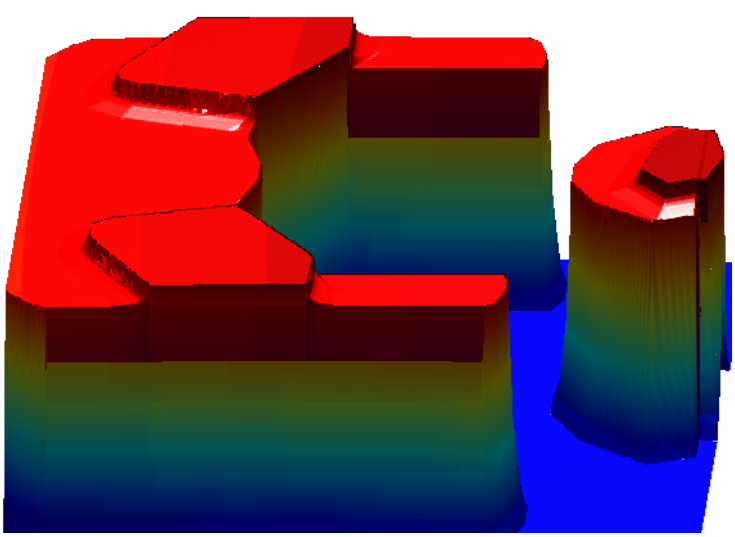

Figure 3.1. An example slider for studying the hybrid adaptive meshing grid.

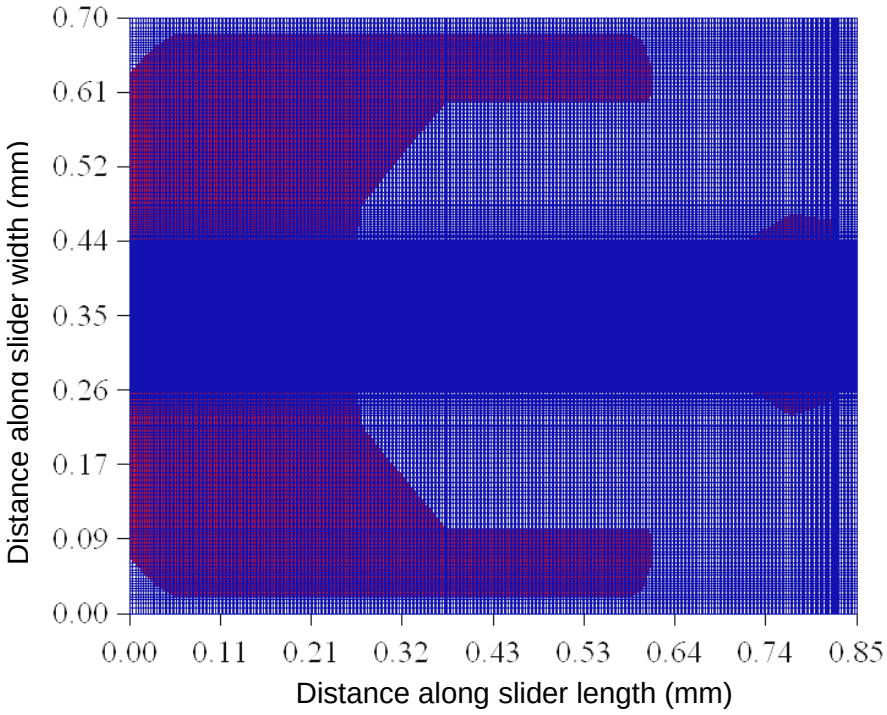

Figure 3.2. Pressure gradient adaptive mesh grids for the example slider.

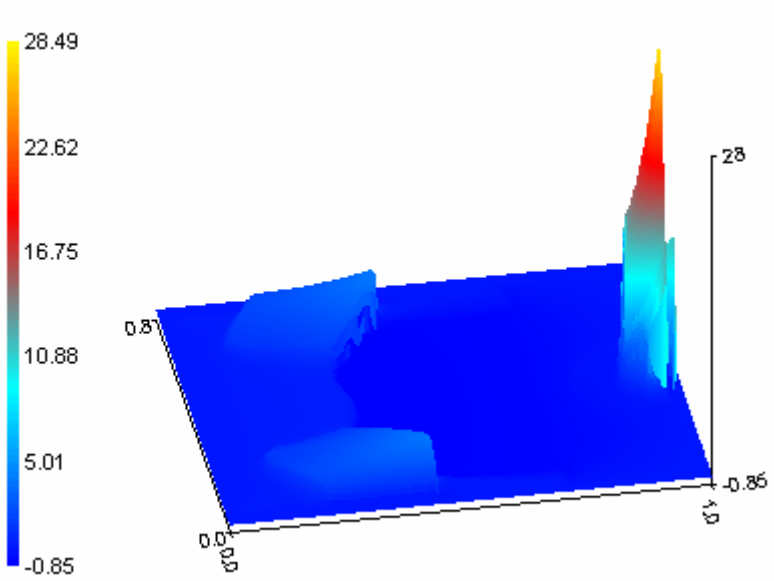

Figure 3.3. Pressure profile calculated by pressure gradient adaptive mesh.

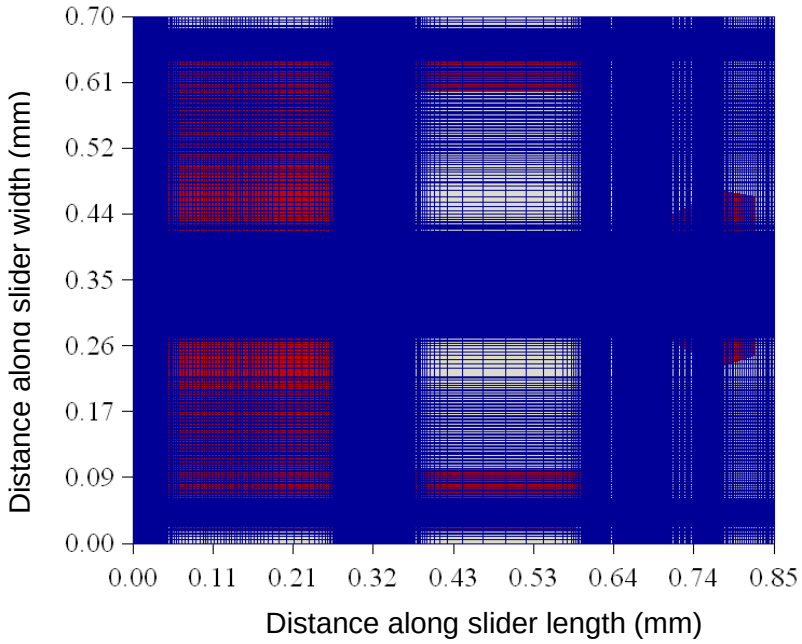

Figure 3.4. Hybrid gradient adaptive mesh grids without refinement features.

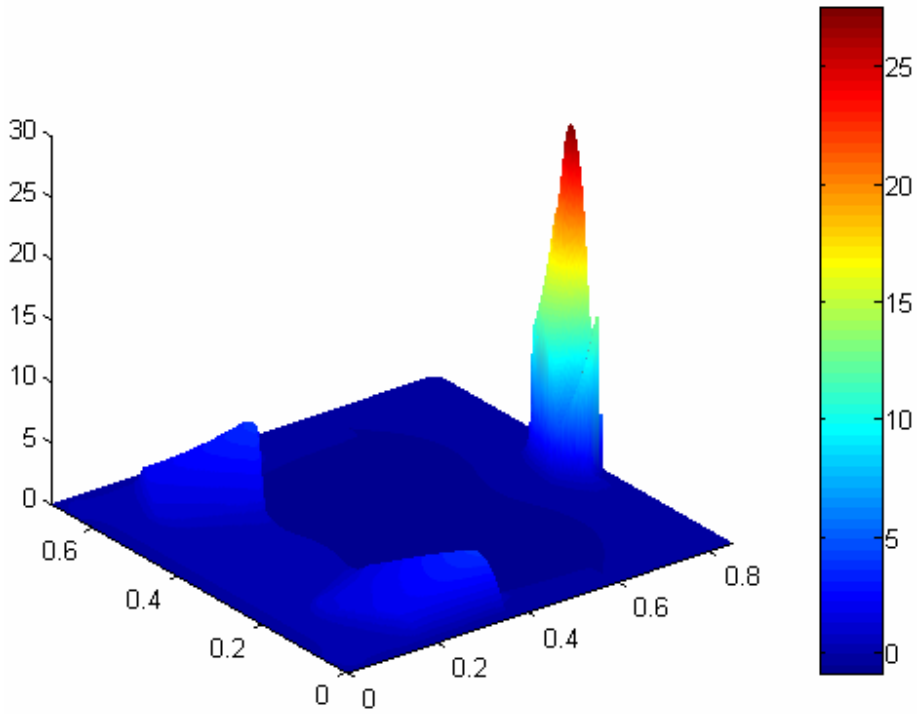

Figure 3.5. Pressure profile calculated by hybrid gradient adaptive mesh grids.

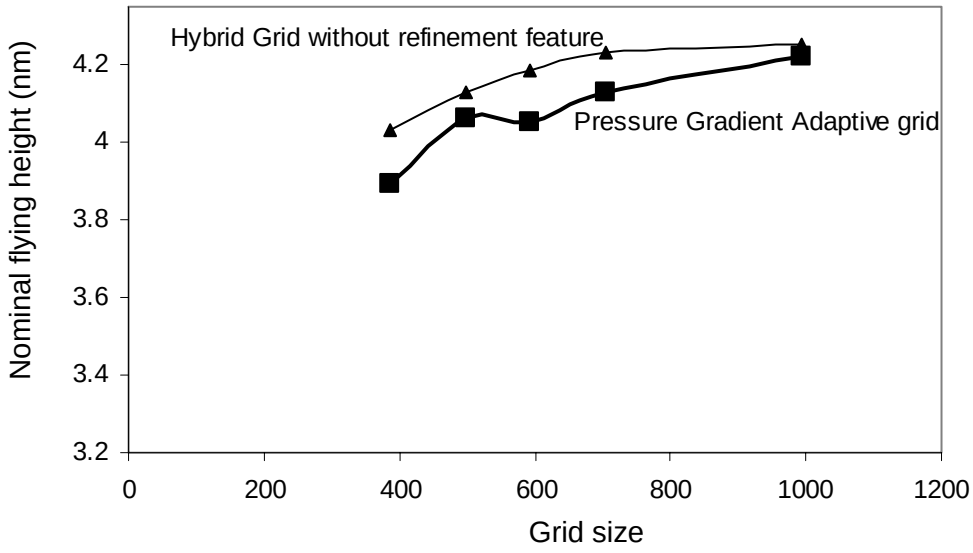

Figure 3.6. Flying height comparison between pressure gradient and hybrid grids.

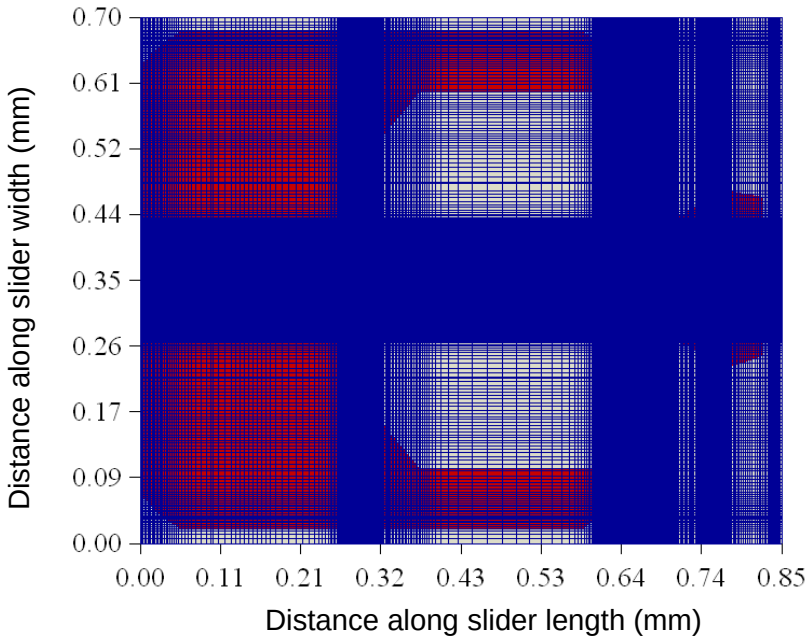

Figure 3.7. Hybrid gradient adaptive mesh with 4X refinement grids.

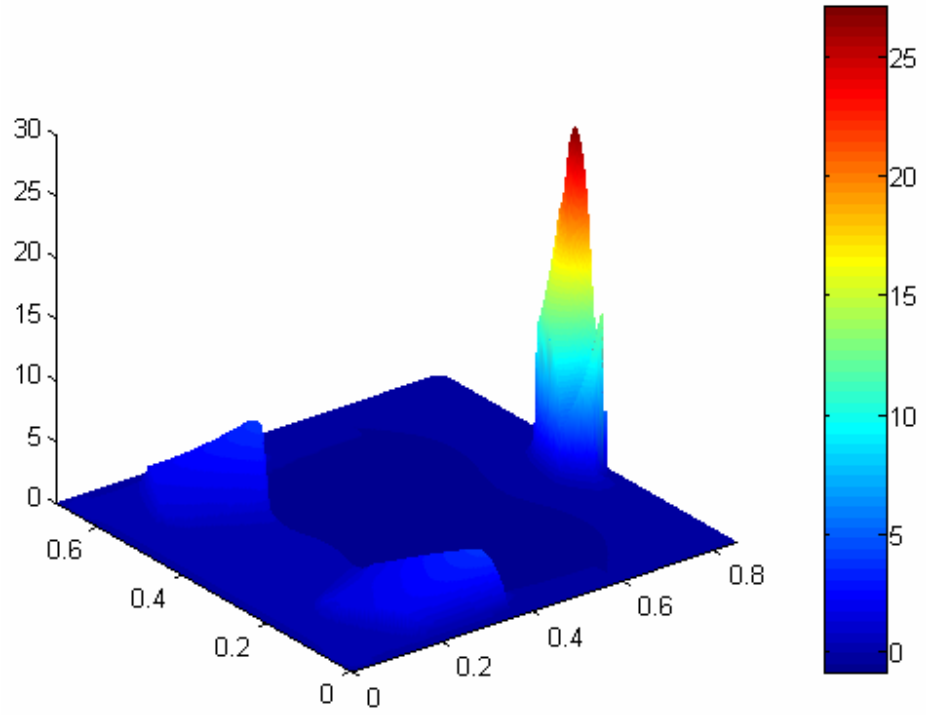

Figure 3.8. Pressure profile calculated by hybrid adaptive grids with 4X refinement.

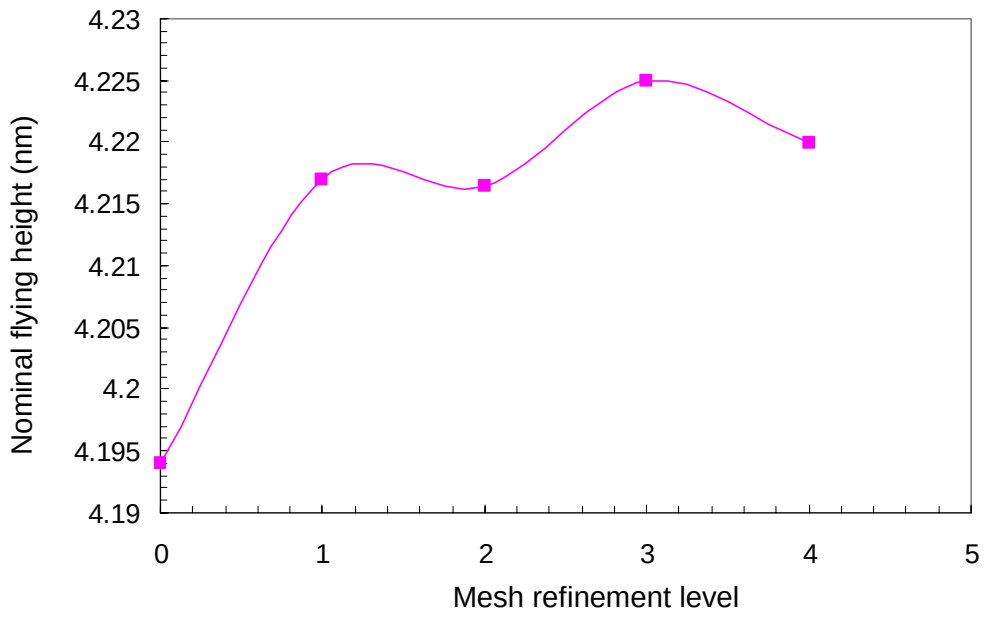

Figure 3.9. Effect of mesh refinement level on flying height convergence.

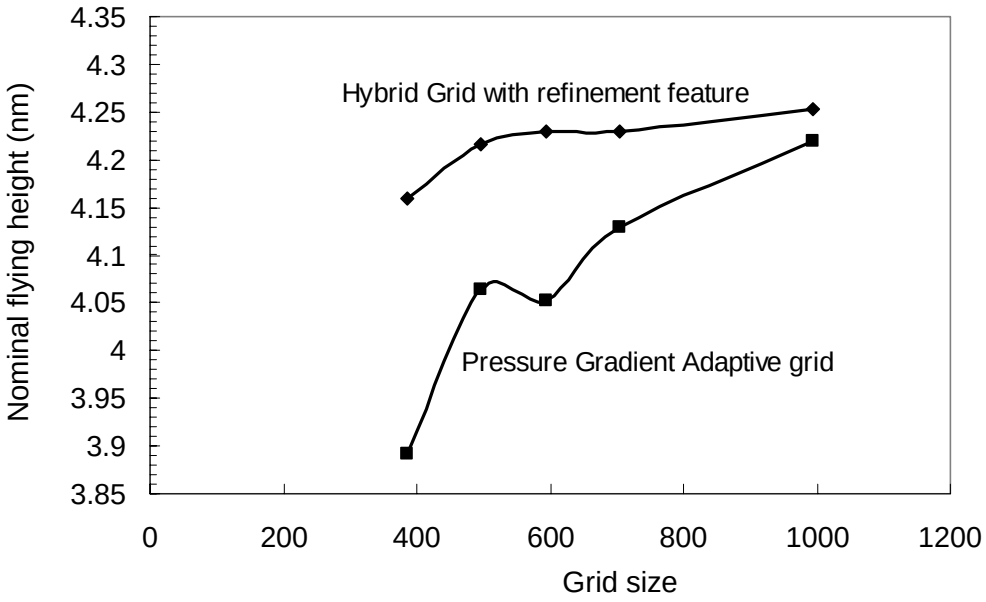

Figure 3.10. Effect of grid refinement on flying height convergence.

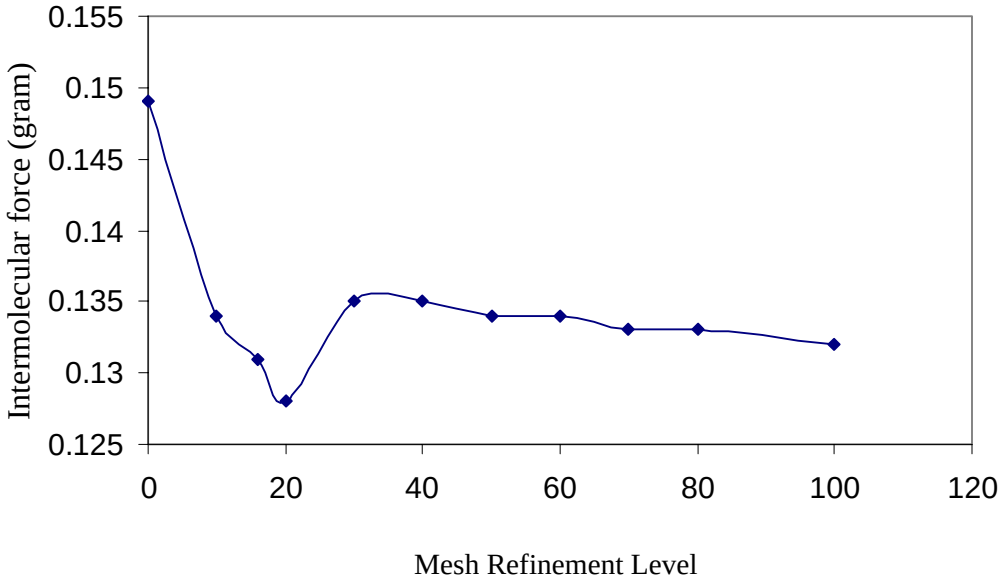

Figure 3.11. Effect of grid meshing on intermolecular forces between the slider and disk.

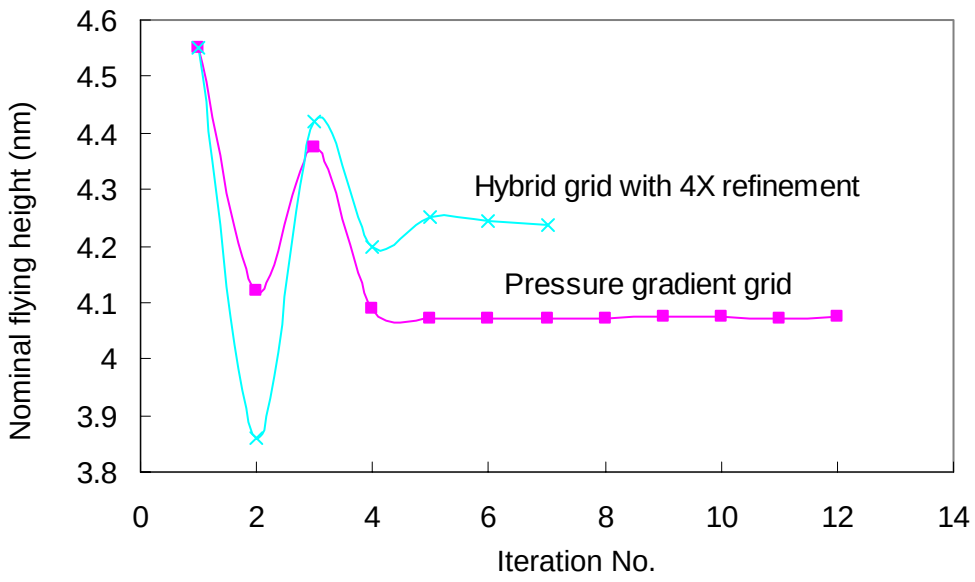

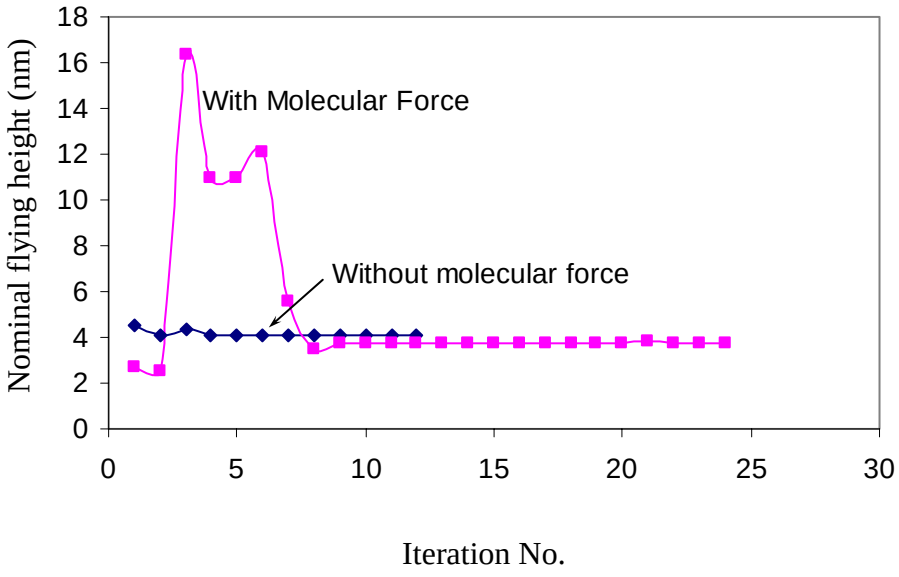

Figure 3.12. Effect of initial conditions on flying height on ultra low flying height sliders.

CHAPTER 4

PARTICLE FLOW AND CONTAMINATION IN THE HEAD DISK INTERFACE

4.1. Introduction

The motion of a particle moving from the leading edge to the trailing edge of an air bearing is quite difficult to describe due to the various forces acting on it. The forces are not only dependent on the particle's size, density and the air velocity and pressure fields in the air-bearing, but also on the relative velocities between the particle and the air-bearing, the particle speed and the initial entry conditions. Various expressions for determining the forces acting on a particle in unsteady gas flows have been derived by many researchers (Liu,1965; Saffmann, 1964 and Chen, X. 1996).

Previously, Zhang and Bogy [60, 61] studied the magnitudes of the Magnus lift force, the Saffmann lift force, and gravity force. The Magnus lift force is related to the spin of a particle in a fluid flow. The Saffmann lift force is caused by the pressure difference above and below a particle, which is caused by shear flow across the particle. The magnitude of the Saffmann lift force also depends on the velocity difference between the particle and air. If the particle's rotation speed is zero, there is no Magnus lift force. For very small particles, the gravity force is much smaller than the drag force, but for larger particles, the gravity force may not be negligible. The drag and lift forces depend on the relative velocity between the particle and the air. For airborne particles, which

have very small velocities relative to the flow in the air-bearing, the Magnus lift force, Saffmann lift force and drag force could be on the same order of magnitude because the Saffmann lift force is also very small. Among these forces, the drag, Saffmann and Magnus lift forces play important roles in large particle contamination on a slider surface.

In this Chapter we study some three-dimensional effects on particle contamination of slider surfaces for particles with different densities. Since the number density of the particles is small, collisions between the particles are assumed to have negligible effect and thus are neglected in the calculation. Furthermore, adhesion on first impact with the slider or disk is assumed. First, we modify the air bearing modeling to include some three-dimensional flow effects. We utilize the resulting equations to calculate the forces and the motion of a particle within an air-bearing based on previous work [50, 60-62]. We then choose some contemporary slider designs and show that the three-dimensional effects lead to markedly different results from the 2-dimensional flow analysis [50, 62]. Finally, the predicted contamination pattern is compared with experimental results for a particular ABS design.

4.2 Particle kinetics equations

The governing equations for a particle moving in air can be written as

$$\frac{d\vec{x}}{dt} = \vec{v} \tag{4.1}$$

$$m\frac{d\vec{v}}{dt} = \vec{f} \tag{4.2}$$

where $\vec{x}$ and $\vec{v}$ are the position and velocity vectors of the particle, respectively; m represents the mass of the particle; $\vec{f}$ includes the forces of drag, Saffmann lift, Magnus lift and gravity acting on the particle. The electrostatic and molecular forces between particles and slider surfaces are neglected. The thermophoretic force is also neglected because thermal flow is not considered here. Usually Brownian motion should be considered for such nanometer size particles. However, in hard disk drive air bearings, the shear rate of the air flow is very high. The importance of Brownian force may be characterized by a Peclet number, Pe. The Peclet number describes the ratio of shear to thermal (Brownian) effects at the particle scale.

$$Pe = \frac{3\pi\mu\dot{\gamma}d^3}{4k\Theta} \tag{4.3}$$

where $k = 1.38\times10^{-23}\,J/K$ is the Boltzmann constant, Θ is the air bearing temperature in Kelvin, and μ is the air viscosity. The air bearing shear rate is defined as $\dot{\gamma} = U/(h/2)$ where h is the spacing between slider and disk surfaces. For Pe>1, the hydrodynamic forces such as drag force dominate the Brownian force.

For the example slider considered here, the length is 1mm and the width is 0.8mm. The spacing between the slider and disk surfaces is between 25nm and 300 nm. The maximum velocity of air is on the order of 10 m/s. The particles' velocities are typically on the same order due to the air borne assumption. The volume concentration of particles is much less than 0.1%. The air viscosity is 1.5E-5 N-s/m^2. The Peclet number is between 560 and 6800 for 100nm particles in this study. For 30nm particles, the Peclet

number is between 15 and 185. Therefore, the Brownian motion of these particles can be ignored [Lee, 2003 and Shah, 1978].

The details of the hydrodynamic forces are studied by Zhang and Bogy [62], and so they are only briefly outlined here:

(1) Drag force

For a rigid spherical particle moving in the airflow, the drag force can be expressed [62] as

$$\vec{f}_d = \frac{\pi}{8} C_d C_w \rho_g d^2 \left\| \vec{u}_g - \vec{u}_p \right\| \left(\vec{u}_g - \vec{u}_p \right) \tag{4.4}$$

where C_d is the drag coefficient; C_w is the coefficient of the wall effects which tends to unity when the particle is far enough away from the wall; d is the diameter of the sphere; ρ_g is the density of the air; $\vec{u}_g$ and $\vec{u}_p$ are the velocity of the air and sphere, respectively.

(2) Saffmann lift force

The lift force acting on a spherical particle in a linear shear flow can be expressed as

$$f_{SL} = \frac{9}{4\pi} J \mu d^2 \Delta U \left(\frac{\rho_g G}{\mu} \right)^{1/2} \tag{4.5}$$

where ΔU is the velocity of the sphere relative to the airflow, which is given by $\Delta U = \frac{\left(\vec{u}_p - \vec{u}_g \right) \cdot \vec{u}_g}{\left\| \vec{u}_g \right\|}$; G is the magnitude of the airflow shear rate calculated by

$G = \dfrac{\vec{u}_g \cdot \dfrac{\partial \vec{u}_g}{\partial z}}{\left\| \vec{u}_g \right\|}$; J is expressed by Cox and Hsu [11] as $J = \dfrac{\pi^2}{16}\left(\dfrac{1}{\varepsilon} + \dfrac{11}{6} l_w^*\right)$. For a sphere far away from the wall J converges to Saffmann's value of 2.255. When the sphere is close to the wall J depends on the ratio, $\varepsilon = \dfrac{\left(\mathrm{Re}_G\right)^{1/2}}{\mathrm{Re}_S}$, and a non-dimensional distance $l_w^* = \left(\rho_g G / \mu\right)^{1/2} l_w$ in which l_w is the distance between the sphere and wall. Here $\mathrm{Re}_s = \Delta U R \rho_g / \mu$ and $\mathrm{Re}_G = G R^2 \rho_g / \mu$.

(3) Magnus lift force

The spinning of the particle and the air shear results in Magnus lift, which is expressed [62] as

$$\vec{f}_m = \frac{\pi}{8} \rho_g d^3 \left\{ \left[\vec{\omega} \times \left(\vec{u}_p - \vec{u}_g \right) \right] \cdot \vec{e}_z + \frac{1}{2} \frac{\partial \vec{u}_g}{\partial z} \cdot \left(\vec{u}_p - \vec{u}_g \right) \right\} \tag{4.6}$$

where $\vec{\omega}$ is the angular velocity vector of the particle; $\vec{e}_z$ is the unit vector in the z direction.

(4) Gravity force

The gravity force is given as

$$\vec{f}_g = \frac{4}{3} \pi R^3 \left(\rho_g - \rho_p \right) \vec{g} \tag{4.7}$$

where $\vec{g}$ is the acceleration due to gravity. The buoyancy force is also included in the calculation although it is negligible compared to the gravity force.

For particle flow analysis, the number and size distribution of the particles can, in principle, be determined from experiments. The particles are first assumed to be uniformly distributed above the disk surface with velocities close to the air-bearing's velocity where the particles are located. The particle's initial vertical velocity is assumed to be zero.

4.3. Numerical results and discussions

In this section the three-dimensional airflow effects on particle trajectories and contamination are studied. A representative modern negative pressure slider is chosen for this study (Fig. 4.1). The flying height of the slider is 26 nm. A sketch of the slider-disk assembly and coordinates is given in Fig. 4.2. The pressure profile shown in Fig. 4.3 is obtained without 3-D effects by solving the Reynolds equation for the air-bearing of the slider using the CML code Quick 4.

To study particle flow in the air-bearing, we first calculated the spacing function between the slider and the disk. The slider-disk spacing map is shown in Fig. 4.4, where it can be observed that particles may enter the recessed region of the air-bearing through the leading edge of the slider. Next, the air streamlines at different levels of the slider/disk spacing were calculated for heights above the disk of 1%, 50% and 99% of the spacing as shown in Figs. 4.5(a)-(c). It is shown that the airflow close to the disk is mainly determined by the disk velocity and slider skew angle, while close to the slider surface the streamlines are mainly determined by the slip boundary conditions of the air. The air streamline pattern at 50% follows the shape of the air-bearing. Previously, the vertical velocity of the air was assumed to be zero in the air-bearing, according to the 2-D

air bearing theory. However, due to the complex geometry of the slider, there is a pressure step change between the leading pad and the recess region. The pressure gradient and geometry (as shown in Figs. 4.6) cause the air to move vertically up along the wall according to the modified theory with transverse effects, as shown in Fig. 4.7. In the air bearing velocity calculation a very fine mesh grid of 385×385 is used. The mesh is also adapted to the pressure gradient in the air bearing. With this meshing method, the numerical error introduced by the mesh is reduced. Evidently, in the recess and ABS regions, the transverse airflow is still negligible since the pressure gradient is small and the air can be treated as flow between two parallel planes. In the transition zone (x/xl=0.08 in Fig. 4.7), the maximum transverse air velocity is 0.52U, where U is the disk velocity where the slider is located. This is about half of the 2-D velocity and thus, it can not be neglected. The drag force in the transverse direction acting on a particle due to this airflow is also not negligible in these regions.

By applying the transverse flow force component to the particle flow analysis as stated in the previous section we can make a comparison of particle trajectories between the air bearing solutions without and with the transverse effects, as shown in Fig. 4.8. It is seen that an airborne particle's trajectory predicted by the purely 2-D airflow analysis is almost parallel to the disk surface since the lift forces acting on it are so small and there is almost no drag force. The drag force acting on this particle in the 2-D model is on the order of -1E-14 micro Newton. For the 3-D model, however, the drag force acting on this particle is -1E-10 micro Newton before the leading edge and 1E-7 micro Newton before the recess region. Thus the drag force predicted by the 3-D model is about 4-7 orders of magnitude higher than that predicted by the 2-D model due to the transverse air flow in

the different regions. The gravity force is 6E-13 micro Newton for a 30nm particle. Also the lift force acting on the particle in Figure 4.8 is between 1E-11 and 1E-9 micro Newton. To further understand the transverse flow effects, a comparison of drag force and Saffmann lift force at various locations was carried out for the two models. The locations used for this comparison are illustrated in Fig. 4.4. The results are presented in Table 4.1. It is shown that the drag force contributes significantly in the transverse flow model (usually 2 orders higher than in the purely 2-D modeling), with little contribution from the Saffmann lift force. Due to the drag force effect, the transverse flow analysis predicts that the particle's path is modified at the places of abrupt change in the slider-disk spacing. In this case, the drag force is the main cause of the vertical motion of the particle. Figure 4.9 shows different trajectories for particles starting from different locations. Here we see that all particles are affected by the transverse airflow in the transition regions, and the drag force acting on a particle close to the disk surface is much smaller according to the calculations. In both Figs. 4.8 and 4.9, a particle is assumed to stick when it collides with the air bearing surface.

Applying the flow with and without transverse effects to the particle contamination analysis, we can compare the calculated contamination profiles (Fig. 4.10), which show a large difference between the two results. Initially, particles are distributed uniformly on the disk surface. These particles have a density of 4.25×10^3 kg/m^3 and initial velocities equal to that of the air where they are located. The particle size in Fig. 4.10 is 30nm. The particle contamination profile obtained by the purely 2-D analysis has many particles on the leading pad, and there are no particles attached to and after the transition regions of the air-bearing surface. For the 3-D modeling, few particles

are observed on the leading pad, and more particles are observed in the transition region between the leading pad and the recess region according to the airflow analysis with transverse effects.

Figures 4.11 and 4.12 show a comparison of the numerical simulation of a particle contamination profile with experiments for a particular slider design. One can see in both figures that many particles strike the front edge of the rails. These are large particles coming from the entrance. In the simulation results of Fig. 4.12, 30nm and 100nm particles are used. They have the same density of 4.25×10^{3} kg/m^{3}. They are distributed uniformly on the disk surface in the entrance of the air bearing. Mostly the 100nm particles are deposited in this region. There are also many small particles that pass through the spacing between the slider and disk surfaces (< 50nm spacing). For these particles, we used 30 nm in the simulation. The numerical simulation is seen to provide good quantitative agreement with the experiment.

4.4. Conclusions

From the multi-particle flow analyses in the air bearing we observe that the analysis with transverse flow effects predicts results that are quite different from those predicted by the purely 2-D air bearing theory. We observe that with the transverse effects the particles are more likely to contaminate the transition regions on the rail surfaces between the leading pad and recessed regions, a result not predicted by the 2-D flow analysis. And also, the particle contamination profile predicted using the 3-D model with air transverse flow is consistent with experimental results.

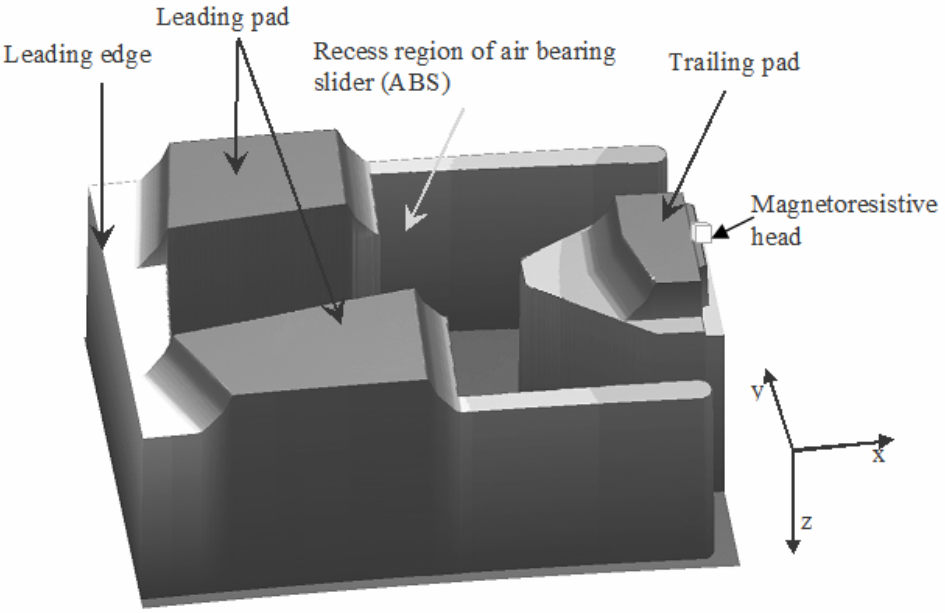

Figure 4.1. An example slider.

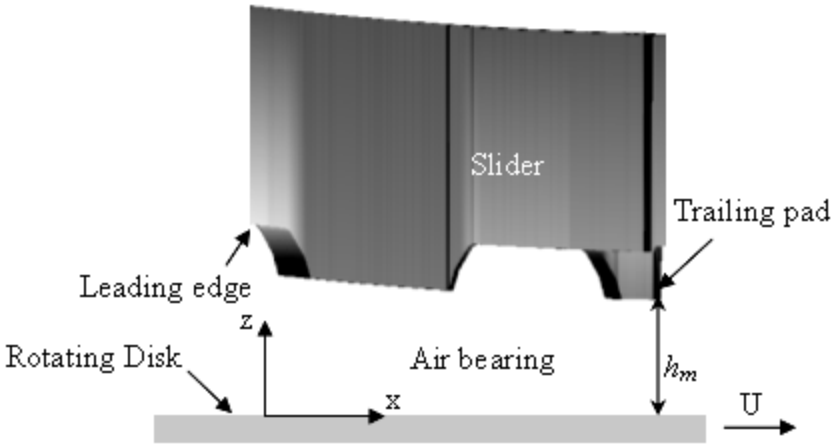

Figure 4.2. A sketch of slider-disk assembly and Cartesian coordinates.

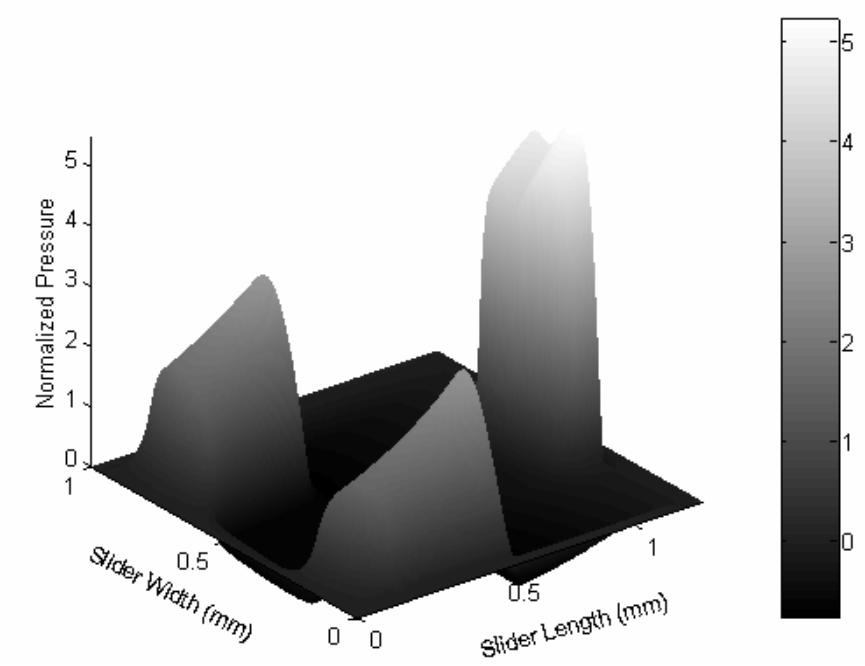

Figure 4.3. Pressure profile of the air-bearing slider.

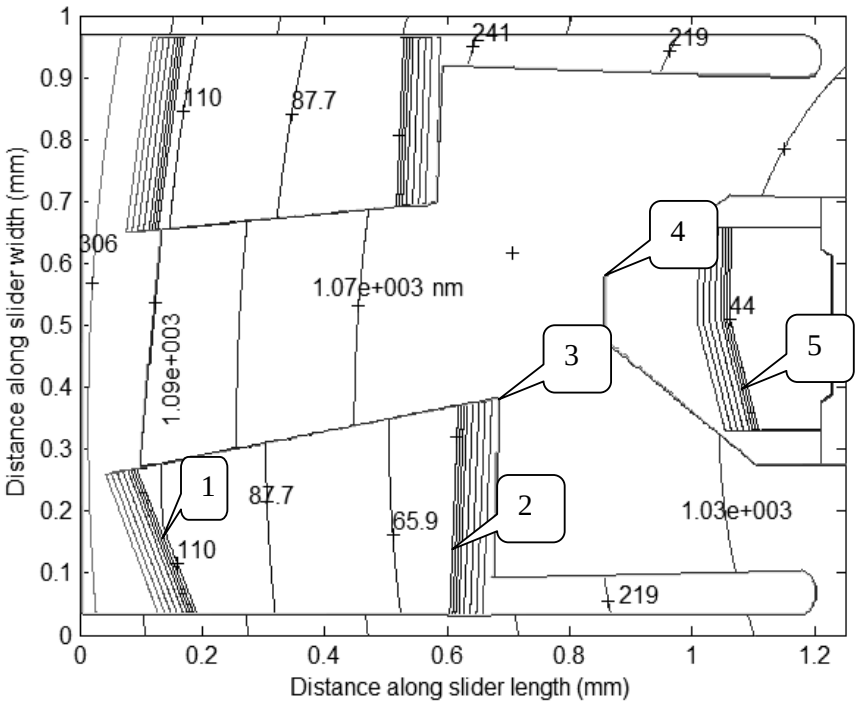

Figure 4.4. Spacing between the slider and disk surfaces and locations for comparing the forces of 2-D and 3-D modeling.

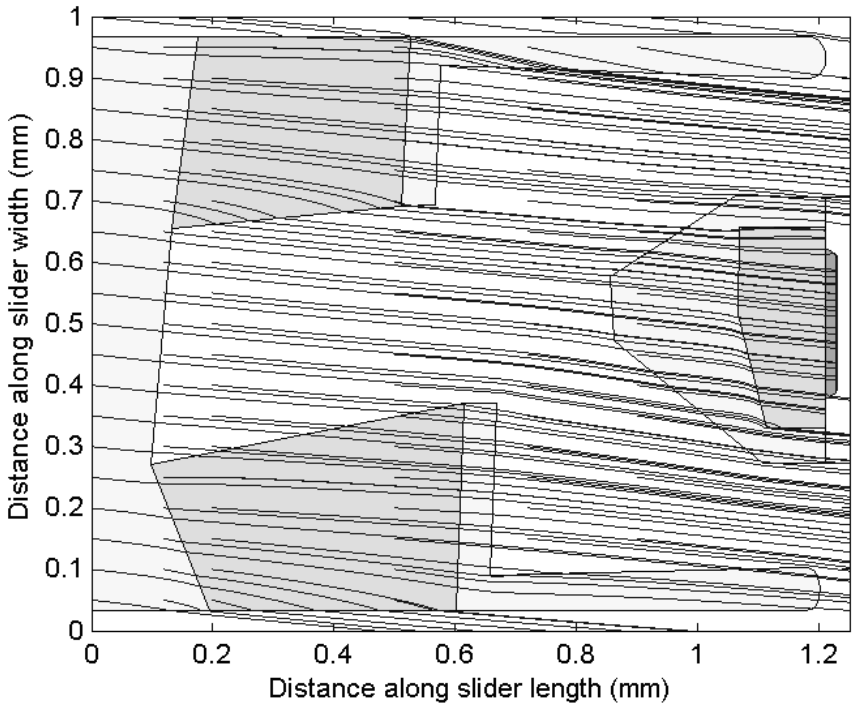

Figure 4.5 (a). Air streamlines at heights of 1% of the slider spacing above the disk.

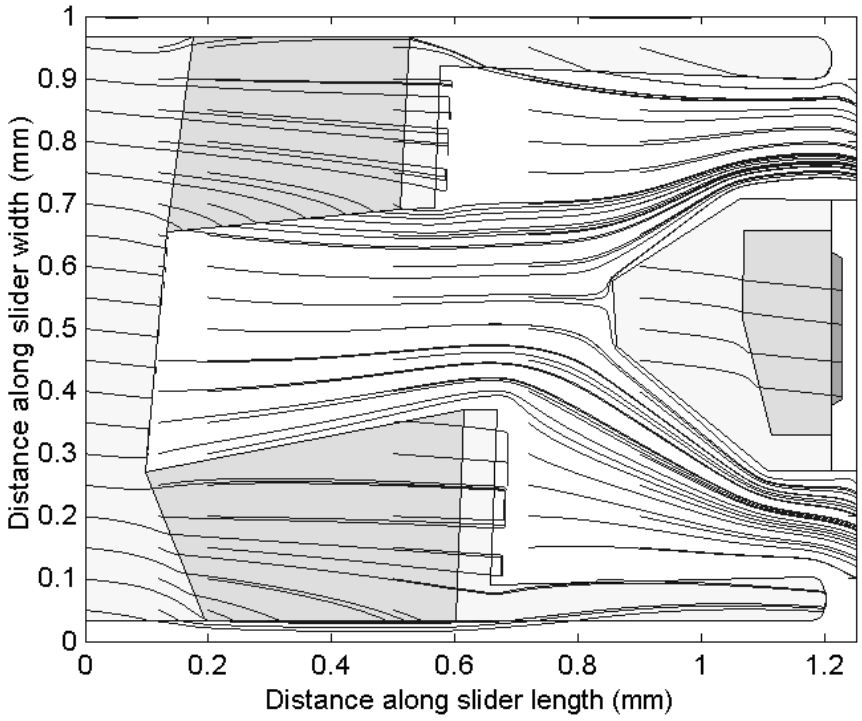

Figure 4.5 (b). Air streamlines at heights of 50% of the slider spacing above the disk.

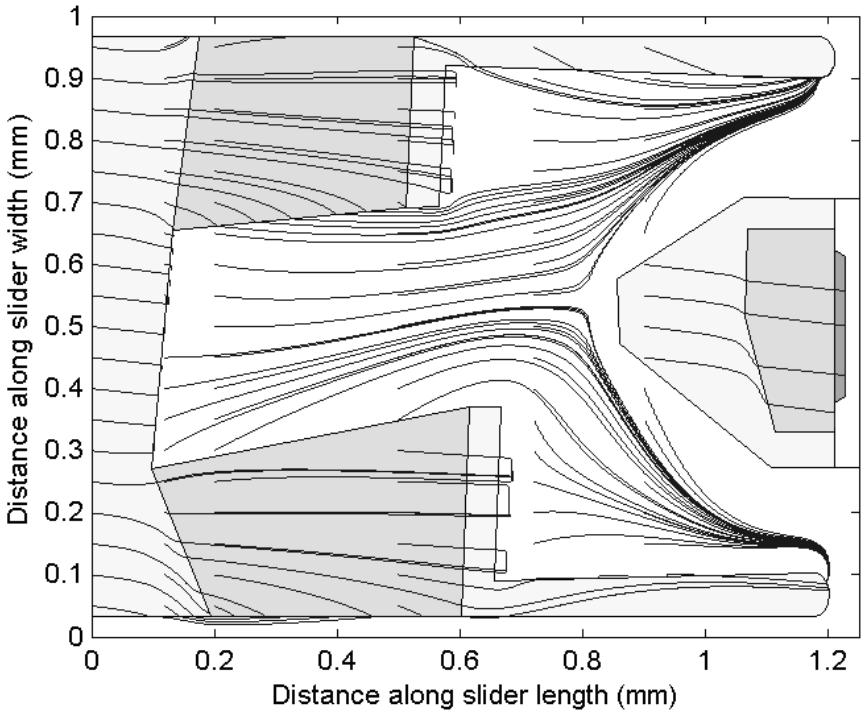

Figure 4.5 (c). Air streamlines at heights of 99% of the slider spacing above the disk.

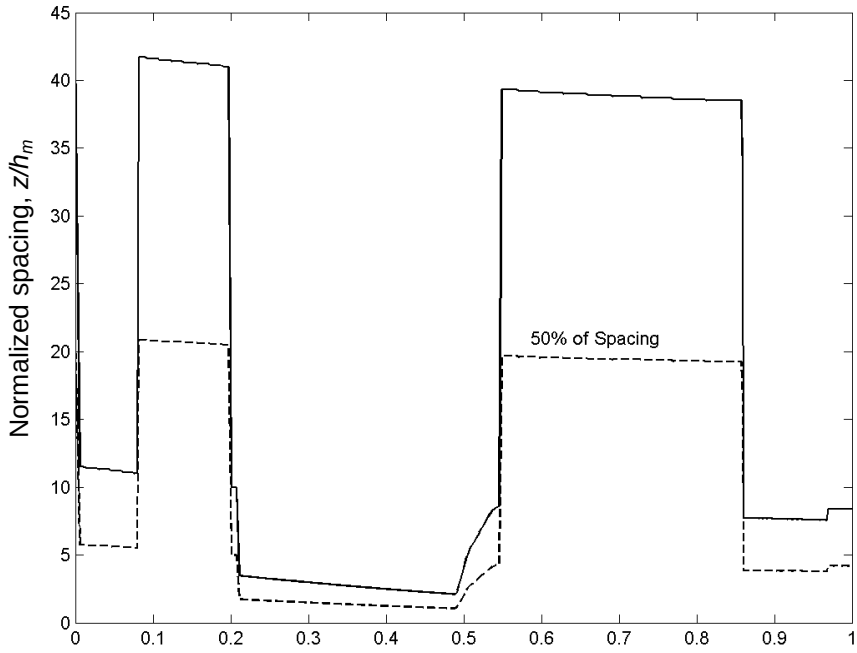

Distance along slider length, *x/xl*.

Figure 4.6. Spacing between the slider and disk surfaces at y=0.3 mm.

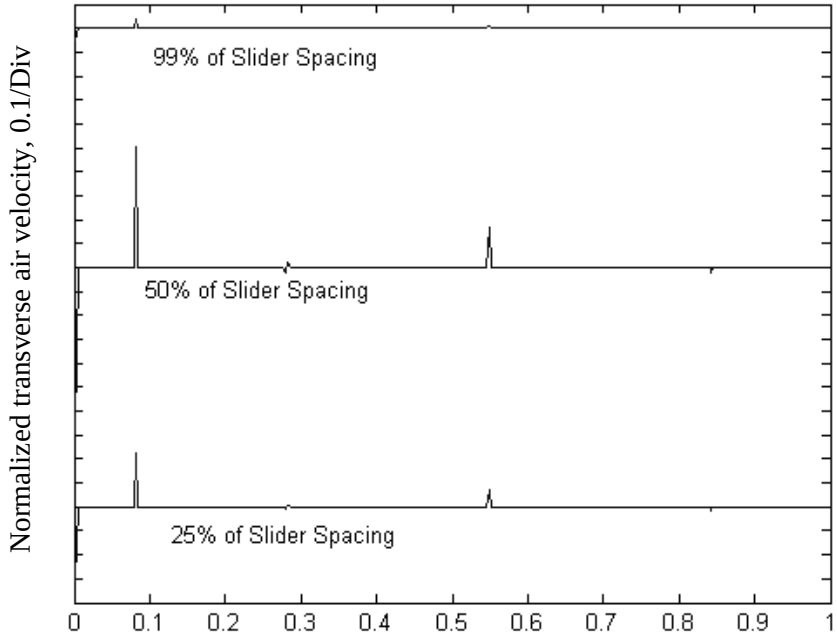

Distance along slider length, *x/xl*.

Figure 4.7. Air vertical velocity in the air-bearing at y=0.3 mm.

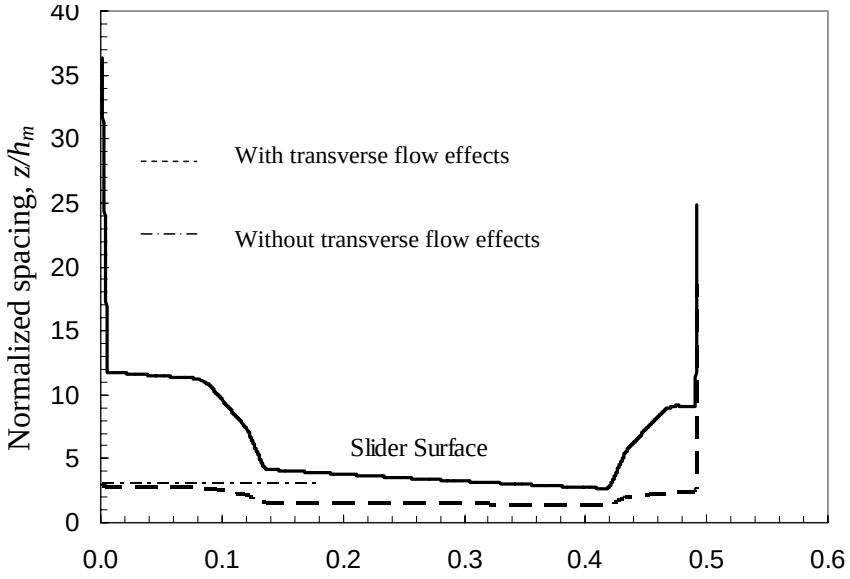

Distance along slider length, *x/xl*.

Figure 4.8. Comparison between particle trajectories using 2-D and 3-D modeling.

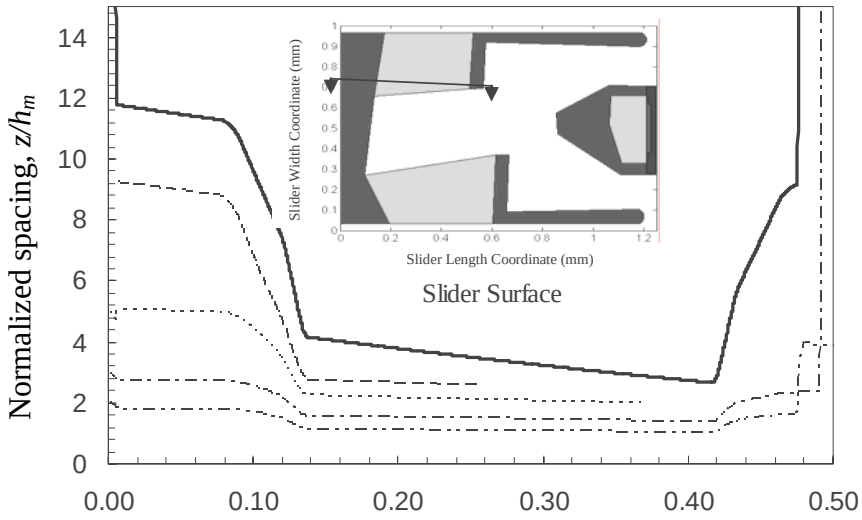

Figure 4.9. Particle flying paths starting at z=2, 3, 5, 9 h_m .

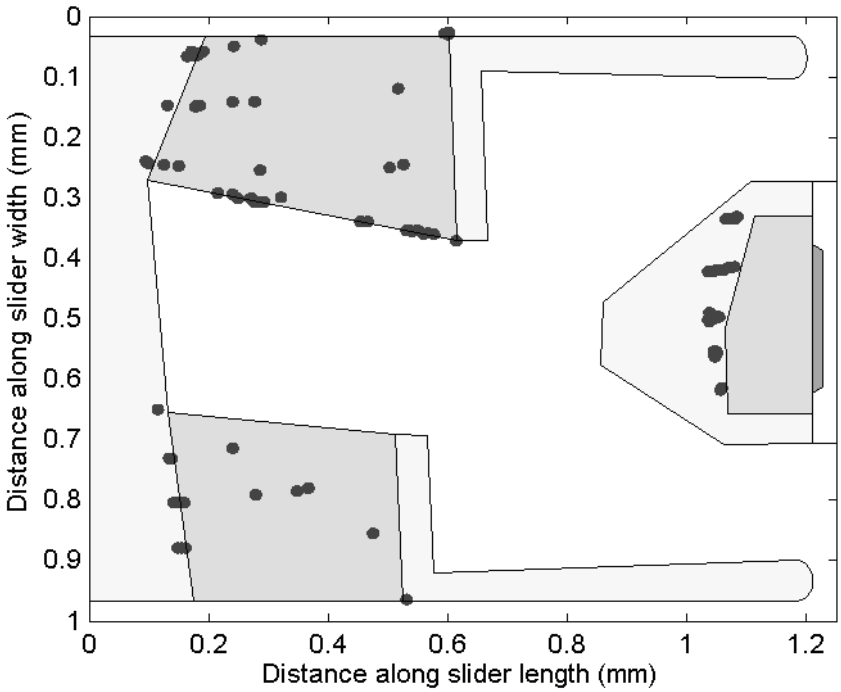

(a) w/o transverse flow

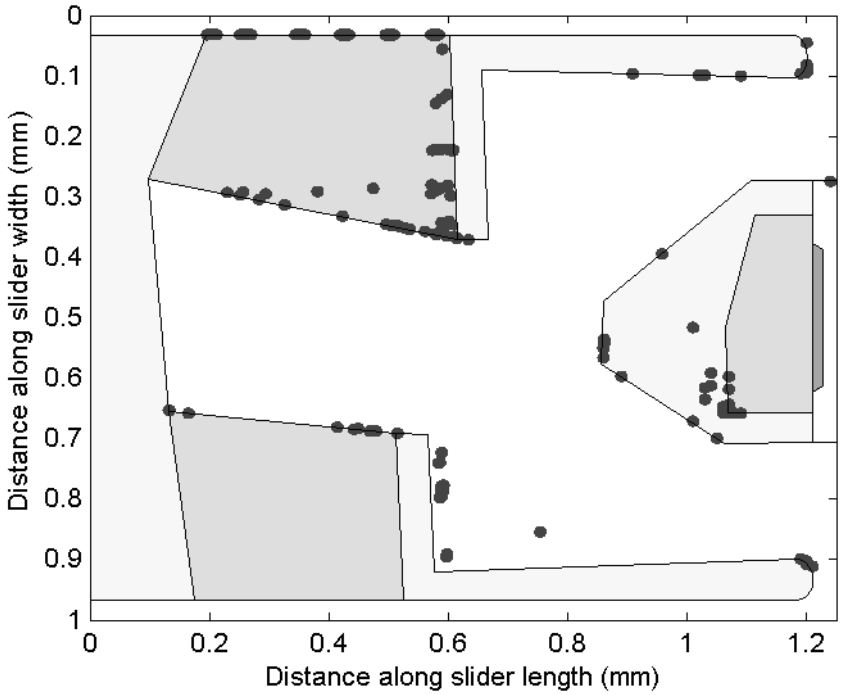

(b) with transverse flow

Figure 4.10. Comparison between particle contamination profiles using analysis without and with transverse flow effects.

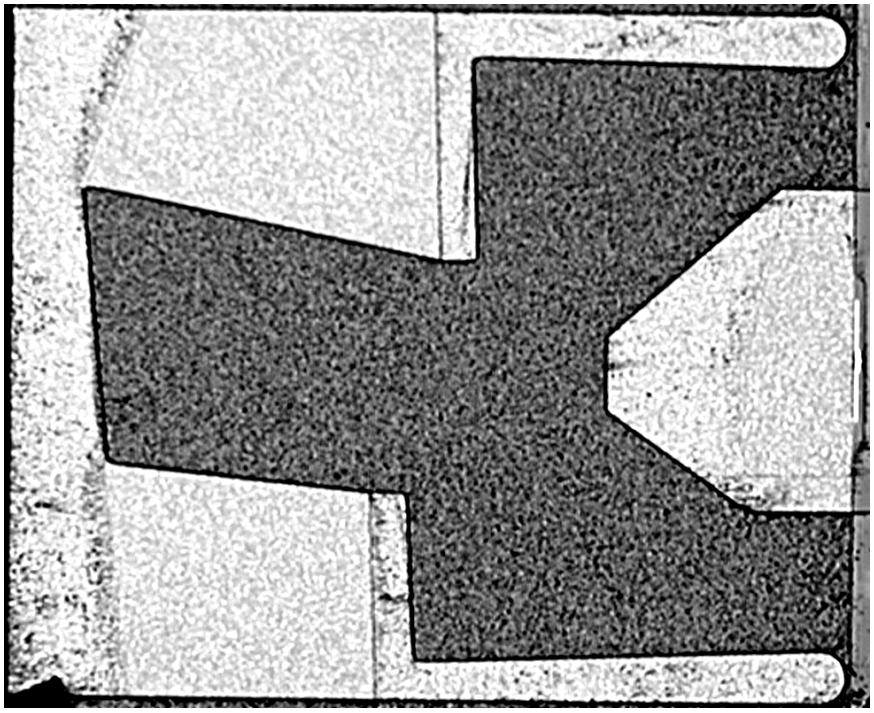

Figure 4.11. Experimentally observed particle contamination profile on the slider.

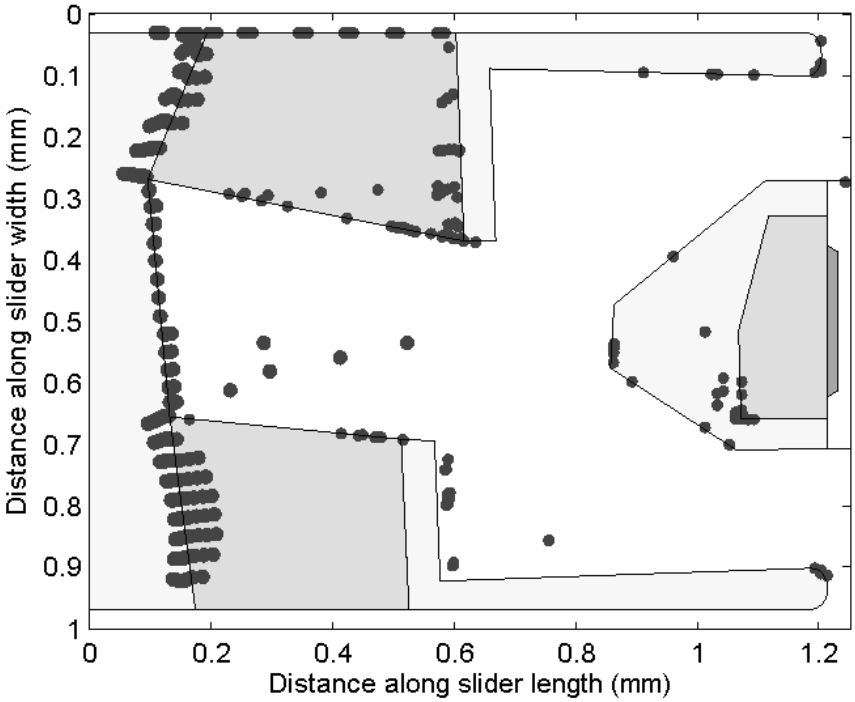

Figure 4.12. Numerically simulated particle contamination profile for the same slider.

Table 4.1 Comparison between forces in 2-D and 3-D modeling

Locations in Figure 4	Drag Force (10^{-9} Micro Newton)		Saffmann Lift Force (10^{-9} Micro Newton)	
	2-D	3-D	2-D	3-D
1	-0.001	-0.5	0.003	0.005
2	0.014	4.0	0.014	0.2
3	0.1	16	0.25	0.02
4	-0.2	-100	0.1	0.07
5	-0.04	-0.2	0.014	0.015

CHAPTER 5

CONTACT FORCE AND FRICTIONAL HEATING DUE TO "LARGE" PARTICLES

Particles in the head disk interface may cause large contact forces acting on the slider as well as thermal asperities in the read/write signal. This is especially true for the close spacing required for 1Tbit/in^2. In this chapter, a three-body contact model is employed to study the effects of a particle entrapped between a slider and disk. A criterion for determining a particle's movement pattern is proposed. The study of particles in the head disk interface shows that large particles are likely to slide between the slider and disk interface, and the particles going through the trailing pad of an air bearing slider cause severe contact forces on the slider and generate significant heat sources. The frictional heating study shows that the temperature around the magnetoresistive (MR) head increases about 5 ^{0}C for a single 200nm particle passing through the trailing pad of the slider. The effects of the particle size, disk material and friction coefficient are also studied. It is found that the disk and slider materials and the frictional coefficient between the materials largely affect the contact force acting on the slider by an entrapped particle as well as the temperature rise at its contact region. It is also found that the friction coefficient largely affects a particle's movement pattern in the head disk interface.

5.1. Introduction

With the evolution of magnetic recording disk technology the flying height of the sliders has decreased dramatically. Currently, the minimum flying height for 1Tbit/in^2 is targeted to be as low as 3.5 nm. With such narrow spacing between the slider and disk surfaces the flow of particles and their contamination on slider surfaces and their effects in the head disk interface become a major concern. The possible effects for a particle entering the air bearing include modulation of the flying height, abrasive wear and mechanical scratching of the magnetic disk surface, and thermally induced spikes in the read-write signal as illustrated in Fig. 5.1. Flash events introduced near MR transducers modify the MR signal because of the dependence of the coil's electrical resistance on temperature, while mechanical scratching on magnetic disk surfaces may cause permanent data loss. Those effects depend on the size and other properties of the particles as well as their interaction with the slider and magnetic disk surfaces. Therefore, proper slider design is necessary to reduce the particles' chances of entering the air bearing, contacting the slider and disk surfaces, and contaminating the slider surfaces.

For a slider flying over a rotating disk one possible phenomenon is that of a large particle falling off the slider, and going into the head disk interface. For these large particles entrapped between the air bearing slider and disk surface the effect on the slider's dynamic performance is more severe for lower flying sliders. The contact force causes the slider's flying height to fluctuate. Therefore, the head media spacing gets modulated, which is critical for 1Tbit/in^2 magnetic hard disk drives.

Recently, Khonsari et al. [26] studied the abrasive failure of hydrodynamic bearings induced by an abrasive particle. By modeling a particle penetrating into two plate surfaces, they predicted the critical particle size causing a scuffing failure. For a

particle sliding on a surface under a normal force one well-known phenomenon is frictional heating [25]. In the head disk interface one major concern is magnetoresistive (MR) head read back signal change due to the local heating near the head. Chen et. al. [5] studied the thermal dependence of the MR signal on slider flying height. They found that the MR element's resistance changed linearly with temperature change. The temperature rise due to a particle entrapped between the trailing pad of a slider and disk can be quite large.

In this Chapter we study the effects of relatively large particles in the head disk interface. First, the three-body contact model is employed for a particle entrapped between an air bearing slider and disk. A criterion for determining the particle's movement pattern is also proposed. A detailed study of particles in a head disk interface shows that larger particles are likely to slide between the slider and disk, and particles going through the trailing pad of an air bearing slider cause a severe contact force on the slider and generate large heat flux. The frictional heating study shows that the temperature around the MR head increases for particles passing through the trailing pad. The effects of the particle's size and disk materials are studied. It is found that, as expected, the disk and slider materials also affect the contact force acting on the slider by a particle.

5.2. Three-body abrasive modeling

For a particle partially penetrating into a disk surface and scuffing on the slider surface as shown in Fig. 5.2, the forces exerted by the particle depend on the penetration depths as well as the slider and disk materials [26].

Let r_1, r_2 be the contact radii at the particle-slider and particle-disk interfaces, respectively. The normal loads acting on the slider and disk surfaces by the particle are:

$$F_s = \frac{\pi}{2} r_1^2 H_s \tag{5.1}$$

$$F_D = \frac{\pi}{2} r_2^2 H_D \tag{5.2}$$

where H_s and H_D are the slider and disk material hardnesses, respectively. The friction coefficients between the particle and disk and particle and slider are μ_D and μ_s, respectively. Therefore, the friction forces are given as:

$$f_s = \frac{\pi}{2} \mu_s r_1^2 H_s \tag{5.3}$$

$$f_D = \frac{\pi}{2} \mu_D r_2^2 H_D \tag{5.4}$$

The contact radii r_1 and r_2 are determined by the geometrical constraints between the penetration depth and the spacing between the slider and disk surfaces. For two parallel plates, we have

$$h + D_s + D_d = 2R \tag{5.5}$$

where h is the spacing between the slider and disk surface; D_s is the penetration depth into the slider; D_d is the penetration depth into the disk; R is the particle's radius.

Geometrically,

$$r_1^2 = 2R \cdot D_s - D_s^2 \,,\; r_2^2 = 2R \cdot D_d - D_d^2 \,. \tag{5.6}$$

For a particle entrapped between an air bearing slider and disk,

$$F_s = F_D \tag{5.7}$$

Therefore,

$$\frac{r_2^2}{r_1^2} = \frac{H_s}{H_D} = \alpha \tag{5.8}$$

Substituting Eq. (5.7) into the first equation in (5.6), we obtain

$$\frac{r_2^2}{\alpha} = 2R \cdot D_s - D_s^2 . \tag{5.9}$$

Substituting Eq. (5.5) into the second equation in (5.6), results in

$$r_2^2 = \left(h + D_s\right)\left(2R - h - D_s\right). \tag{5.10}$$

Combining Eq. (5.9) and (5.10), we obtain the following equation for the penetration depth on the slider,

$$\alpha\left(2R \cdot D_s - D_s^2\right) = \left(h + D_s\right)\left(2R - h - D_s\right). \tag{5.11}$$

The solution of this equation is

$$D_s = \frac{R(\alpha - 1) + h - \sqrt{\left[R(\alpha - 1) + h\right]^2 - (\alpha - 1)h(2R - h)}}{\alpha - 1}, \tag{5.12}$$

which is suitable for $\alpha \neq 1$. For $\alpha = 1$, $D_s = \dfrac{2R - h}{2}$. The contact radii r_1 and r_2 can be calculated from Eqs. (5.6) and (5.9), respectively.

5.3. Criteria for movement of a particle entrapped in a head disk interface

A particle moving in the head disk interface can be sliding or rolling. The movement pattern is determined by the driving moment and resistive moment acting on the particle. As illustrated in Fig. 5.2, the driving moment for a particle to roll is provided by the friction force, which is determined by

$$M_D = f_s h . \tag{5.13}$$

The resistive moment preventing a particle from rolling is the moment due to the normal force acting on the slider, which is

$$M_R = F_S e\,. \tag{5.14}$$

Here $F_S = F_D = F$, and e is the effective moment arm for the normal force. Assuming that the pressure acting on the particle is uniformly distributed across the contact area, we get

$$e = \frac{4}{3\pi}(r_1 + r_2)\,. \tag{5.15}$$

The condition for a particle to roll is

$$M_D = f_s h > M_R = F_S e\,, \tag{5.16}$$

which becomes

$$\frac{e}{h} < \frac{f_s}{F_S} = \mu_s\,, \tag{5.17}$$

where μ_s is the friction coefficient between the particle and slider for the rolling motion. If the resistive moment is larger than the driving moment, the particle will slide along the slider. In this case,

$$\frac{e}{h} > \frac{f_s}{F_S} = \mu_k\,. \tag{5.18}$$

Therefore, the sliding friction coefficient is larger than the rolling friction coefficient. The unified criteria for determining a particle's movement pattern are

Particle rolling

$$\frac{e}{h} < \mu_s\,. \tag{5.19}$$

Particle sliding

$$\frac{e}{h} > \mu_s . \tag{5.20}$$

5.4. Flash temperature for sliding particles

For a particle sliding on a stationary body, the maximum temperature rise on the stationary body is determined by [25]

$$\Delta T = \frac{2qr_1}{\kappa_s \sqrt{\pi}}, \tag{5.21}$$

where q is the heat flux into the slider, r_1 is the contact radius on the slider, and κ_s is the slider material's thermal conductivity. In this case, the heat flux into the slider can be determined by,

$$q = \beta \mu_k U F_S , \tag{5.22}$$

where $\beta = \dfrac{1}{1 + \dfrac{\kappa_P}{\kappa_S}\sqrt{1+Pe}}$ is the heat partition coefficient, $Pe = \dfrac{Ur_1}{2\kappa_P}$ is the Peclet number, and κ_P is the particle material's thermal conductivity.

5.5. Numerical Results and Discussion

A typical slider is chosen, Fig. 5.3, for studying the effect of large particles in the head disk interface. The minimum flying height is 9nm with a pitch angle of 134 μrad at the disk location of 23mm with a skew angle of 9.1 degrees. The important spacings between the air bearing surface and disk surface are shown in Fig. 5.3 at various locations. It is shown that the spacing between the air bearing surface and disk at the leading pad is about 135nm, while the spacing before the leading edge of the air

bearing slider is more than 400nm. At the trailing edge of the slider the spacing decreases dramatically to 9.4 nm where the MR element is located. The decreasing gap induces increasing contact force acting on the air bearing slider as the particle passes through. The material properties of the slider and disk materials used in this paper are given in Table 5.1. We first consider a particle initially located in front of the leading edge of the slider with coordinates x=0.0125 mm and y=0.375mm, which is illustrated in Fig. 5.3. The disk material is first chosen to be Aluminum. The particle is assumed to be rigid. The slider material is $(TiC)_{40\%}(Al_2O_3)_{60\%}$. The contact forces acting on the air bearing slider by particles of size 180nm, 220nm and 240nm, as they move along the slider, are given in Fig. 5.4. The maximum contact force is about 2.7 μN for the 240nm particle while it is 1.2 μN for the 180nm particle at the leading pad of the air bearing slider. Also, it is observed that the 180nm particle rolls between the head and disk interface while the 240nm particle slides.

Currently, many magnetic disk drives are using glass disks. For glass, the indentation depth on the slider will be different than for Aluminum for a given rigid particle, and therefore the contact force acting on the slider will be affected by the disk material. Figure 5.5 shows a comparison between a glass and aluminum disk of the contact force and thermal spike on the slider caused by a 240nm particle. The contact force is 47 μ N when the particle is entrapped between the slider and a glass disk while it is only 2.7 μ N for an aluminum disk. This larger contact force also generates a much larger thermal spike (9.3 ^{0}C) on the slider surface for a friction coefficient of 0.2. The flash temperature also depends on the friction coefficient between the slider and particle. Figure 5.6 illustrates the effect of the friction coefficient on the flash

temperature on the air bearing surface. It shows that for a textured slider (μ=0.5) the temperature rise can be above 23 ^{0}C. The friction coefficient also affects the movement pattern of the particle. It is observed in Fig. 5.6 that the particle begins to slide at x=0.126 mm for the friction coefficient of 0.5. For the friction coefficients of 0.1 and 0.2, the particle begins to slide at x=0.074mm.

For an operating drive many particles may enter the air bearing at the same time. In the simulation 500 particles with size of 200nm enter the air bearing at the leading edge of the slider. These particles have a density of 1.85E3 kg/m^3. At the time t=0.2, 206 particles are entrapped between the slider and disk surfaces, as shown in Fig. 5.7. The maximum contact force by one particle on the slider is 5 μN. However, the total resultant force on the slider is close to 500 μN at t=0.2. This force is large enough to push up the leading pad of the slider. As time evolves, the particles move toward the trailing pad where the MR element is located. The flash temperature at the trailing pad will cause the MR signal to change. It is shown in Fig. 5.8 that these particles cause a temperature rise of 5 ^{0}C at the center of trailing edge at t=0.95.

Also, the total force and moments acting on the slider fluctuate when these particles pass through the head disk interface. As shown in Fig. 5.9, the maximum total force acting on the slider occurs when the particles pass the leading pad of the slider. This is because the total number of particles entrapped between the slider and disk surface reaches the maximum value at this location. When most of the particles fly in the recess region of the air bearing slider the force acting on the slider is negligible, as illustrated in Fig. 5.9. Figure 5.10 shows the pitch and roll moments acting on the slider by these particles. The roll moment is much less than the pitch moment at all times.

Also, the pitch and roll moments reach their maximum values at t=0.2. The contact force and moments created by these particles, as shown in Figs 5.9 and 5.10, can strongly affect the slider's flying height and pitch.

5.6. Conclusions

In this Chapter a three-body contact model is employed to study the effects of a particle entrapped between a slider and disk. A criterion for determining a particle's movement pattern is proposed. A detailed study of particles in a head-disk interface shows that large particles are likely to slide between the slider and disk, and particles going through the trailing pad of an air bearing slider produce severe contact force on the slider, and they generate significant heat flux. The frictional heating study shows that the temperature around the MR element increases about 5^0C for a single 200nm particle passing through the trailing pad. The effects of particle size, disk material and friction coefficient are also studied. It is found that the disk and slider materials and the friction coefficient have a large effect on the contact force acting on the slider by a particle as well as the temperature rise. A glass disk will have a more severe contact force and thermal spike on the slider by particles in the interface while an aluminum disk will be indented more by the particles than the glass disks.

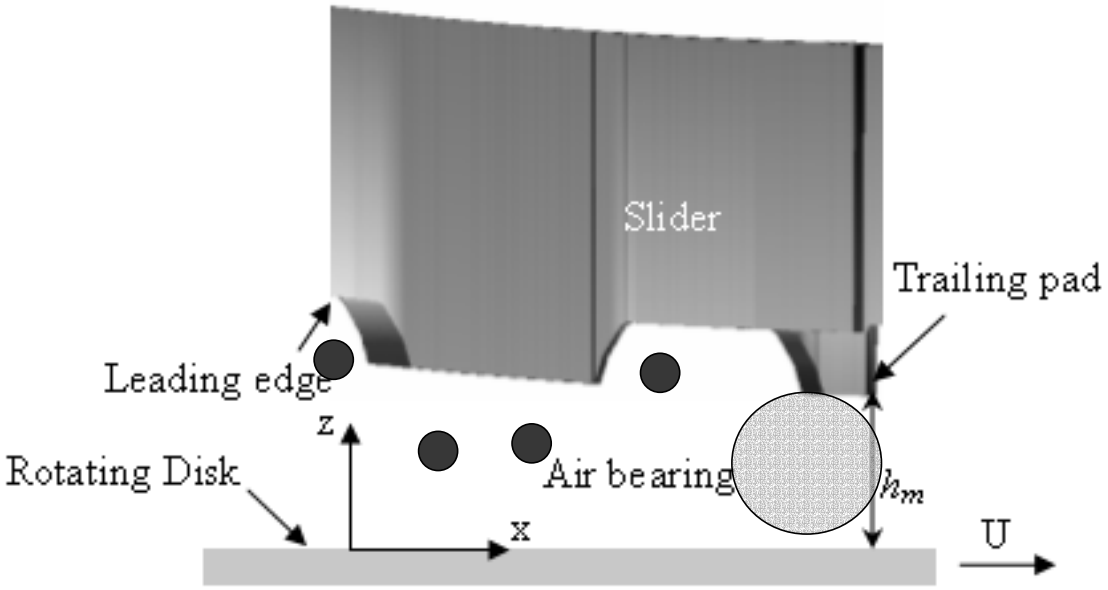

Figure 5.1. A sketch of slider-disk assembly with particles and Cartesian coordinates.

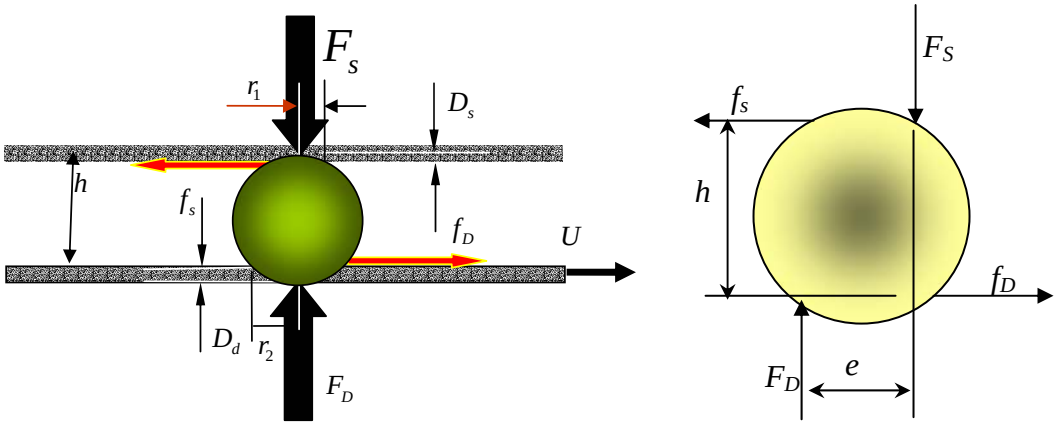

Figure 5.2. Particle entrapped between two parallel surfaces and force diagram.

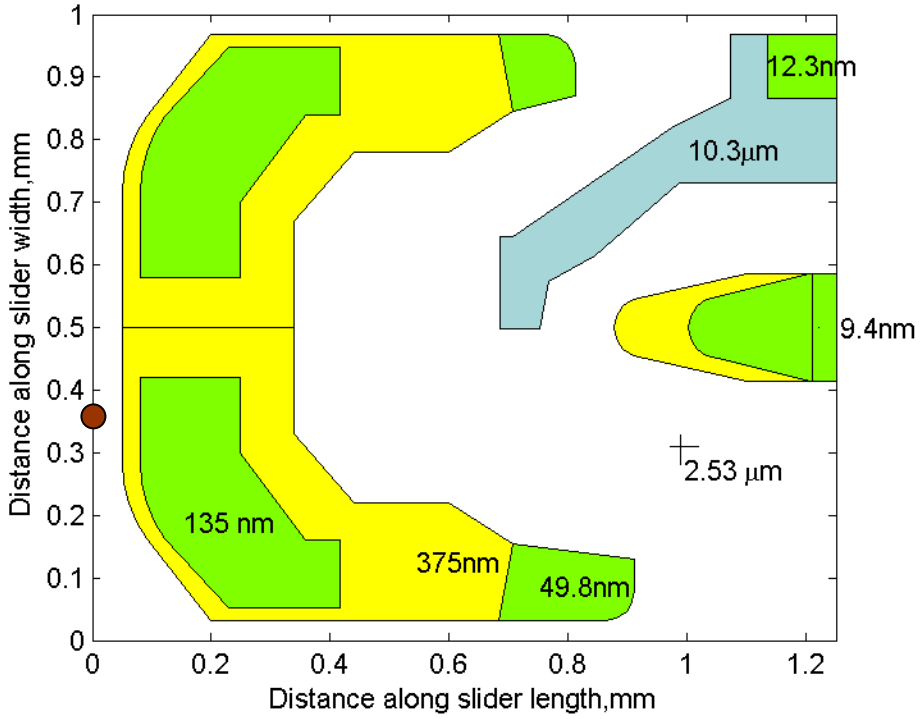

Figure 5.3. An air bearing slider used for studying large particle effect.

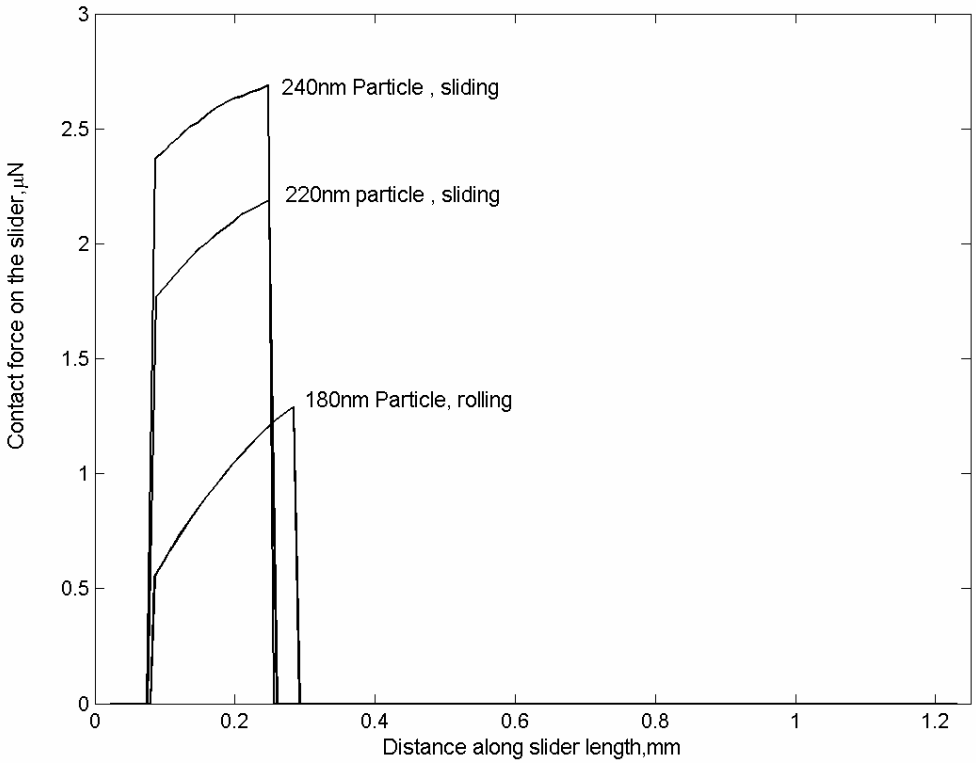

Figure 5.4. Size effect on contact force by a particle between a slider and aluminum disk.

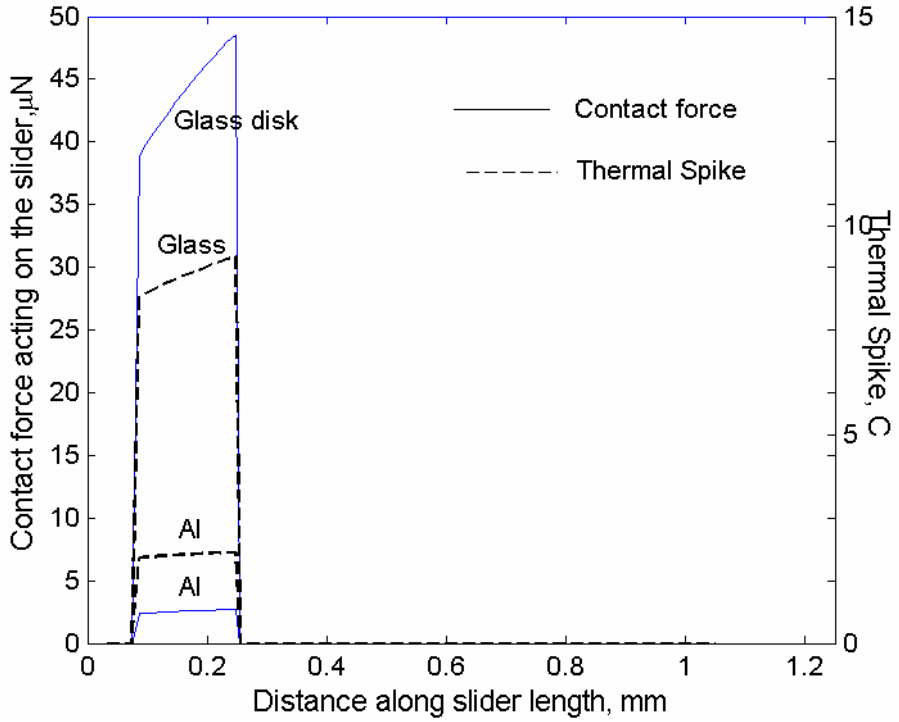

Figure 5.5. Disk material effect on the contact force and thermal spike on the slider by a 240nm particle.

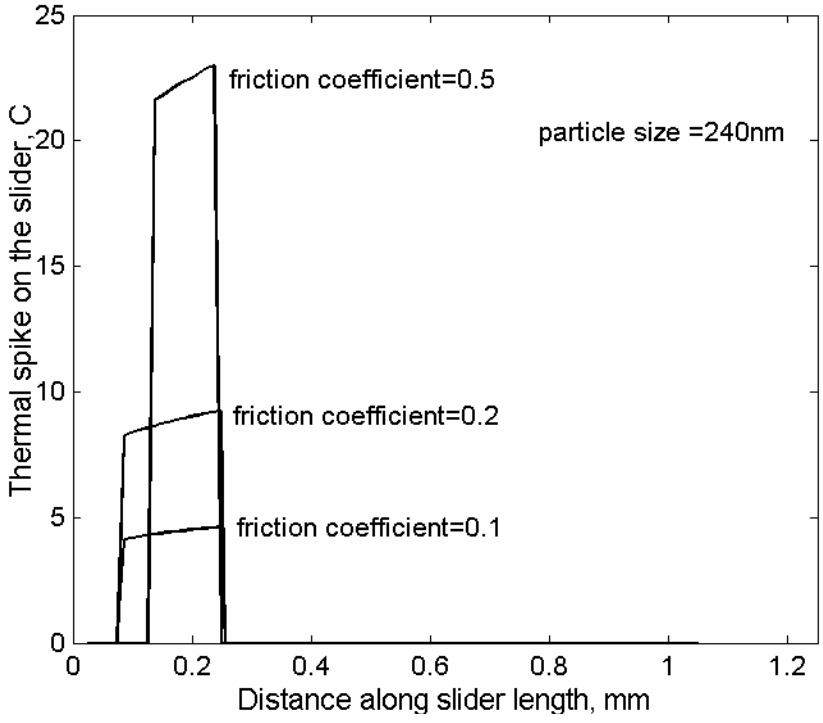

Figure 5.6. Friction coefficient effect on the thermal spike on the slider.

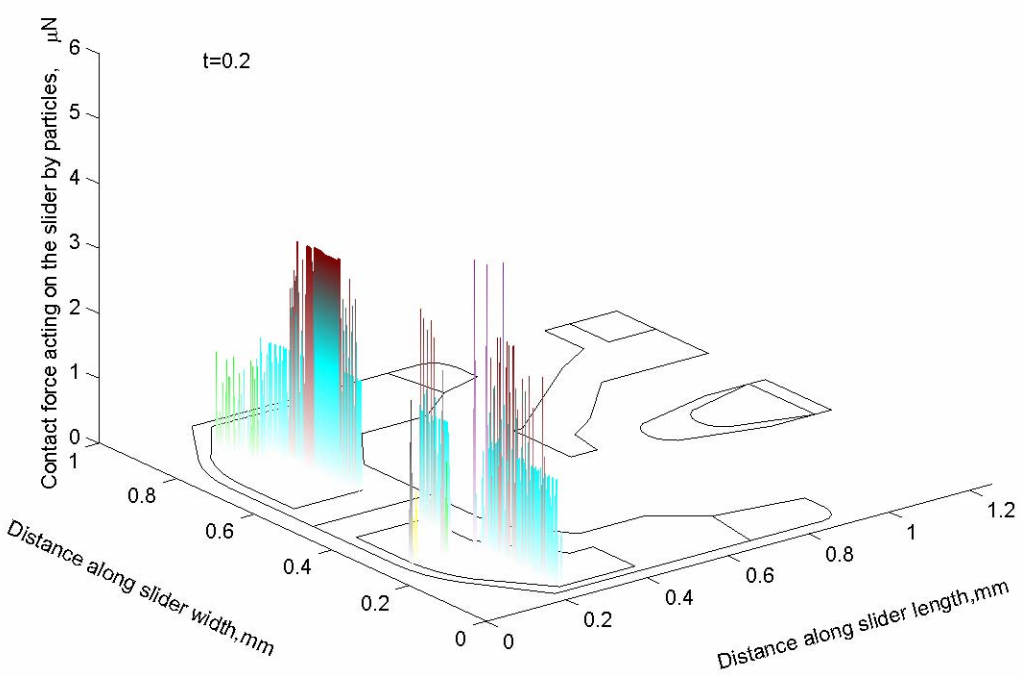

Figure 5.7. Contact force map acting on the air bearing surface at t=0.2.

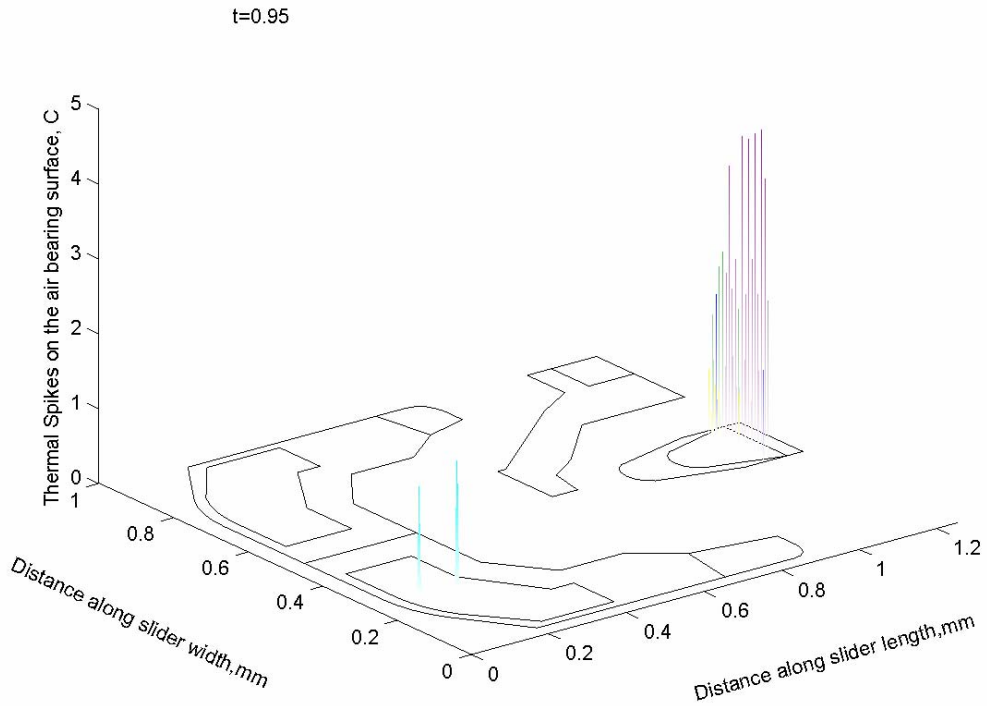

Figure 5.8. Temperature rise on the air bearing surface at t=0.95.

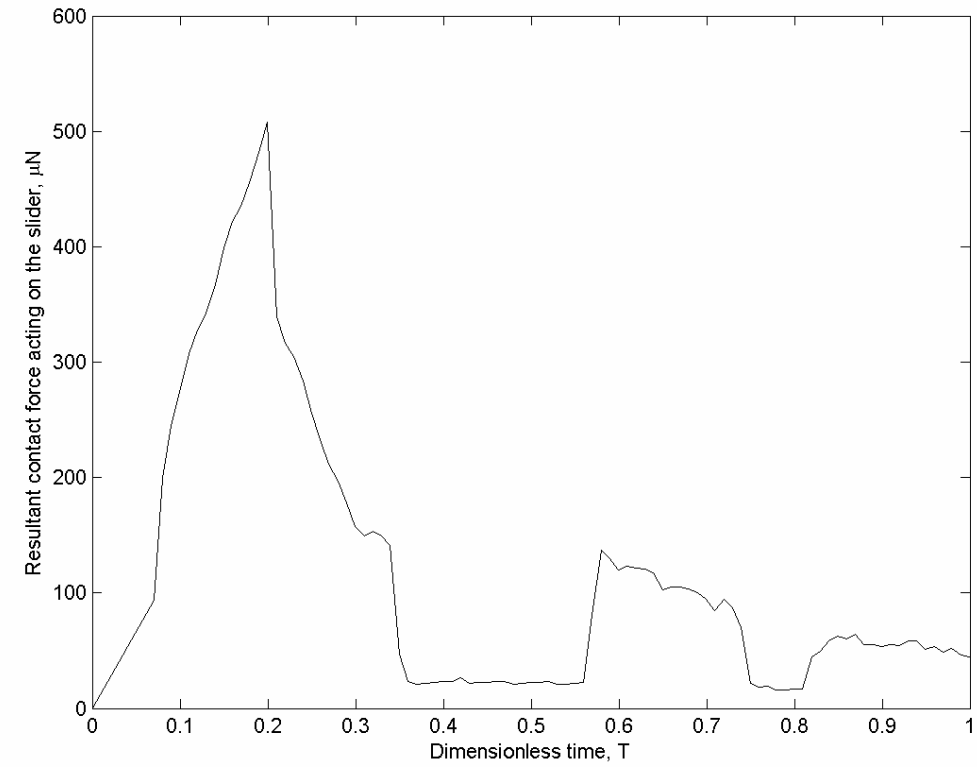

Figure 5.9. Resultant contact force history acting on the slider.

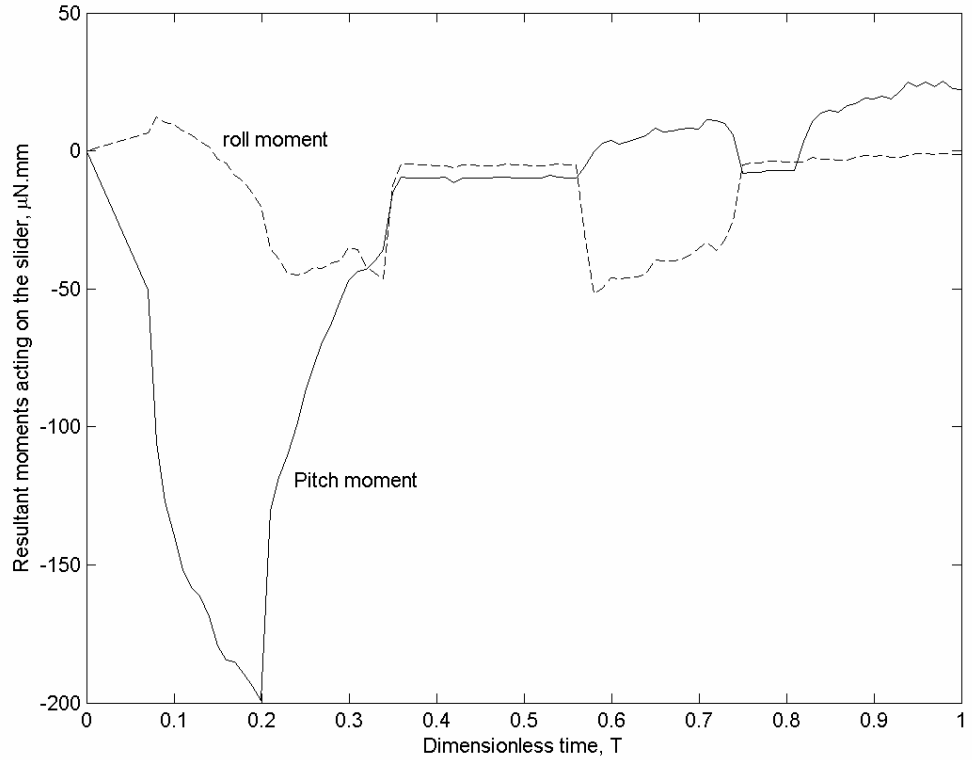

Figure 5.10. Resultant contact force moments' histories acting on the slider.

Table of Contents

Table 5.1 Material properties for slider and disk materials

Materials	Hardness (MPa)	Young's modulus (GPa)	Thermal conductivity (W/m-k)
$(TiC)_{40\%}(Al_2O_3)_{60\%}$	2.42E3	4.39E2	27
Glass	4.77E3	68	1.38
Aluminum	1.2E2	69	166.9

Table of Contents

CHAPTER 6

SLIDER DESIGNS FOR ANTI PARTICLES IN HDI

Due to the transverse flow of the air at the etch steps in current etched-cavity slider air bearing designs in hard disk drives, a contamination particle's flying path in the air bearing can be modified by changing the slider's wall profiles and crown. This will influence the particle contamination on the slider. In this chapter it is shown that the wall profile has a major effect on the particle's path in a slider/disk interface and that one may design the wall profiles of a slider to reduce a particle's likehood of contacting the slider as it passes through the air bearing. In this way there is the potential to minimize the effect of particle contamination on the slider's flying behavior. Also, by increasing the crown of the slider one can increase its pitch angle and also reduce the particle contamination on the air bearing surface.

6.1. Introduction

To achieve the high data density of one terabit per square inch in hard disk drives designers must reduce the flying height of the air bearing to less than 5nm. At such low flying heights contamination particles are very likely to enter the spacing and accumulate on the air bearing surface. The motion of a particle moving through the air bearing from the leading edge to the trailing edge is quite difficult to describe due to the various parameters that may affect the forces acting on the particle. These forces depend on the particle's size, density and the air velocity and pressure fields in the air-bearing. It is desirable to have the particles pass through the head disk interface without contaminating

the ABS. As shown by Shen, et al. [50] the transverse flow in the air bearing at the etch step has an important effect on a particle's flying path. This transverse air flow can be changed by modifying the wall profiles and crown of a slider. By retarding a particle's motion toward the ABS one may reduce the particle's probability of contaminating the slider.

In this Chapter we study some three-dimensional effects of wall profiles and crown on a particle's flying path and the contamination on the slider's ABS. Since the number density of the particles is small, collisions between the particles are assumed to have negligible effect and thus are neglected in this investigation. Furthermore, adhesion of the particles on first impact with the slider or disk is assumed. The air bearing equation, including some three-dimensional flow effects [50], is used in this study to calculate the forces on a particle within an air-bearing based on previous work [60-62]. We then choose some contemporary slider designs and show that modification of the wall profiles causes less transverse force on the particles thereby causing fewer particles to contaminate the ABS. Our results also show that increasing a slider's crown not only increases its pitch angle but also reduces a particle's likehood of contaminating the ABS.

6.2. Wall and crown effects on particle flow and slider contamination in hard disk drives

The reference slider used in these numerical simulations to study the effects of the wall profile and crown is shown in Fig. 6.1. Its 3-D view is shown in Fig. 6.2. From the reference air bearing surface to the first etch level there is a wall profile, which is determined by various manufacturing processes. It is defined as a shallow step wall profile. There is also another wall profile from the shallow etch to the recess region of the

slider. The reference slider's center trailing edge flying height is 26nm with a pitch angle of 56 μrad at a particular location on the disk. We examined three different wall profiles in the numerical experiments. The first wall profile is composed of two straight segments, as shown in Fig. 6.3. The depth from the reference surface to the shallow step is 0.28 micron. The wall profile from the shallow step to the recess region is shown in Fig. 6.4. In the second slider design the curved wall profile shown in Fig. 6.5 is used for the shallow step, while the straight wall profile in Fig. 6.4 is again used from the shallow step to the recess. The third slider has the curved wall profile shown in Figure 6.5 for the shallow step, while the curved wall profile shown in Figure 6 is used from the shallow step to the recess region of the slider. The flying characteristics of these three sliders are listed in Table 6.1. The nominal flying height of each slider is 26nm. Their pitch angles are 56, 62, 64 μrad , respectively.

The transverse air flow in the head disk interface is modified significantly by the changes in the wall profile. Figure 6.7 shows that the transverse air flow velocity at the transition region of the slider with a straight wall profile is 0.17U in the middle of the spacing at y=0.2mm. The transverse air flow is as low as 0.02U at the same location for the slider with a curved wall profile. The two wall profiles corresponding to this major transverse air flow difference are shown in Fig. 6.8. It is seen that the curved wall profile almost eliminates the abrupt transverse flow. Because of the transverse air flow decrease, a 30nm particle can not easily fly toward the ABS at the transition region of the slider and contaminate it. The 30nm particle's flying paths in these two air bearings are shown in Fig. 6.9. The particle's density is 4.25×10^3 kg/m^3. The particles are initially located at

x=0.425mm, y=0.2mm and z=5hm. The particle in the air bearing with the straight wall profile flies toward the slider surface and contaminates it right after the transition region (Figure 6.9(a)). However, the same particle starting from the same position with the same condition for the curved profile passes through the head disk interface without touching the slider's surface, as illustrated in Figure 6.9(b).

In the particle contamination simulations we used 864 alumina particles of 30nm in size. They were initially uniformly distributed close to the disk. Figure 6.10 shows the particle contamination pattern for the original slider design. It is seen that many particles are deposited on the leading pad, and also on the trailing pad of the ABS. In all, 237 particles adhered to the air bearing using the worst-case scenario. For the improved wall profile design, only 76 particles were deposited on the air bearing, as shown in Fig 6.11. No particle is shown on the trailing pad of this slider, and many fewer particles are collected on the leading pad.

To further modify the transverse air flow pattern in an air bearing one may increase the crown to reduce the drag force acting on a particle. Figure 6.12 shows the particle contamination profile on two slider designs with different crowns. The first slider has a crown of 5nm, while the second slider has a crown of 20nm. The minimum flying heights are at 5 and 7nm, respectively. Increasing the crown also increases the pitch angle of the slider, which is desirable for its dynamic performance; but what is the effect of increasing the pitch angle of a slider on particle contamination? From the particle contamination profiles shown in Fig. 6.12 it is seen that many fewer particles are

collected on the air bearing of the slider with 20nm crown. And also, there is no particle at the transition region of the inside leading pad on the 20nm crown slider while many particles are observed there on the slider with 5nm crown. Even though the slider with 20nm crown has a higher pitch angle than the slider with 5nm crown, the total number of particles deposited on the ABS of the 20nm crown slider is 7% less than the number of particles on the other slider, as shown in Table 6.2.

6.3. Effects of channel design on particle flow in the head disk interface

To further control particles in the head disk interface we proposed the channel design as shown in the bottom of Fig. 6.13. The top figure shows an original INSIC design which has a minimum flying height of 5nm with a pitch angle of 215 μrad and a roll angle of 0.01 μrad at the MD location. The bottom figure in Fig. 6.13 shows a modified design with a channel included. Its minimum flying height is 6nm, with a pitch angle of 205 μrad.

Due to the presence of the channel it is expected that many particles will drift to it and away from the trailing pad where the MR element is located. Fig. 6.14 shows the number of particles passing the MR element area for the original design. It is seen that as many as 36 out of 500 particles fly through the MR element area. For the modified design with the channel only 19 particles fly through the MR element area as shown in Fig. 6.15. The improved design reduces the number of particles passing through the MR element area by nearly 50%.

6.4. Conclusions

Due to the effect of transverse flow on a particle's flying behavior in the air bearing it is possible to modify a particle's flying path by changing the wall profiles and crown of a slider. The current study found that the wall profile can have a large effect on the particle contamination pattern on a slider. The curved wall profile is advantageous for reducing particle contamination on the slider's ABS. One such wall profile is shown to reduce the air's transverse flow velocities at the transition regions of a slider. For this slider with curved wall profiles a 70% reduction of the small particle contamination is predicted by the numerical experiments. Also, increasing the crown of a slider's ABS, one not only increases the slider's pitch angle, but also reduces by about 7% the particle contamination for the particular slider studied.

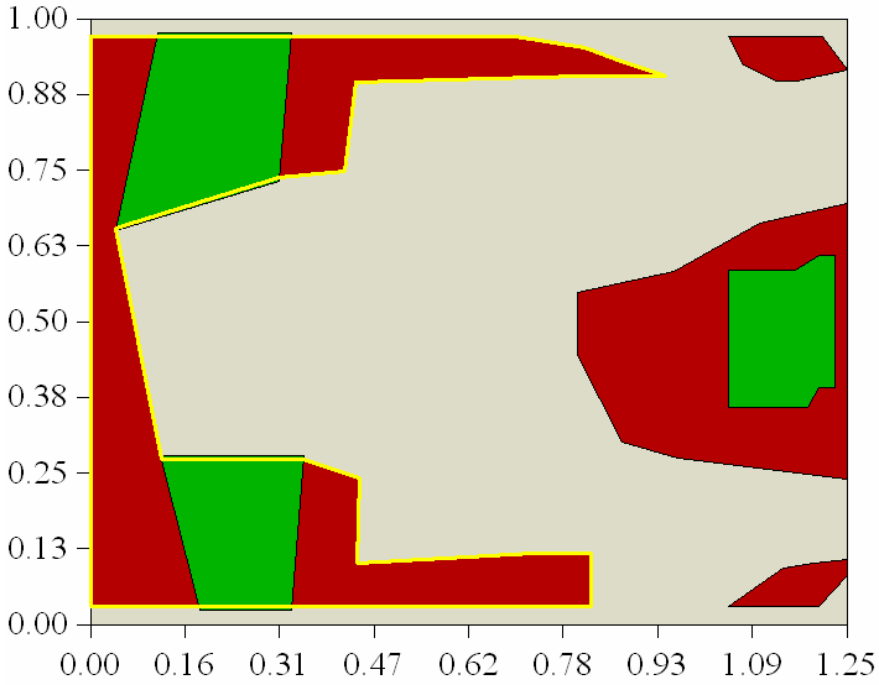

Figure 6.1. A reference slider used to study wall profile and crown effects

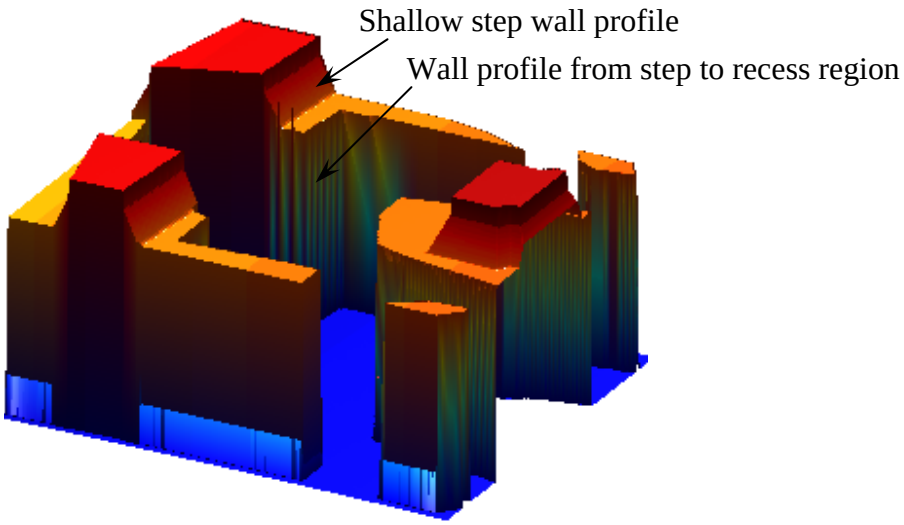

Figure 6.2. 3-D view of the reference slider with original wall profiles

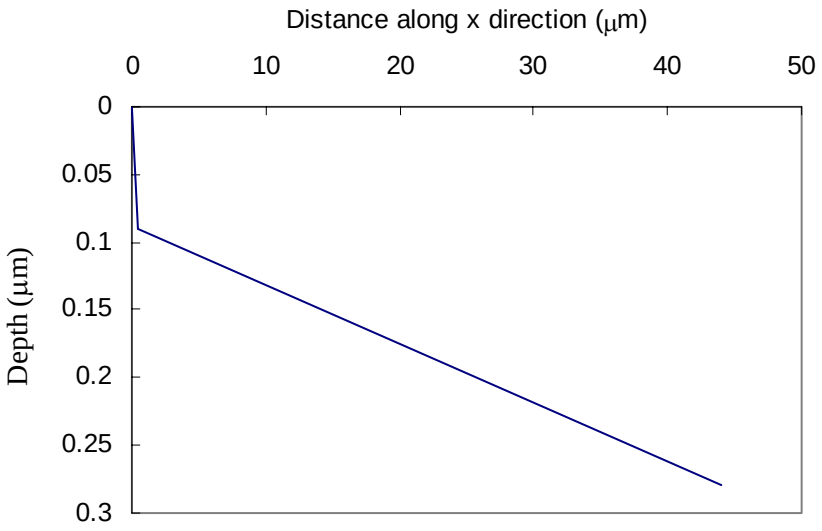

Figure 6.3. Straight segment shallow step wall profile

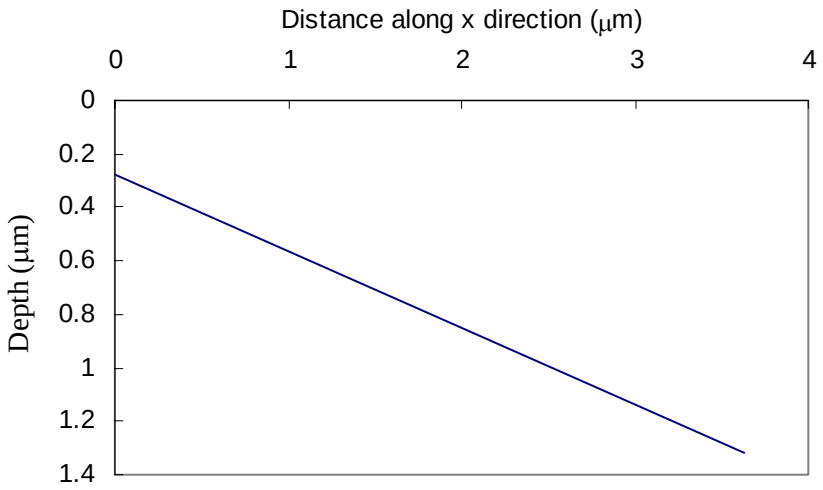

Figure 6.4. Straight wall profile from step to the recess region

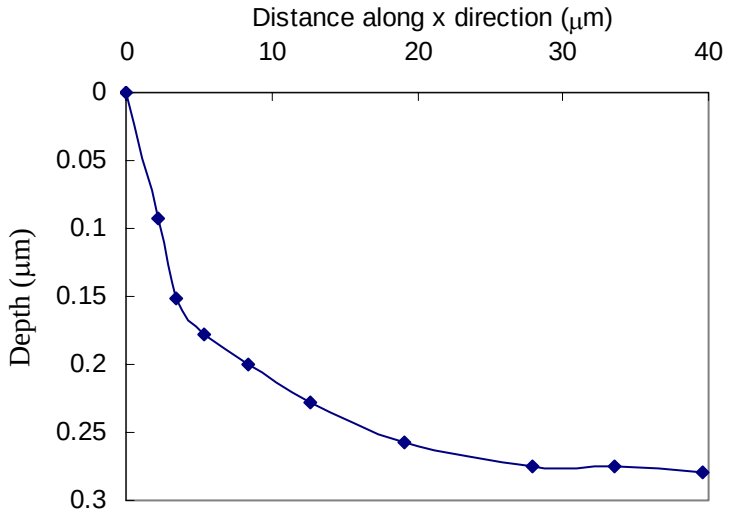

Figure 6.5. Curved wall profile for the shallow step

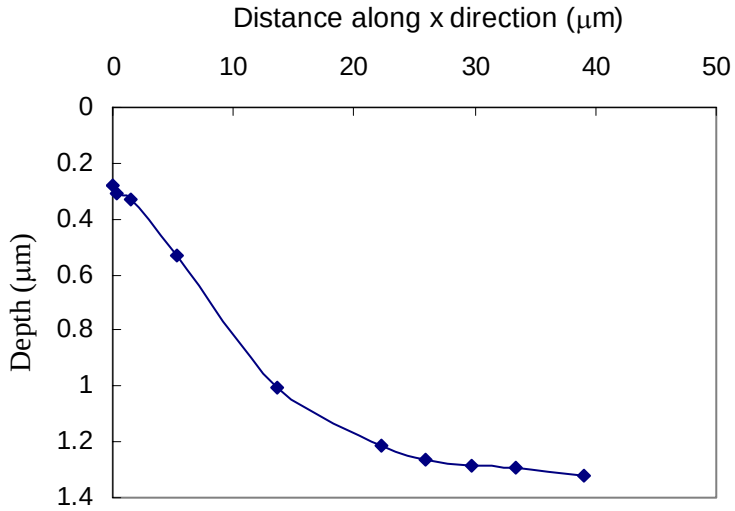

Figure 6.6. Curved wall profile from the shallow step to the recess region

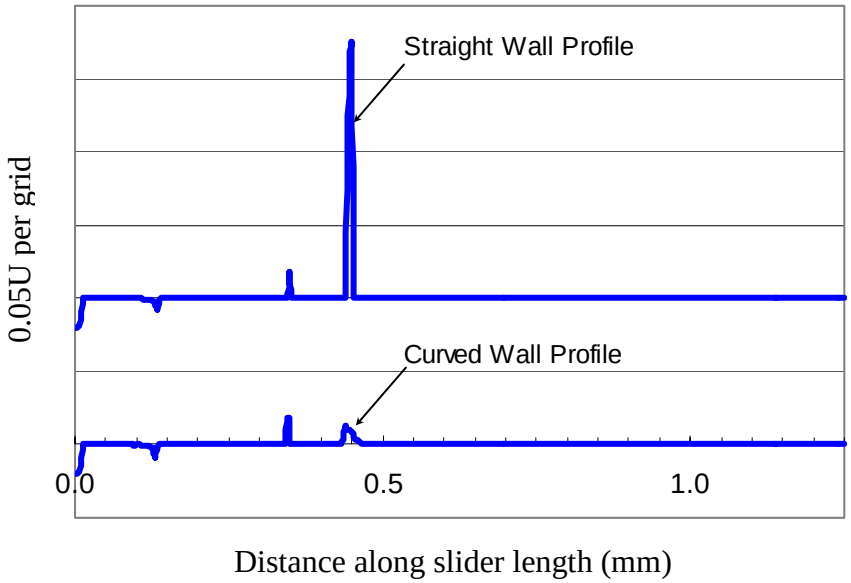

Figure 6.7. Comparison of transverse air velocities between straight and curved wall profiles at 50% of the slider spacing at y=0.2mm

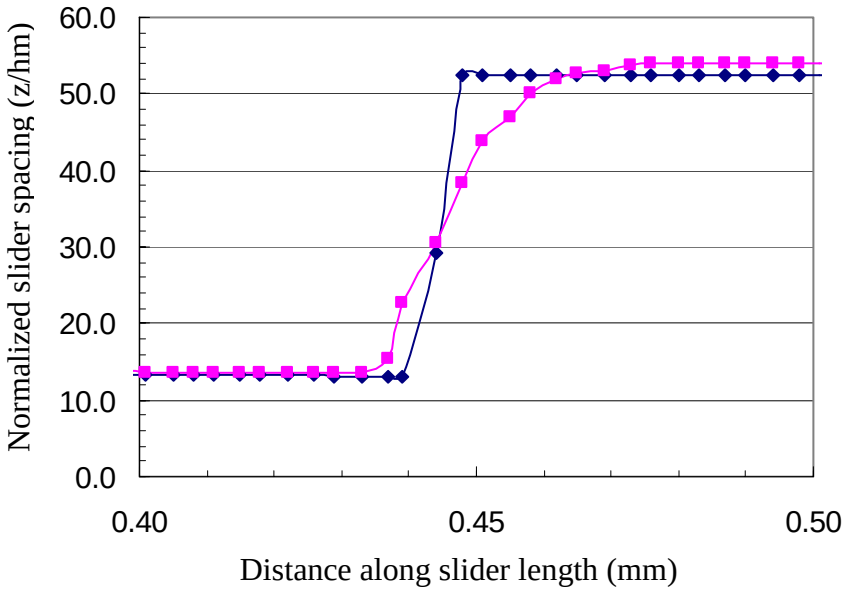

Figure 6.8. Slider spacing using straight and curved wall profiles at y=0.2mm

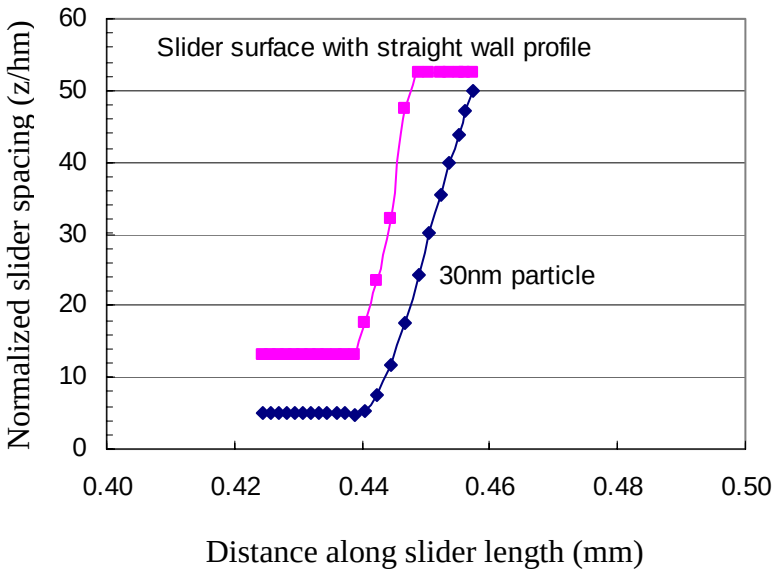

(a) Particle flying path in air bearing with straight wall profile

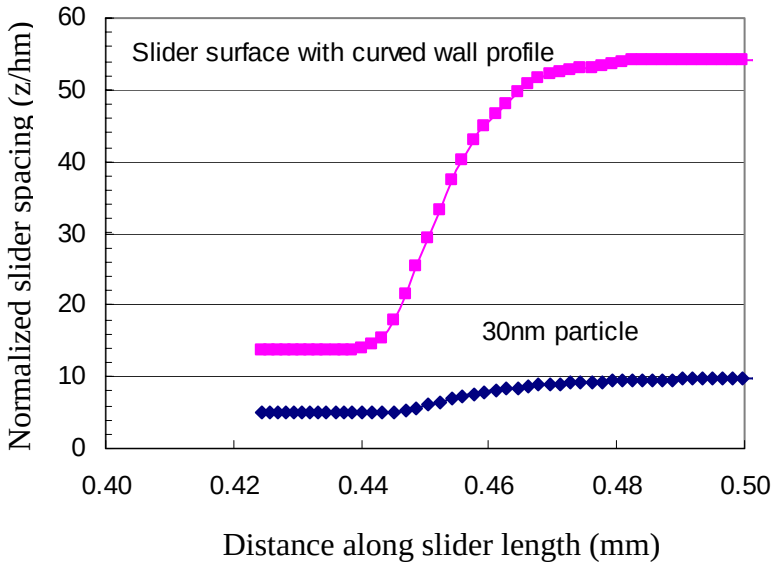

(b) Particle flying path in air bearing with curved wall profile

Figure 6.9. Particle flying paths under sliders with straight and curved wall profiles

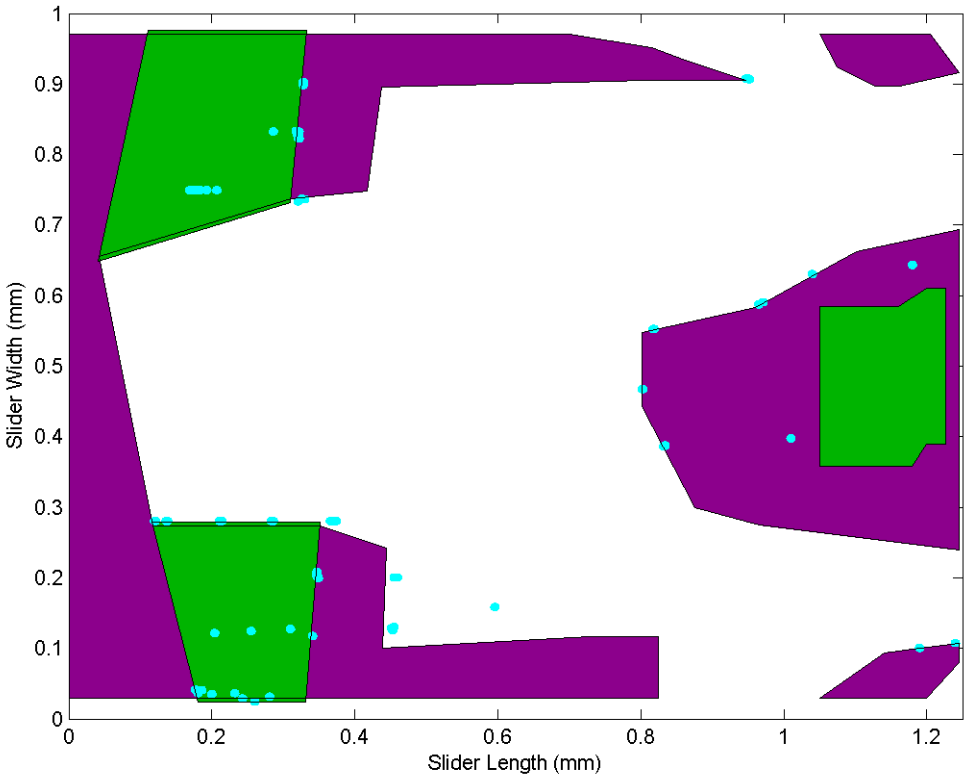

Figure 6.10. Particle contamination profile for the original slider design

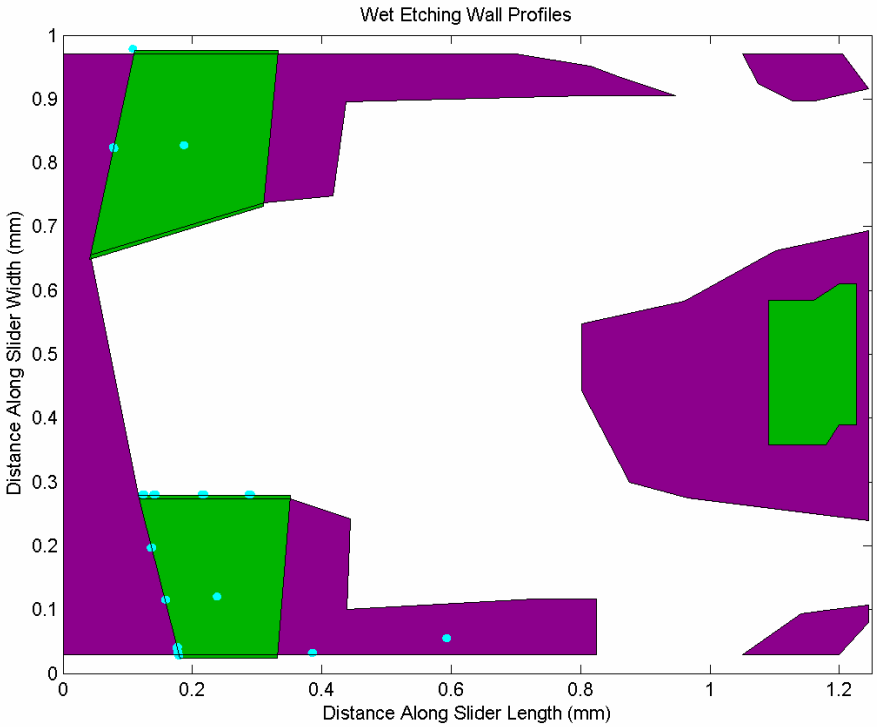

Figure 6.11. Particle contamination profile for the optimized wall profile slider design

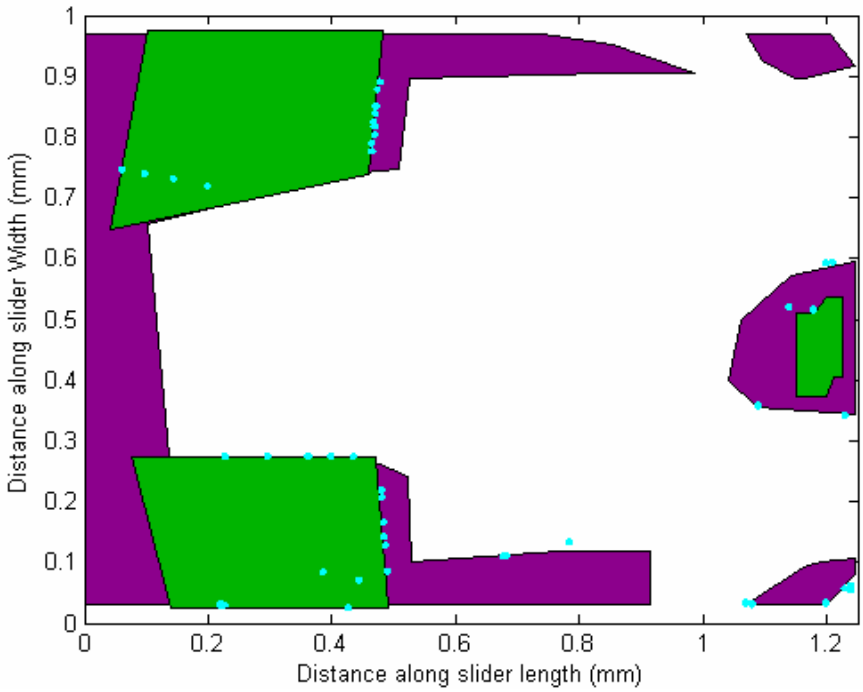

(a) Particle contamination profile on 5nm crown air bearing

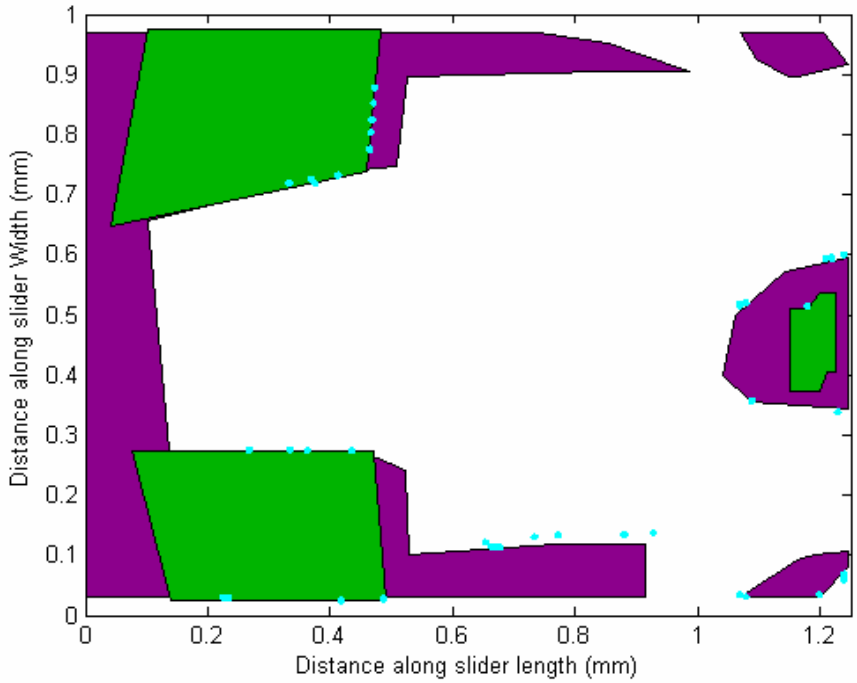

(b) Particle contamination profile on 20nm crown air bearing

Figure 6.12. Crown effects on particle contamination profile on slider air bearings

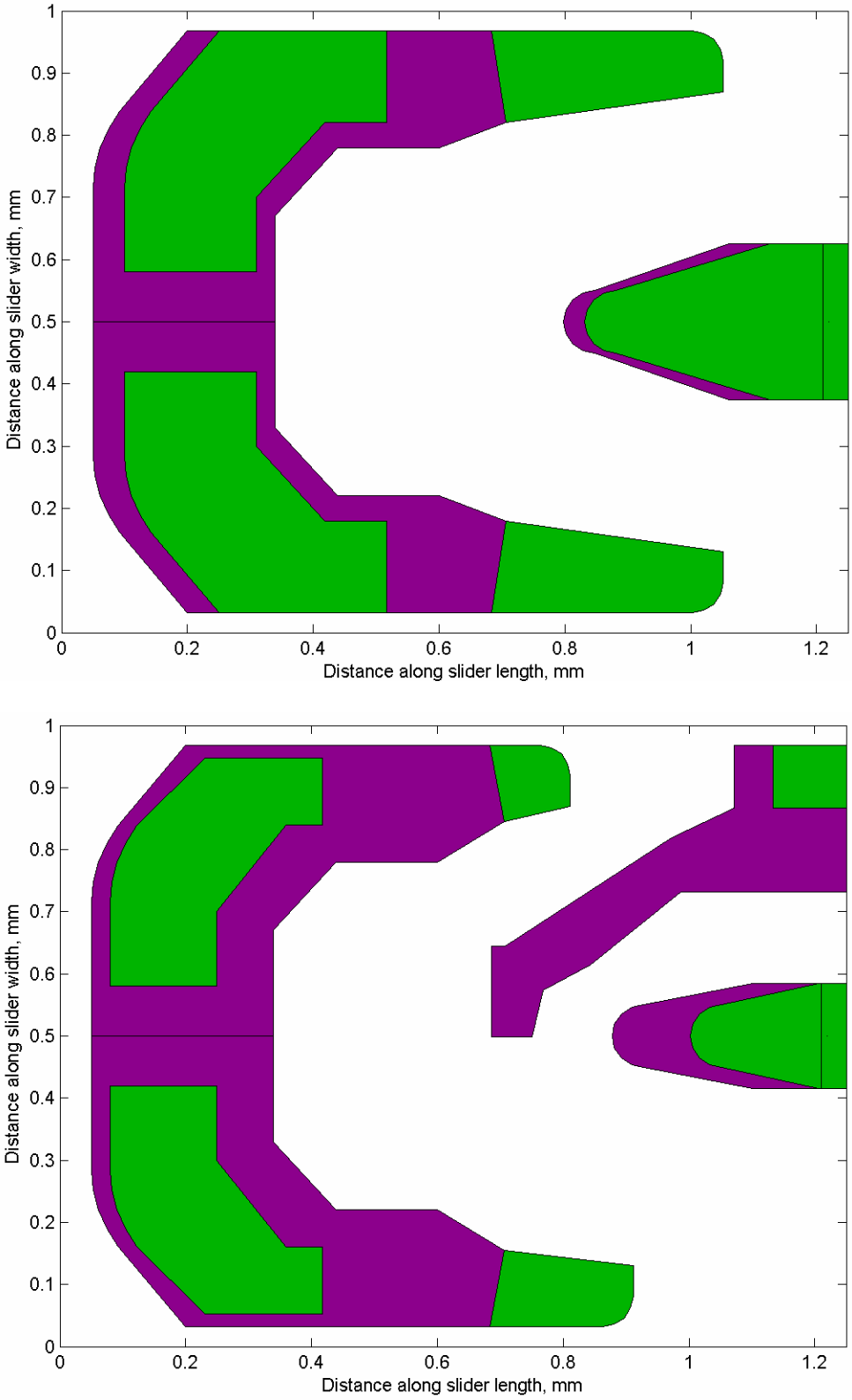

Figure 6.13 Channel effects on particle flow in head disk interface

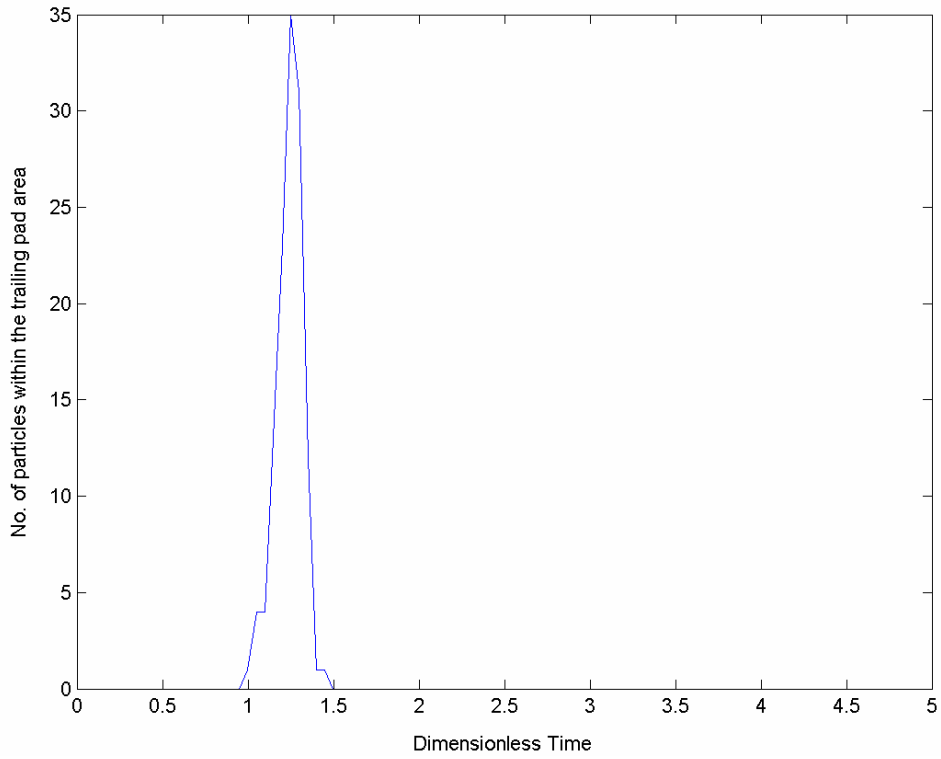

Figure 6.14 Number of particles passing through the MR element area: Original Design

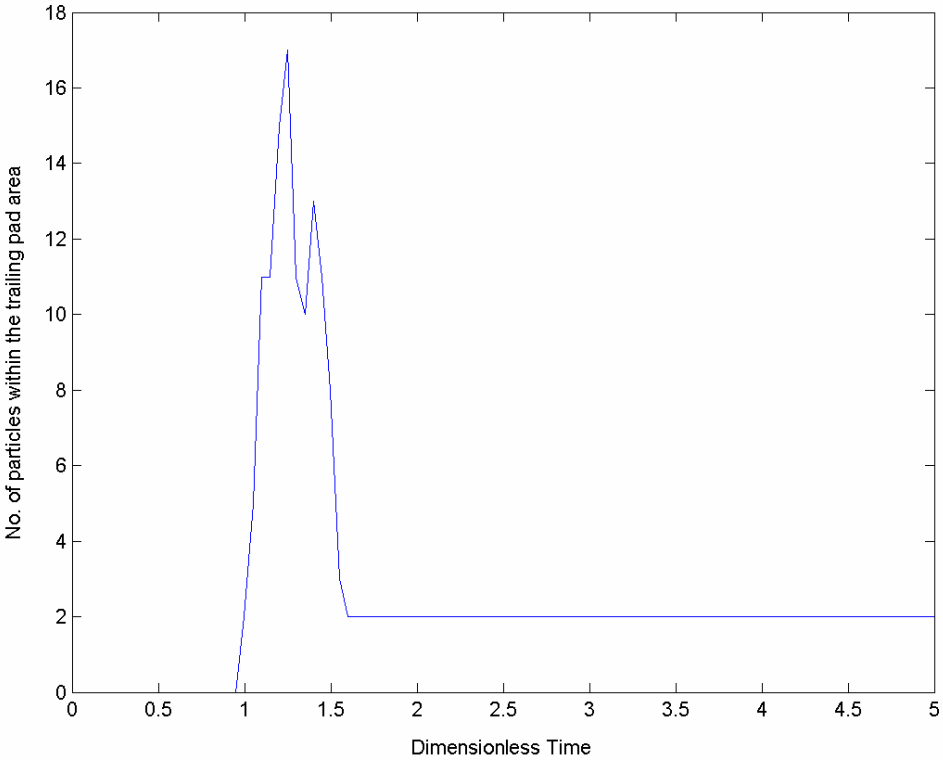

Figure 6.15 Number of particles passing through the MR element area: Channel Design

Table 6.1. Summary of wall profile effects on particle contamination patterns on sliders

	Original Slider	Modified I	Modified II
FH (nm)	26	26	25.5
Pitch	56	62	64
Roll	-0.57	-4	-4
No. of particles on the slider (out of 864)	237	161	76

Table 6.2. Summary of crown effects on particle contamination patterns on sliders

Crown	5nm	20nm
FH (nm)	5	7
Pitch	150	166
Roll	0.82	1.6
No. of particles on the slider (out of 864)	169	157

CHAPTER 7

SUMMARY AND CONCLUSIONS

For fixed as well as removable hard disk drives several technical challenges remain to achieve 1 Tbit/in^2 areal density. One of the most important challenges is to obtain a reliable head-disk interface. Contamination particles in the head-disk interface become more problematic as the slider flying height decreases. They cause slider flying height modulation and MR readback signal change when a particle passes through the trailing edge where the MR element is located. More severely, they may damage the disk media and destroy data stored on the disk. To achieve 1 Tbit/ in^2 areal density, the mechanical clearance between the head and disk must be as low as 3nm. An understanding of the behavior of particles in such spacing becomes essential in designing a reliable head-disk interface. The research reported in this dissertation aims to shed light on the causes and solution of the problem of particle contamination of the HDI.

Here, the work focuses on understanding the air flow for ultra low flying height sliders as well as particle flow in the head-disk interface together with its effects. Contamination control air bearing designs are also proposed based on the analysis of particle flow and contamination for low flying height sliders.

In Chapter 2, a new air bearing model including transverse flow is proposed. The geometry is usually very complex for modern air bearing sliders, which have several etch steps that are formed during the manufacturing process. The two-dimensional flow

modeling that forms the basis of the compressive Reynolds equation is not sufficient for some applications such as particle flow in the head disk interface. By including some transverse flow component in the air bearing analysis we can better predict the flying and contamination behavior of the particles in the head-disk interface. The major improvement is the inclusion of the geometry and pressure gradients in the air bearing analysis, which changes significantly the forces acting on the particles.

To appropriately simulate the wall angle at the etch steps of the air bearing slider we propose a hybrid grid algorithm in Chapter 3. The new grid generation algorithm with refinement features gives more precise results than the old pressure gradient based grid. Also, the new grid requires less grid size and thus less computational time is required for convergence.

From the multi-particle flow analyses in the air bearing in Chapter 4 we observe that the analysis with transverse flow effects predicts results that are quite different from those predicted by the purely 2-D air bearing theory. We observe that with the transverse effects the particles are more likely to contaminate the transition regions on the rail surfaces between the leading pad and recessed regions, a result not predicted by the 2-D flow analysis. And also, the particle contamination profile predicted using the 3-D model with air transverse flow is consistent with experimental results.

In Chapter 5 a three-body contact model is employed to study the effects of a particle entrapped between a slider and disk. A criterion for determining a particle's movement pattern is proposed. A detailed study of particles in a head-disk interface shows that large particles are likely to slide between the slider and disk, and particles going through the trailing pad of an air bearing slider produce severe contact force on the

slider generating significant heat flux. The frictional heating study shows that the temperature around the MR element will increase about 5^0C for a single 200nm particle passing through the trailing pad. The effects of particle size, disk material and friction coefficient are also studied. It is found that the disk and slider materials and the friction coefficient have a large effect on the contact force exerted on the slider by a particle as well as the temperature rise at the MR transducer. A glass disk produces a more severe contact force and thermal spike on the slider by particles in the interface while an aluminum disk will be indented more by the particles than the glass disks.

Because of the effect of the air's transverse flow on a particle's flying behavior in the air bearing one may modify a particle's flying path by changing the wall profiles and crown of a slider. The study in Chapter 6 found that the wall profile can have a large effect on the particle contamination pattern on a slider. The curved wall profile is advantageous for reducing particle contamination on the slider's ABS. One such wall profile is shown to reduce the air's transverse flow velocities at the transition regions of a slider. For this slider with curved wall profiles a 70% reduction of the small particle contamination is predicted by the numerical experiments. Also, increasing the crown of a slider's air bearing not only increases the slider's pitch angle, but also reduces by 7% the particle contamination on the particular slider studied. Finally, the study incorporating a channel design in the ABS indicates that one may also improve the particle flow behavior significantly by proper design practices.

REFERENCES

[1] Burgdorfer, A., 1959, "The Influence of the Molecular Mean Free Path on the Performance of Hydrodynamics Gas Lubricated Bearing", *ASME Journal of Basic Engineering*, **81**, No. 1, pp. 94-100.

[2] Carslaw, H. S., Jaeger, J. C., 1986, *Conduction of Heat in Solid*, Clarendon Press, Oxford.

[3] Cha, E. T., 1993, "Numerical Analysis of Head-Disk Assembly Dynamics for Shaped Rail Sliders with Sub-ambient Pressure Regions", Doctoral Dissertation,Department of Mechanical Engineering, University of California, Berkeley.

[4] Cha, E. T., Bogy, D. B., 1995, "A Numerical Scheme for Static and Dynamic Simulation of Sub-ambient Pressure Shaped Rail Sliders", *ASME Journal of Tribology,* **117**, p.36-46.

[5] Chen, L, Bogy, D. B. and Strom B., 2000, "Thermal Dependence of MR Signal on Slider Flying State", *IEEE Transactions on Magnetics,* **36**, pp.2486-2489.

[6] Chen, M., McLaughlin, J. B., 1995, "A New Correlation for The Aerosol Deposition Rate in Vertical Ducts", *Journal of Colloid and Interface Science*, **169**, pp.437-455.

[7] Chen, X., 1996, "The Drag Force Acting on a Spherical Non-evaporating or Evaporating Particle Immersed into a Rarefied Plasma Flow", *Journal of Physics D: Applied Physics*, **29**, pp. 995-1005.

[8] Clift, R., Grace, J. R., Weber, M. E., 1978, "Bubbles, Drops, and Particles", *Academic Press*.

[9] Cox, R. G., Hsu, S. K., 1977, "The Lateral Migration of Solid Particles in A Laminar Flow near A Plane", *Int. J. Multiphase Flow*, **3**, pp. 201-222.

[10] Fukui, S., Kaneko, R., 1988, "Analysis of Ultra-thin Gas Film Lubrication Based on Linearized Boltzmann Equation: First report-Derivation of A Generalized Lubrication Equation Including Thermal Creep Flow", *ASME Journal of Tribology*, **110**, p.253-261.

[11] Fukui, S., Kaneko, R., 1990, "A Database for Interpolation of Poiseuille Flow Rates for High Knudsen Number Lubrication Problems", *ASME Journal of Tribology*, **112**, p.78-83.

[12] Gans, R., 1985, "Lubrication Theory at Arbitrary Knudsen Number", *J. of Tribology*, **107**, p.431-433.

[13] Garcia-Suarez, C., Bogy, D. B., Talke, F. E., 1984, "Use of an Upwind Finite Element Scheme for Air Bearing Calculation", *ASLE SP-16*, pp. 90-96.

[14] Golaman, A. J., Cox, R. G., Brenner, H., 1967, "Slow Viscous Motion of A Sphere Parallel to A Plane Wall -I: Motion through a Quiescent Fluid", *Chemical Engineering Science*, **22**, pp.637-651.

[15] Gross, W. A., et al, 1980, "Fluid Film Lubrication", *John Wiley & Sons, Inc*.

[16] Hempstead, R. D., 1974, "Thermally Induced Pulses in Magnetoresistive Heads", *IBM J. Res. & Dev.*, **18**, P547-550.

[17] Hiller, B., Brown, B., 1993, "Interaction of Individual Aluminum Particles with the Head-Disk Interface at Various Velocities", *Adv. Info. Storage Syst*., **5**, pp.351-361.

[18] Hiller, B., Singh, G. P., 1991, "Interaction of Contamination Particles with the Particulate Slider/Disk Interface", *Adv. Info. Storage Syst*., **2**, pp.173-180.

[19] Hsia, Y. T., Domoto, G. A., 1983, "An Experimental Investigation of Molecular Rarefaction Effects in Gas Lubricated Bearings at Ultra-Low Clearance", *ASME Journal of Tribology*, **105**, pp. 120-130.

[20] Hu, Y., Bogy, D. B., 1995, "The CML Air Bearing Dynamic Simulator", *CML Tech. Report*, No 95-011, UC Berkeley.

[21] Hunt, A. P., 1971, "A Magnetoresistive Readout Transducer", *IEEE Transactions on Magnetics*, Vol. Mag-7, No. 1, pp.150-154.

[22] Jander, A., Indeck, R. S., Brug, J. A., Nickel, J. H., (1996) "A Model for Predicting Heating of Megnetoresistive Heads", *IEEE Tran. On Mag.*, Vol.32, N.5, p3392-3394.

[23] Karis, T. E., Marchon, B., et. al., 2001, "Lubricant Spin-off on Rotating Disks", *Tribology letters*, **11**, pp.151.

[24] Kennard, A. H., 1938, "Kinetics Theory of Gases", *McGraw-Hill Book Company, Inc*., New York and London.

[25] Kennedy, F. E., 2001, "Frictional Heating and Contact Temperatures", in *Modern Tribology Handbook*, CRC Press.

[26] Khonsari, M., Pascovici, M. and Kuchinschi, B., 1999, "On the Scuffing Failure of Hydrodynamic Bearings in the Presence of an Abrasive Contaminant", *ASME Journal of Tribology*, **121**, pp. 90-96.

[27] Koka, R., 1989a, "Effects of Fine Particles on the Slider/Disk Interface in Rigid Disk Drives", *Tribol. Mech. Magn. Storage Systems*, STLE SP-26, pp. 40-46.

[28] Koka, R., Kumaran, A. R., 1991, "Visualization and Analysis of Particulate Buildup on the Leading Edge Tapers of Sliders", *Adv. Info. Storage Syst.*, **2**, pp.161-171.

[29] Lee, J. W., Yi, M.-Y. and Lee, S. M., 2003, "Inertial focusing of particles with an aerodynamics lens in the atmospheric pressure range", Journal of Aerosol Science, **34**, pp. 211-224.

[30] Liu, V. C., Pang, S. C., Jew, H., 1965, "Sphere Grad in Flows of Almost-Free Molecules", *The Physics of Fluids*, **8**, pp. 788-796.

[31] Lu, S., Bogy, D. B., 1994, "A Multi-Grid Control Volume Method for the Simulation of Arbitrarily Shaped Slider Air Bearings with Multiple Recess Levels", *CML report*, No. 94-016, UC Berkeley.

[32] Lu, S., Bogy, D. B., 1995, "CML Air Bearing Design Program User's Manual", *CML report*, No. 95-003, UC Berkeley.

[33] Lu, S., 1997, *Numerical Simulation of Slider Air Bearing*, Doctoral Dissertation, Department of Mechanical Engineering, University of California, Berkeley.

[34] Ma, X., Chen, J, et. al, 2001, "Contribution of lubricant thickness to head-media spacing", IEEE Transactions on Magnetics, **37**, pp.1824-1826.

[35] Ma, X., Kuo, D., et. al., 2002, “Effect of lubricant on flyability and read-write performance in the ultra-low flying regime”, *ASME Journal of Tribology*, **124**, pp. 259.

[36] Mate, C. M., 1992, “Application of disjoining and capillary-pressure to liquid lubricant films in magnetic recording”, *J. Appl. Phys.*, **72,** pp. 3084.

[37] Maxey, M. R., 1993, “The Equation of Motion for A Small Rigid Sphere in A Nonuniform or Unsteady Flow”, *Gas-Solid Flows*, **Fed-Vol. 166**, pp.57-62.

[38] McLaughlin, J. B., 1993, "The Lift on a Small Sphere in Wall-bounded Linear Shear Flows", *Journal of Fluid Mechanics*, **246**, pp. 249-265.

[39] Miu, D. B., Bogy, D. B., 1986, “Dynamics of Gas Lubricated Slider Bearings in Magnetic Recording Disk Files: Part II̦ Numerical Simulation”, *ASME Journal of Tribology*, **108**, pp. 584-588.

[40] Millikan, R. A., 1923, “The General Law of Fall of A Small Spherical Body through A Gas, and Its Bearing Upon the Nature of Molecular Reflection from Surfaces”, *Physical Reviews*, **22**, pp.1-23.

[41] Mitsuya, Y., 1993, "Modified Reynolds Equation for Ultra-Thin Film Gas Lubrication Using 1.5-Order Slip-Flow Model and Considering Surface Accommodation Coefficient", *ASME Journal of Tribology*, **115**, pp. 289- 294.

[42] O'Hara, M., Hu, Y., and Bogy, D. B., 1996, “Effects of Slider Sensitivity Optimization”, *IEEE Transactions on Magnetics*, **32**, pp.3744-3746.

[43] O'Hara, M., and Bogy, D. B., 1995, “CML Air Bearing Optimization Program”, *CML Technical Reports*, No.95-015.

[44] Patankar, S. V., 1980, *Numerical Heat Transfer and Fluid Flow*, McGray-Hill, New York.

[45] Rubinow, S. I., Keller, J. B., 1961, "The Transverse Force on A Spinning Sphere Moving in A Viscous Fluid", *J. Fluid Mech*., **11**, pp.447-459.

[46] Ruiz, O. J., Bogy, D. B., 1990, "A Numerical Simulation of the Head-Disk Assembly in Magnetic Head Disk: 1. Component Models", *ASME Journal of Tribology*, **112**, pp. 593-602.

[47] Saffman, P. G., 1965, "The Lift on A Small Sphere in A Slow Shear Flow", *J. Fluid Mech*., **22**, pp. 385-400.

[48] Shah, R. K. and London, A. L., 1978, *Laminar flow forced convection in ducts*, Academic Press, New York.

[49] Shen, X.-J. and Bogy, D. B., 2002**, "**Particle Flow and Contamination in Slider Air Bearings for Hard Disk Drives", *ASME Journal of Tribology*, **125**, pp. 358-363.

[50] Shen, X.-J., Suk, M. and David B. Bogy, 2003**, "**Study of Transverse Flow Effects on Particle Flows and Contamination of Air Bearing Sliders", *ASME Magnetic Storage Symposium*, **125**, pp. 1-6.

[51] Shimomizuki, N., Adachi, T., et al, 1993, "Numerical Analysis of Particle Dynamics in A Bend of A Rectangular Duct by the Direct Simulation Monte Carlo Method", *Gas-Solid Flows*, *Fed-Vol. 166*, p.145-152.

[52] Shyy, W., Sun, C. S., 1993, "Development of A pressure-correction/Staggeredgrid Based Multi-grid Solver for Incompressible Recirculating Flows", *Computer and Fluids*, **22**, pp.51-76.

[53] Singer, P., Feb. 1997, "Read/Write Heads: The MR Revolution", *Semiconductor International*, pp.71.

[54] Sommerfeld, M., Qiu, H., 1993, "Characterization of Particle-Laden, Confined Swirling Flows by Phase-Doppler Anemomentry and Numerical Calculation", *Int. J. Multiphase Flow*, **19**, pp. 1093-1127.

[55] Talke, F. E., Tseng, R. C., 1973, "An Experimental Investigation of the Effect of Medium Thickness and Transducer Spacing on the Read-Back Signal in Magnetic Recording Systems", *IEEE Transactions on Magnetics*, **MAG-9**, pp.133-139.

[56] Thornton, Brian., 2003, *Head-Disk Interface Dynamics of Ultra-Low Flying Air Bearing Sliders for Hard-Disk Drive Applications*, Doctoral Dissertation, Department of Mechanical Engineering, University of California, Berkeley.

[57] White, J. M., Nigam, A., 1980, "A Factored Implicit Scheme for the Numerical Solution of the Reynolds Equation at Very Low Spacing", *ASME Journal of Tribology*, **102**, pp. 80-85.

[58] Wood, R, 2000, "The Feasibility of Magnetic Recording at 1 Terabit per Square Inch", *IEEE Transactions on Magnetics*, **36**, pp. 36-42.

[59] Wu, L., 2001, *Physical Modeling and Numerical Simulations of the Slider Air Bearing Problem of Hard Disk Drives*, Doctoral Dissertation, Department of Mechanical Engineering, University of California, Berkeley.

[60] Zhang, S. and Bogy, D. B., 1997a, "Effects of Lift on the Particle Motion in Recessed Regions of a Slider", *Physics of Fluids*, **9**, pp.1265-1272.

[61] Zhang, S. and Bogy, D. B., 1997b, "Slider Designs for Controlling Contamination", presented in the *Int. 1996 ASME/STLE Trib. Conf.*, and published in *ASME Journal of Tribology*, **119**, pp.537-540.

[62] Zhang, S. and Bogy, D. B., 1997c, "Motion of Particles in A Slider/Disk Interface Including Lift Force and Wall Effects", presented in *INTERMAG97*, and published in the *IEEE Transactions on Magnetics*, **33**, pp.3166-3169.

Table of Contents

APPDENDIX A

CML PARTICLE FLOW AND SLIDER CONTAMINATION PROGRAM USER'S MANUAL

A.1. Introduction

This manual describes the first version of the CML particle flow and slider contamination program with its Matlab user interface, as well as its input files, preprocessing and post processing.

The CML particle flow and slider contamination program requires Matlab installed on the computer, a commercial software from Mathworks Inc. The CML particle flow and slider contamination program interface integrates the preprocessing and post processing with two solvers: the CML air bearing solver and the CML particle flow solver. Both solvers are written in Fortran 77 and tested under the PC/windows environment. The unix/linux operating systems are currently unsupported.

System recommendations for running the CML particle flow and slider contamination program:

Hardware:

Intel based Pentium 4 systems above 2GHz

AMD based systems above AMD 2000+

512Mb memory with 1Gb virtual memory

Software:

Windows operating systems, Windows NT, 2000, XP.

Matlab ver. 5.0 and above.

CMLAir Design Program 6.5

A.2. Installation

The installation package for Windows is a zipped file named **cmlparticleflow.zip**. Unpack the file into a working directory with an unzip utility such as **winzip** software. As an example, we will assume the directory is D**:\cmltemp**. When you are ready to run a simulation, copy your input files (rail.dat, run.dat, and Particles.dat) into the working directory D:**cmltemp**.

The installation does not require any association with window's core and registry system. Therefore, it is very stable and robust.

To run the software, start Matlab from the windows start menu or desktop. Then change the directory in Matlab to the current working directiory, D:\cmltemp. Enter the command, ParticleGUI in the Matlab command window. The particle flow and slider contamination program interface will show up.

A.3. Interface guide

The main interface is shown in Fig. A.1. The menu bar includes File, Input Files, Slider, Preprocessing, Particle Solver, Particle Flow visualization, Results and Help.

The File submenu includes one option only. You can save the current work and exit from File -> Exit.

To run the particle flow simulation, three input files are needed. They are included in the Input Files submenu as shown in Fig. A.2. They are rail.dat, run.dat and

Particles.dat. You can open and edit them in the notepad program provided by Windows or other commercial text editor software.

In the Slider submenu, you can verify your slider design which is imported from CMLAir Design Program. Figure A.3 shows the slider submenu. You can view the 2-D rails first. After you run the CML air bearing solver, you may view its 3-D profile, pressure profile, and the spacing map between the head and disk.

Figure A.4 shows the Preprocessing submenu. You can run the CML air bearing solver by clicking on “Solve Reynolds equation”. The preprocessing solver gets the necessary information for particle flow and slider contamination simulation, such as pressure and the spacing profiles where the particles will fly.

After running the CML air bearing solver, you can now run the particle solver by clicking on the “Solve particle flow” button as shown in Fig. A.5. To run the particle flow, you need to make sure that Particles.dat is in the current directory. Also, to get a realistic simulation, you need to specify the particle source similar to what you expect in your experiments. The simulation will take several hours even for a modern PC, also it may take a lot of computer resources such as memory and storage spaces.

After simulating the particle flow in the head disk interface, you need to observe how the particles fly in your specific head disk interface design. The submenu “Particle Flow visualization” in Fig. A.6 includes three methods of visualization. You can use the 2-D particle flow animation to see how the particles fly in HDI from a top view. You can also run the 3-D flow movie. However, this animation requires much more time and

computer resources. The particle buildup history on the air bearing surface can also be visualized using the current software.

The Results submenu shown in Fig. A.7 lets you see the result summary of the air bearing slider, particle contamination profile, and the contact force and moment history applied to the slider by these particles.

Figure A.8 shows the Help menu. Before you run the simulation, it is recommended that you read the README file and this manual.

A.4. Input data files

There are three input data files in this version: **rail.dat, run.dat** and **Particles.dat.** The first file describes the slider geometry, while the second one prescribes the input parameters for the CML Airbearing Design Program. The third file specifies the particle properties and the environmental conditions for the particle flow simulation.

A.4.1 rail.dat

Sample rail.dat:

```
CML Version 4.020  RAIL.DAT
REPORT BUGS TO INFO@CML.ME.BERKELEY.EDU
1.2500E-003     1.0000E-003     3.0000E-004
 11             3
 13             1
1.1009E-003     4.1500E-004     2
1.2100E-003     4.1500E-004     0
1.2100E-003     5.8500E-004     2
1.1009E-003     5.8500E-004     2
9.2772E-004     5.5000E-004     2
```

9.0872E-004 5.4600E-004 2
8.9272E-004 5.3500E-004 2
8.8172E-004 5.1900E-004 2
8.7772E-004 5.0000E-004 2
8.8172E-004 4.8100E-004 2
8.9272E-004 4.6500E-004 2
9.0872E-004 4.5400E-004 2
9.2772E-004 4.5000E-004 2
3.0000E-007
13 1
1.0516E-003 5.5000E-004 3
1.0326E-003 5.4600E-004 3
1.0166E-003 5.3500E-004 3
1.0056E-003 5.1900E-004 3
1.0016E-003 5.0000E-004 3
1.0056E-003 4.8100E-004 3
1.0166E-003 4.6500E-004 3
1.0326E-003 4.5400E-004 3
1.0516E-003 4.5000E-004 3
1.2059E-003 4.1500E-004 1
1.2500E-003 4.1500E-004 0
1.2500E-003 5.8500E-004 1
1.2059E-003 5.8500E-004 3
0.0000E+000
13 1
4.3915E-004 7.8000E-004 2
3.3915E-004 6.7000E-004 2
3.3915E-004 5.0000E-004 0
5.0000E-005 5.0000E-004 2
5.0000E-005 7.1500E-004 2
5.3000E-005 7.4800E-004 2
6.1000E-005 7.8000E-004 2
7.4000E-005 8.1000E-004 2
9.2000E-005 8.3800E-004 2
2.0000E-004 9.6800E-004 2
6.8339E-004 9.6800E-004 0
7.0608E-004 8.4500E-004 2
6.0000E-004 7.8000E-004 2
3.0000E-007
8 1
6.8339E-004 9.6800E-004 1
7.6222E-004 9.6800E-004 1
7.8122E-004 9.6400E-004 1
7.9722E-004 9.5400E-004 1
8.0722E-004 9.3800E-004 1
8.1142E-004 9.1900E-004 1

8.1142E-004 8.7000E-004 1
7.0608E-004 8.4500E-004 3
0.0000E+000
4 1
1.2200E-003 5.0025E-004 0
1.2200E-003 4.9975E-004 0
1.2199E-003 4.9975E-004 0
1.2199E-003 5.0025E-004 0
0.0000E+000
12 1
6.8600E-004 4.9800E-004 0
7.5100E-004 4.9800E-004 0
7.6800E-004 5.7300E-004 0
8.4400E-004 6.1400E-004 0
9.8700E-004 7.3200E-004 0
1.2500E-003 7.3200E-004 0
1.2500E-003 9.6800E-004 0
1.0720E-003 9.6800E-004 0
1.0720E-003 8.6700E-004 0
9.7300E-004 8.1900E-004 0
7.0700E-004 6.4500E-004 0
6.8600E-004 6.4500E-004 0
1.0000E-005
13 1
4.3915E-004 2.2000E-004 2
3.3915E-004 3.3000E-004 2
3.3915E-004 5.0000E-004 0
5.0000E-005 5.0000E-004 2
5.0000E-005 2.8500E-004 2
5.3000E-005 2.5200E-004 2
6.1000E-005 2.2000E-004 2
7.4000E-005 1.9000E-004 2
9.2000E-005 1.6200E-004 2
2.0000E-004 3.2000E-005 2
6.8339E-004 3.2000E-005 0
7.0608E-004 1.5500E-004 2
6.0000E-004 2.2000E-004 2
3.0000E-007
8 1
6.8339E-004 3.2000E-005 1
8.6222E-004 3.2000E-005 1
8.8122E-004 3.6000E-005 1
8.9722E-004 4.6000E-005 1
9.0722E-004 6.2000E-005 1
9.1142E-004 8.1000E-005 1
9.1142E-004 1.3000E-004 1

7.0608E-004 1.5500E-004 3
0.0000E+000
4 1
1.1340E-003 9.6800E-004 0
1.1340E-003 8.6700E-004 0
1.2500E-003 8.6700E-004 0
1.2500E-003 9.6800E-004 0
0.0000E+000
12 1
8.0000E-005 4.2000E-004 3
8.0000E-005 2.8500E-004 3
8.3000E-005 2.5200E-004 3
9.1000E-005 2.2000E-004 3
1.0400E-004 1.9000E-004 3
1.2200E-004 1.6200E-004 3
2.3000E-004 5.2000E-005 1
4.1694E-004 5.2000E-005 3
4.1694E-004 1.6000E-004 3
3.5915E-004 1.6000E-004 3
2.4915E-004 3.0000E-004 3
2.4915E-004 4.2000E-004 3
0.0000E+000
12 1
8.0000E-005 5.8000E-004 3
8.0000E-005 7.1500E-004 3
8.3000E-005 7.4800E-004 3
9.1000E-005 7.8000E-004 3
1.0400E-004 8.1000E-004 3
1.2200E-004 8.3800E-004 3
2.3000E-004 9.4800E-004 1
4.1694E-004 9.4800E-004 3
4.1694E-004 8.4000E-004 3
3.5915E-004 8.4000E-004 3
2.4915E-004 7.0000E-004 3
2.4915E-004 5.8000E-004 3
0.0000E+000
10 10 10
0.0000E+000 1.3822E-006 2.7644E-006 4.1467E-006 5.5289E-006 6.9111E-006
8.2933E-006 9.6756E-006 1.1058E-005 1.2440E-005
0.0000E+000 5.2469E-007 9.8765E-007 1.3889E-006 1.7284E-006 2.0062E-006
2.2222E-006 2.3765E-006 2.4691E-006 2.5000E-006
0.0000E+000 1.2222E-006 2.4444E-006 3.6667E-006 4.8889E-006 6.1111E-006
7.3333E-006 8.5556E-006 9.7778E-006 1.1000E-005
3.0000E-007 7.6173E-007 1.1691E-006 1.5222E-006 1.8210E-006 2.0654E-006
2.2556E-006 2.3914E-006 2.4728E-006 2.5000E-006

0.0000E+000 1.6933E-007 3.3867E-007 5.0800E-007 6.7733E-007 8.4667E-007
1.0160E-006 1.1853E-006 1.3547E-006 1.5240E-006
0.0000E+000 6.2963E-008 1.1852E-007 1.6667E-007 2.0741E-007 2.4074E-007
2.6667E-007 2.8519E-007 2.9630E-007 3.0000E-007
0.0000E+000 0.0000E+000 2.5000E-006
2.5400E-008 2.5000E-009 0.0000E+000
1.2200E-003 1.2050E-003 2.4100E-004 2.4100E-004
5.0000E-004 5.0000E-004 9.7400E-004 2.6000E-005

The rail structure for this sample file is shown in Fig. A.9. The first two lines are the header. The third line contains the slider dimensions in meters: **length**, **width**, **thickness**. The fourth line indicates the **number of rails** and the **number of (different) wall profiles** used. Next, each rail is defined in succession. The starting line for each rail describes the **number of points** and **style**. A **step** has a **style** value of 1, while a **ramp** has a **style** value of 0. The lines that follow contain the **x and y coordinates** of a rail point and the **wall profile index** for the rail edge starting at that point. Note that the **x and y coordinates** are in meters instead of normalized, and the **wall profile indices** should be zero for a **ramp**. The final line in a rail description contains the **recess height(or three heights** for a **ramp)** in meters for the rail. The line that follows the rail definitions contains **the number of wall profile points** for all wall profiles. Next, each wall profile definition occupies two lines. The first line contains the normal distances to the nominal edge for the profile points. Note, the unit is in meters. A negative value indicates that the point is inside the nominal rail boundary, while a positive value is otherwise. The second line contains the recess depth in meters for each point. Note that the zero recess reference plane is the same as for all the rail recess depths, rather than the nominal recess for each rail. The next line contains the **taper length** in meters, the **taper angle** in radians, and the **base recess** in meters. The following line gives the crown,

camber and twist in meters. The final two lines are the **x and y coordinates** for the points of interest.

A.4.2 run.dat

Sample run.dat:

```
CML Version 6.020  RUN.DAT
REPORT BUGS TO INFO@CML.ME.BERKELEY.EDU
***************Solution Control***************
istiff isolv   ioldg   iadpt   isave
 1      1       0       1       1
***************Intial Attitude***************
hm(m)          pitch(rad)     roll(rad)
1.0000E-008    1.5000E-004    0.0000E+000
***************Runs***************
irad           irpm           ialt
 1             1              0
radii(m)
  2.3000E-002
skews(deg)
  9.1000E+000
RPMs
  7.2000E+003
altitudes(m)

***************Air Parameters***************
p0(pa)         al(m)          vis(nsm^-2)
1.0135E+005    6.3500E-008    1.8060E-005
***************Load Parameters***************
f0(kg)         xf0(m)         yf0(m)
1.5000E-003    0.0000E+000    0.0000E+000
xfs(µNM)       yfs(µNM)       emax
0.0000E+000    0.0000E+000    1.0000E-003
***************Grid Control***************
nx      ny
 593     593
nsx      nsy     isymm
 1       1       0
xnt(i), i = 2, nsx

nxt(i), i = 2, nsx
```

dxr(i), i = 1, nsx
1
ynt(i), i = 2, nsy

nyt(i), i = 2, nsy

dyr(i), i = 1, nsy
1
**********Adaptive Grid**********
difmax decay ipmax
100 60 1
100 60 0
**********Mesh refinement in x direction*******
1
0.380e-3 0.42e-3 0
**********mesh refinement in y direction*******
1
0.325e-3 0.375e-3 0
**********Reynolds Equation**********
ischeme imdoel akmax beta gamma accommodation
2 3 1.0000E-007 6.0000E+000 6.0000E+000 1.0000E+000
**********Partial Contact**********
icmodel stdasp(m) dnsasp(m^-2) ConstantA ConstantB
0 0.0000E+000 1.0000E+012 1.0000E-019 1.0000E-076
rdsasp(m) eyoung(pa) yldstr(pa)
0.0000E+000 1.0000E+010 1.0000E+012
frcoe pratio
0.3 0.3
**********Molecular Force Hamaker Constants(ahc,bhc)*****
0.0e-19 0.0e-76
**********Sensitivities**********
crowninc(m) camberinc(m) twistinc(m)
0.0000E+000 0.0000E+000 0.0000E+000
tlnginc(m) tanginc(rad) loadinc(kg)
0.0000E+000 0.0000E+000 0.0000E+000
ptrqinc(µNM) rtrquinc(µNM) recessinc(m)
0.0000E+000 0.0000E+000 0.0000E+000
iwscale
1
**********Comments**********
"This is a test case"

Here are some explanations:

Solution Control:

istiff: 1 = calculate stiffness, 0 = no stiffness calculation

isolv: 1 = solve for fly height, 0 = given attitude

ioldg: 1 = use existing grid data, 0 = create new grid

iadpt: 1 = use adaptive grid, 0 = no adaptive grid

isave: 1 = save pressure and mass flow, 0 = don't save

Initial Attitude:

hm(m): nominal trailing edge height

pitch(rad): pitch, note the change in units from the previous version

roll(rad): roll

Runs:

irad: number of disk radii where the solution is sought

irpm: number of RPMs

ialt: number of altitudes, 0 = use Air Parameters

radii(m): disk radii

skews(deg): skews corresponding to each disk radii

rpms: RPMs

altitudes(m): altitudes, lowest one is the base case.

Air Parameters:

p0(pa): ambient pressure

17

al(m): mean free path

vis(NS/M$_2$): viscosity

Load Parameters:

f0(kg): load

xf0(m): load point x offset, origin is at the geometric center now!

yf0(m): load point y offset

xfs(μNM): static pitch torque, note the change of unit

yfs(μNM): static roll torque

emax: convergence criterion of load error

Grid Control:

nx: total x grid number (16k+1)

ny: total y grid number (16k+1)

nsx: number of sections in length

nsy: number of sections in width

isymm: 1 = symmetry in width, 0 = specify entire width

xnt(i), i = 2, **nsx**: x control points in meters, no longer normalized!

nxt(i), i = 2, **nsx**: grid indices at x control points

dxr(i), i = 1, **nsx**: grid ratios for each x section

ynt(i), i = 2, **nsy**: y control points, use half width if **isymm** = 1

nyt(i), i = 2, **nsy**: grid indices at y control points

dyr(i), i = 1, **nsy**: grid ratios for each y section

Adaptive Grid:

difmax: ratio of max/min gradient allowed

decay: smaller value increases smoothness

ipmax:1 = use maximum gradient, 0 = average gradient

The adaptive grids in the x and y directions are controlled separately by two lines. The first line specifies difmax, decay and ipmax for the x direction. The second line defines these parameters for the y direction.

Mesh refinement in x and y directions:

The first line defines how many locations will be refined by the end user. The following lines specify the starting and ending locations for mesh refinement.

Reynolds Equation:

ischeme: convective term scheme.

0 = upwind

1 = hybrid

2 = power-law; default

imodel: slip model

1 = first order slip

2 = second order slip

3 = FK; default

akmax: convergence criterion for the Reynolds equation

Partial Contact:

icmodel: 0 = no contact model

1 = Greenwood-Williamson

2 = Elastic-Plastic

stdasp(m): standard deviation of asperity height

dnsasp(m^{-2}): asperity density

rdsasp(m): mean radius of curvature of asperity

eyoung(pa): Young's modulus

yldstr(pa): yield strength

frcoe: friction coefficient

pratio: Poisson's ratio

Intermolecular Force menu

Two constants, **ahc** and **bhc**, are defined for the adhesive force between the head and disk for ultra low flying height sliders. The first one is the effective Hamaker constant between the slider and disk. The second is the constant B used in the Lernard Jones potential. For detailed information of these two parameters, please refer to Lin Wu's Ph. D. dissertation at CML, "Physical Modeling and Numerical Simulations of the Slider Air Bearing Problem of Hard Disk Drives".

Sensitivities:

Zero increment means no sensitivity is calculated for the parameter.

crowninc(m): crown increment

camberinc(m): camber increment

twistinc(m): twist increment

tlnginc(m): taper length increment

tanginc(rad): taper angle increment

loadinc(kg): load increment

ptrqinc(μNM): pitch torque increment

rtrqinc(μNM): roll torque increment

recessinc(m): recess increment

iwscale: used with **recessinc**

0 = stretch the profile, the normal distances are unchanged,

only the depths are scaled.

1 = scale the wall profile with recess. For the part of the

profile that is outside the nominal rail boundary, the normal

distances will change proportionally with recess.

A.4.3 Particles.dat

Sample Particles.dat

```
lamda      rous      roup       amu          p0
.635e-7  1.4128d0   3.52d3   1.488e-5   1.0135e+5
NX|NY|NZ|
1   50  10
Xmean Std
200e-09 50e-9
  xp0      yp0       zp0
 0.02       0.04         6.0
 0.02       0.75        25.0
The velocity ratio to the disk |particle velocity option
7.5 2
 Time for simulation (T, DT)
5.0  1e-3
|The skew angle of the slider| Particle Module|Particle Distribution Option|
-17.55 2 2
|Gravity Effect| Saffman Lift|Magnus Lift | Pressure Gradient|Vortex
0.0 1.0 1.0 1.0 1.0
|Particle|Airbearing Module|Layer Streamline Module|
1 0 0
|Particle Nature:1: Soft; 2: Hard|
2
|Mechanical and Thermal Properties of particle(TiC)|
Young's Modulus|Poison's Raio|Hardness|Thermal conductivity|SPecific Heat|
4.39d11    0.187          2.47d9              30.9                710.6
Disk Material Properties(Aluminum)
|Density|Modulus|Poison's Ratio|Hardness|Thermal Conductivity|Specfific Heat(J/kg.C)|
2.7d3      6.9d10      0.3269      1.20d8            166.9          896
Slider Material Properties(TiC 40% Al2O3 60%)
|Density|Modulus|Poison's Ratio|Hardness|Thermal Conductivity|Specfific Heat|
4.31d3     4.390d11      0.2          2.42e9              27.0          898
Friction Coefficient( Betweeen particle and slider)
0.2
```

lamda: free mean path of the air.

rous: air density

roup: particle density

amu: air viscosity.

p0: air ambient pressure.

NX,NY,NZ: Number of particles in the X, Y, Z directions.

Xmean, Std (m): these two parameters define the particle mean size and standard deviation for a Gaussian distribution.

xp0, yp0, zp0: define the initial location of the particles. The first line defines the lowest value of x, y, z. The second line defines the upper limit of x, y, z.

The velocity ratio of particle to the disk is used for the initial particle velocity option. Particle velocity option: 1: its ratio to the disk velocity is specified. 2: air borne particles. 2 is the default option for most cases.

T, DT: simulation time and time step. These two are normalized. The user can change the time step to balance the calculation time and accuracy based on experience.

In the remaining part of the input file, each item is clearly defined. The user can enter the corresponding value for specific case.

A.5. Output data files

The output files include ParticleD.dat, Pcontaminates.dat, Summary.dat, and Contacts.dat. These output files are post processed in the particle flow and slider contamination software interface.

A.6. Post processing

The post processing for particle flow and slider contamination includes visualization of the particle flow in the head disk interface, the final particle contamination profile on the slider, and the contact force and moment history acting on the air bearing slider. They are integrated into the software interface. Advanced users may modify the corresponding module to get other information. For visualization post processing, a movie file is generated for each animation. They are found in your working directory after you run the animation.

Figure A.1. Matlab interface

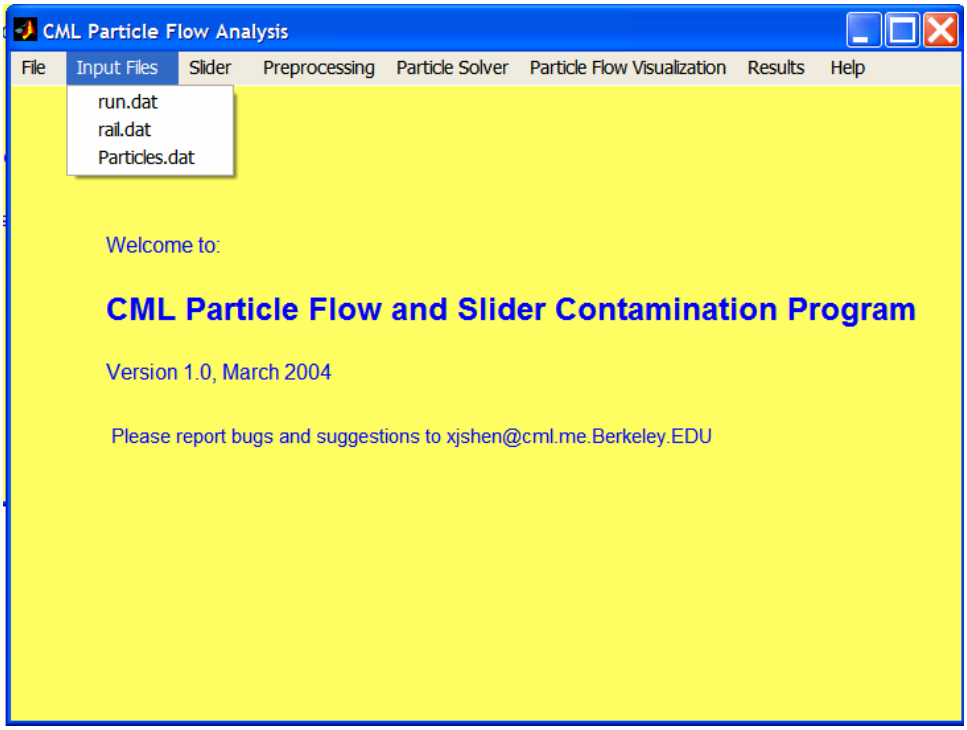

Figure A.2. Input files

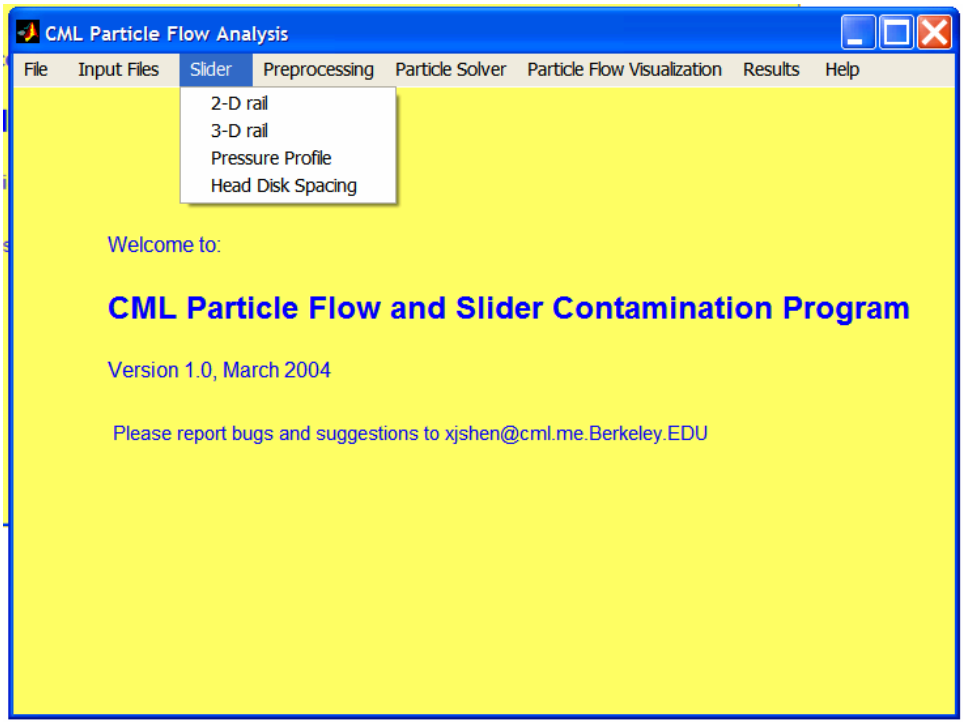

Figure A.3. Slider information

Figure A.4. CML air bearing solver

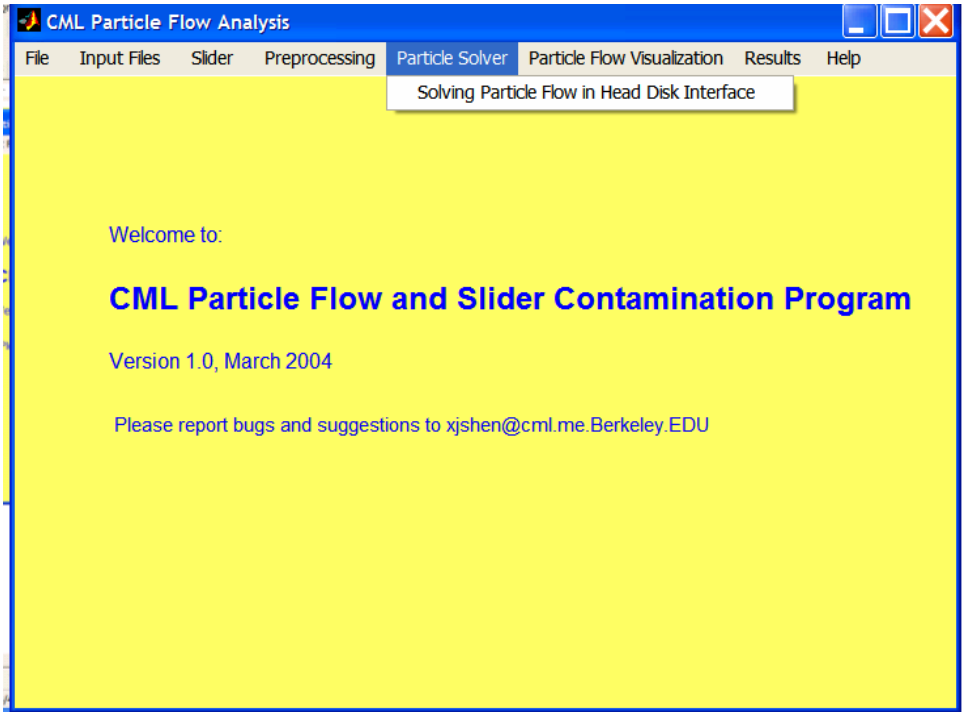

Figure A.5. CML particle flow and slider contamination solver

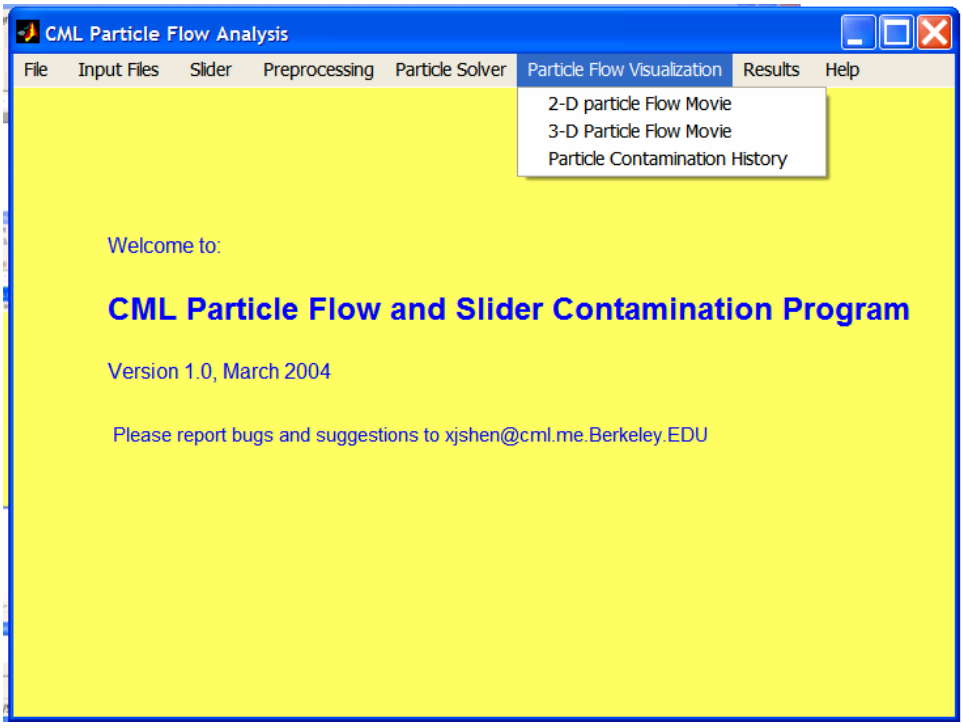

Figure A.6. Particle flow visualization modules

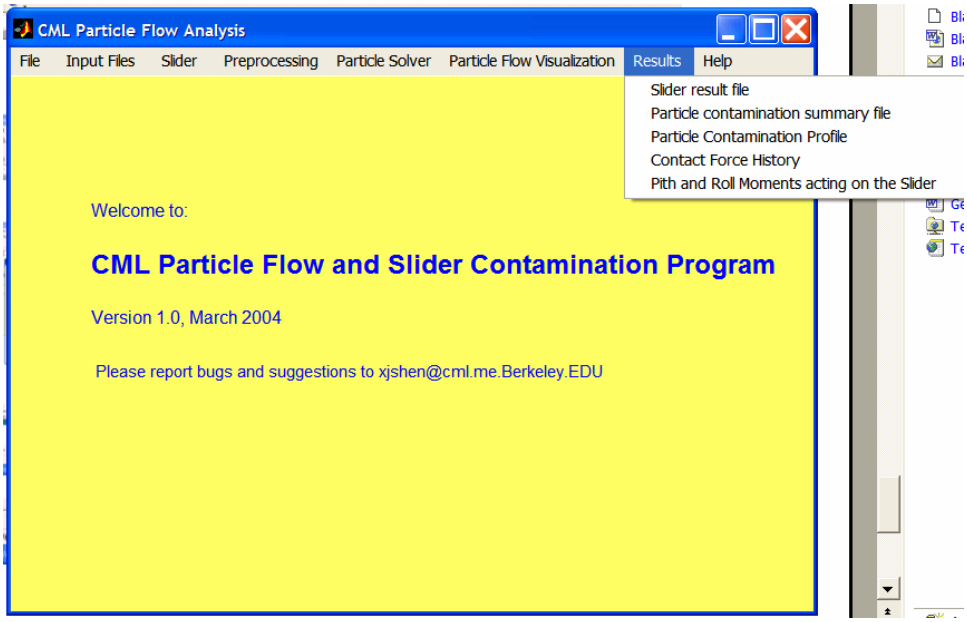

Figure A.7. Particle result files

Figure A.8. User's manual and README files

Table of Contents

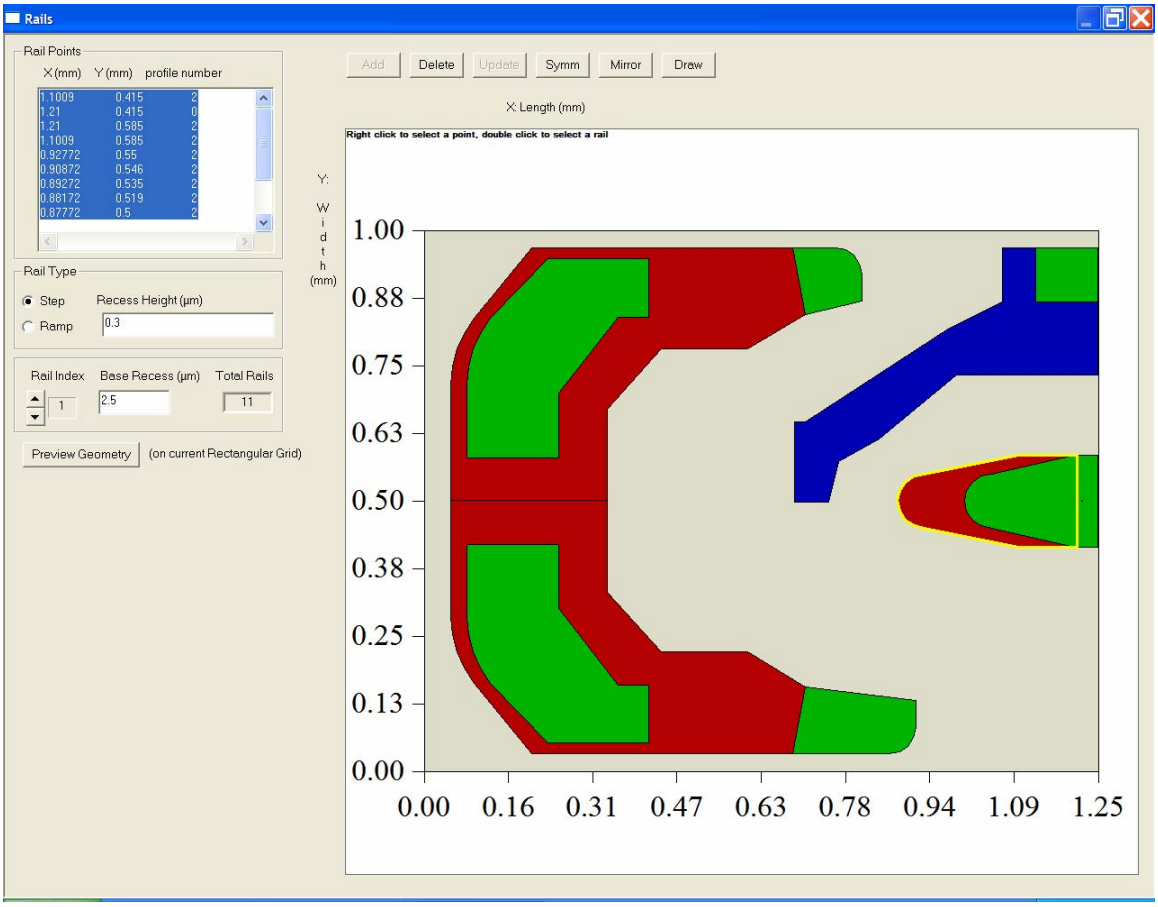

Figure A.9. A sample air bearing slider.